University of California
Santa Barbara

Multiscale network characterization of the strength and robustness of trabecular bone

A dissertation submitted in partial satisfaction
of the requirements for the degree

Doctor of Philosophy
in
Physics

by

Chantal Nguyen

Committee in charge:

Professor Jean Carlson, Chair
Professor Boris Shraiman
Professor Megan Valentine

September 2019

The Dissertation of Chantal Nguyen is approved.

Professor Boris Shraiman

Professor Megan Valentine

Professor Jean Carlson, Committee Chair

July 2019

Multiscale network characterization of the strength and robustness of trabecular bone

Chantal Nguyen

For my parents

Acknowledgements

First and foremost, I would like to thank my advisor, Jean Carlson, for her unwavering support and encouragement. Jean's vision and enthusiasm are unparalleled, and I have learned so much under her guidance. Most importantly, she has taught me how to communicate my work clearly and compellingly, and I am very grateful for her mentorship.

Ahmed Elbanna has been a second mentor over the course of this bone project. He has been incredibly kind and supportive and has provided many invaluable insights and ideas.

All of the work described here has really been a collaborative effort. I owe an tremendous amount to the hard work of Avik Mondal, who laid the groundwork (a massive understatement) for the network modeling and analysis; Darin Peetz, who developed the topology optimization framework that drove a large part of this thesis; Xiao Ma, who was enormously helpful in getting the mechanical simulations off the ground; and Kimberly Schlesinger, who has been a great person to work with on so many different things both within and outside of this dissertation.

Kristin James and Tim James have been fantastic people to work with and really kicked off this whole foray into bone. Ian Parker, Esther Cory, Giovanna Silberman, Koichi Masuda, and Robert Sah also provided much assistance and advice on the MR project.

A big thank you to Eric Jones, Josh Mueller, Imtiaz Ali, and all of the Carlson group members past and present that I had the pleasure of being colleagues with over my time here.

Thank you also to my committee members, Boris Shraiman and Megan Valentine, for generously offering their time and thoughtful feedback on this dissertation.

As they say, the real Ph.D. is the friends you make along the way. My fellow graduate students and housemates have made the past several years so much more fun than they would have been otherwise. My cohortmates — you guys are awesome! I miss our trailer shenanigans and am very glad to count you all as friends. Thank you to Sasha for being a great friend and for naming my inevitable future cat.

And finally, my parents have never ceased to be supportive and loving throughout my whole life and educational journey.

I acknowledge the support of the National Science Foundation under grants EAR-1345074, CMMI-1435920, and IIP-1548339; the David and Lucile Packard Foundation; the UCSB Graduate Division Doctoral Scholars and Graduate Opportunity Fellowships; the Worster Summer Research Fellowship; and the Institute of Collaborative Biotechnologies through Army Research Office Grant W911NF-09-D-0001. Use was made of computational facilities purchased with funds from the National Science Foundation (CNS-1725797) and administered by the Center for Scientific Computing (CSC). The CSC is supported by the California NanoSystems Institute and the Materials Research Science and Engineering Center (MRSEC; NSF DMR 1720256) at UC Santa Barbara.

Curriculum Vitæ

Chantal Nguyen

Education

2019	Ph.D. in Physics (Expected), University of California, Santa Barbara.
2016	M.A. in Physics, University of California, Santa Barbara.
2013	B.S. *magna cum laude* in Physics, California State University, Los Angeles.

Publications

1. **C. Nguyen**, D. Peetz, A. E. Elbanna, and J. M. Carlson. Characterization of fracture in topology-optimized bio-inspired networks. arXiv:1907.07860 (2019).
2. A. Mondal, **C. Nguyen**, X. Ma, A. E. Elbanna, and J. M. Carlson. Network-based models for characterization of trabecular bone. *Physical Review E* **99**(4), 042406 (2019).
3. **C. Nguyen**, K. J. Schlesinger, F. Han, I. Gur, and J. M. Carlson. Modeling individual and group evacuation decisions during wildfires. *Fire Technology* **55**(2), 517 (2018).
4. **C. Nguyen**, K. J. Schlesinger, T. W. James, K. M. James, R. L. Sah, K. Masuda, and J. M. Carlson. Novel magnetic resonance technique for characterizing mesoscale structure of trabecular bone. *Royal Society Open Science* **5**, 180563 (2018).
5. **C. Nguyen**, K. J. Schlesinger, and J. M. Carlson. Data-driven models for individual and group decision making. In the Proceedings of the IEEE/ACM International Conference on Advances in Social Networks Analysis and Mining (2017).
6. **C. Nguyen**, K. J. Schlesinger, and J. M. Carlson. Collective decision dynamics in group evacuation. In the Proceedings of the Summer Computer Simulation Conference (2017).
7. **C. Nguyen** and J. M. Carlson. Optimizing real-time vaccine allocation in a stochastic SIR model. *PLOS ONE* **11**(4), e0152950 (2016).

Abstract

Multiscale network characterization of the strength and robustness of trabecular bone

by

Chantal Nguyen

Trabecular bone is a flexible, lightweight bone tissue that exhibits hierarchical mechanisms of fracture resistance across scales. At the mesoscale, trabecular bone resembles a web of interconnected bone struts (trabeculae) that erode with age and diseases such as osteoporosis, resulting in increased fracture propensity. Recent *ex vivo* bone experiments have indicated that the traditional diagnostic marker of osteoporosis, bone mineral density (BMD), correlates poorly with bone strength when used as a sole predictor, but that it can explain much of the variation in bone strength when considered in conjunction with architectural features.

We introduce a novel approach to modeling trabecular bone that combines network analysis with simulations of mechanical loading and failure, enabling a unique characterization of how bone architecture contributes to robustness and resilience. Network science has been applied to a vast range of systems across biology and soft condensed matter physics, among many other fields, but has rarely been applied to the study of bone. Exploiting the disordered network resemblance of bone, we generate network models from tomographic images of real human vertebral bone. We simulate loading and deformation on finite element models in which edges are replaced by beams, resulting in a considerable reduction in computation time in comparison with fine-grained models used for *in silico* validation. The beam-element analysis facilitates direct comparison of mechanics and topology at multiple scales ranging from that of individual edges (beams) to the network as a whole.

To assess how variation in architecture impacts mechanical response, we also develop networked structures simulated via multi-objective topology optimization. We maximize a weighted combination of biologically motivated objectives: stiffness, surface area, and stability. By modulating the weights of the objectives, we analyze how tradeoffs in these quantities produce topologies of varying strength and robustness. Finally, we discuss implications of our work in the context of clinical application, facilitated by advances in data acquisition methods for assessing fine tissue structure, and we highlight future directions for integrating our results into a comprehensive characterization of bone that links its molecular constituents at the nanoscale to its architecture at large.

Contents

Chapter 1

Introduction

Bone is a hierarchical material that exhibits mechanisms of fracture resistance across multiple scales. At the macroscale, human bone consists of two types: the dense, shell-like *cortical* bone, and the web-like *trabecular* (or *cancellous*) bone. Here, we focus on trabecular bone, which is found mostly in the vertebrae, the pelvis, and at the ends of long bones (such as the femur), encased by a cortical shell. At the mesoscale, the architecture of trabecular bone resembles a highly porous network of struts and rods called *trabeculae* that are individually on the order of tens of microns in thickness. This structure results in a strong, lightweight material that can tolerate large deformations [1]. At the sub-microscale, individual trabeculae are made up of mineralized collagen fibrils, the "building blocks" of bone, which themselves comprise hydroxyapatite crystals embedded in a collagen matrix [2]. The micromechanics of these components have been shown to be predictive of overall bone stiffness [3, 4].

In this thesis, we primarily characterize trabecular bone at length scales in the range of 0.1 to 10 mm, which spans the thickness of an individual trabecula to more complex trabecular architecture. (In comparison, a vertebral body, for example, is about 50 mm across.) We develop a modeling framework that integrates various computational

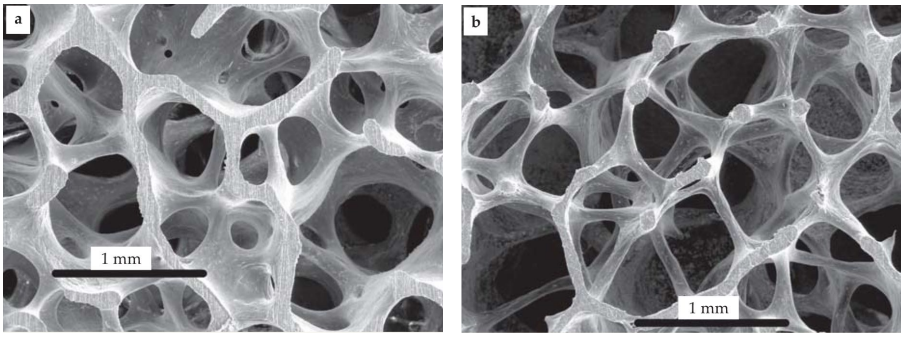

Figure 1.1: Comparison of trabecular structure in young (a) and old (b) bone. The young sample is taken from a 21-year-old male and the old sample from a 65-year-old female. Trabeculae are noticeably thinner in the older sample. From Ritchie, Buehler, and Hansma, *Phys. Today* **62**, 41, 2009 [6].

methods to relate structure and function in trabecular bone, and we further apply this framework to generate and analyze bone-inspired structures. The trabecular bone data studied in this work are high-resolution images obtained *ex vivo*, but we also validate a newly-developed magnetic resonance technique aimed at probing trabecular structure in live patients. A driving force behind the study of morphometry and mechanics in trabecular bone is its decreased fracture resistance due to osteoporosis, a metabolic bone disease that affects approximately 200 million worldwide [5], in addition to regular aging processes.

1.1 Trabecular bone

1.1.1 Osteoporosis

Trabeculae erode with age (Fig. 1.1), even to the point of perforation, widening and connecting the spaces on either side of a trabecula. The accumulation of microcracks and breakage in aging bone contributes to its fragility. This process is accelerated with diseases such as osteoporosis (and osteopenia, its less severe form), a disease that arises due to an imbalance in bone regeneration activity. The regeneration cycle of bone is

governed by cells called osteoblasts and osteoclasts: osteoclasts break down and resorb bone, while osteoblasts rebuild bone. (A mnemonic: osteo**c**lasts — "c" — *c*ollect bone, while osteo**b**lasts — "b" — *b*uild bone.) When more resorption occurs than the deposition of new bone tissue, the overall bone mass density is decreased.

Osteoporosis effects a significant personal and economic toll worldwide. Osteoporosis increases the risk of fracture four-fold [7]; hip fracture is associated with excess mortality of between 8% and 36% [8]. In the United States alone, osteoporosis affects approximately 10.2 million adults over age 50 [9], and about 1.5 million adults experience a fracture each year [10]. The annual cost of managing osteoporotic fractures is in the tens of billions and is projected to increase as life expectancy increases [7, 11]. In Europe, the number of patients with disability due to osteoporosis is comparable to that of heart disease and greater than that of cancer [12].

Osteoporosis is diagnosed by measuring bone mineral density (BMD), which is typically accomplished via dual-energy X-ray absorptiometry (DXA or DEXA) [13] or quantitative computed tomography (QCT) [14]. DXA works by directing a high-energy X-ray beam and a low-energy X-ray beam at the body; the difference in attenuation of the two beams is used to estimate the amount of bone and of soft tissue. On the other hand, computed tomography (CT) uses X-rays from which tomographic images can be reconstructed by calculating the different attenuation rates by various tissues. Attenuation in CT scanning is measured according to Hounsfield scale, which is defined relative to the attenuation of water; bone absorbs X-rays at a higher rate and is thus assigned higher values on the Hounsfield scale. In QCT, Hounsfield units are converted from tomographic images of bone to estimate BMD. One primary difference between DXA and QCT is that DXA measures only areal bone mineral density, from which volumetric bone mineral density (or simply bone mineral density) is estimated, while QCT measures volumetric bone mineral density directly.

However, BMD, which effectively serves as a bulk measure of the quantity of bone (as determined by the presence of calcium and other minerals), has been shown to be an incomplete predictor of bone strength. While BMD can explain the variance in the mechanical strength of trabecular bone up to about 70%, a combination of BMD and architectural properties such as anisotropy can explain up to 90% [1, 15, 16, 17, 18]. In fact, osteoporotic bone structure is marked by its anisotropy; osteoporotic bone is observed to contain fewer trabeculae that lie transverse to the principal direction of loading than those that are parallel to the loading axis [1, 19]. For instance, in the vertebrae, where loads are primarily parallel to the spine, there are fewer horizontal trabeculae than vertical trabeculae. Moreover, the trabeculae parallel to the principal loading direction tend to maintain their original thickness (and in some cases can be even thicker), while the few transverse ones that remain are generally thinner.

1.1.2 Bone remodeling

Three mechanisms for remodeling — metabolic, adaptive, and microdamage remodeling — have been proposed to explain the changes in bone structure that occur with age and osteoporosis (Fig. 1.2) [1]. Metabolic remodeling describes a process of resorption (performed by osteoclasts) and rebuilding (performed by osteoblasts) of bone tissue that occurs uniformly throughout the bone. With age, an imbalance of osteoclast and osteoblast activity will result in uniform thinning of trabecular structure. Adaptive remodeling posits that trabeculae that undergo less loading are preferentially resorbed, and those that are more frequently loaded are preferentially rebuilt. In the spine, then, this would result in fewer horizontal trabeculae over time, with the resorbed bone tissue being used to rebuild and maintain vertical trabeculae. Microdamage remodeling, meanwhile, refers to preferential remodeling of trabeculae that undergo microdamage — small

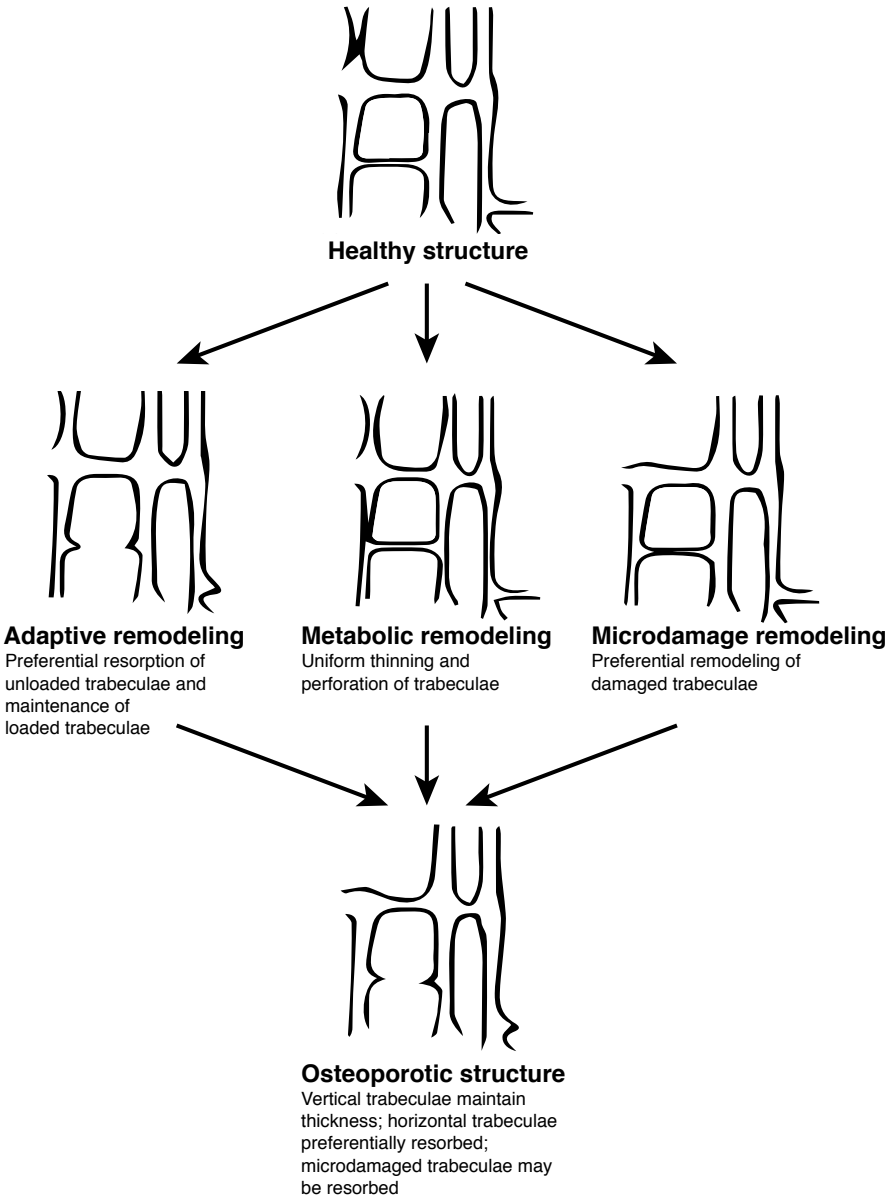

Figure 1.2: Schematic of how three mechanisms of bone remodeling — adaptive, metabolic, and microdamage — can explain osteoporotic trabecular architecture. Adapted with permission from McDonnell, McHugh, and O'Mahoney, *Ann. Biomed. Eng.* **35**, 170, 2007 [1].

cracks, called microcracks, that initiate in bone tissue may signal osteoclast activity of bone at the location of the microdamage.

No one of these three mechanisms alone can explain osteoporotic bone architecture; rather, a combination of these three mechanisms has been proposed to contribute to osteoporotic damage (Fig. 1.2). While (vertebral) osteoporosis results in fewer horizontal trabeculae than vertical trabeculae, with vertical trabeculae generally maintaining their original thickness, it has also been shown that the overall number of vertebral trabeculae lost with aging and osteoporosis is greater than that of horizontal trabeculae [19]. This cannot be explained by adaptive remodeling alone, since osteoclast activity would target unloaded (horizontal) trabeculae. Metabolic remodeling, particularly in the early stages of aging, could explain the vertical bone loss. Thomsen et al. [19] have observed that young, healthy vertebrae can contain about twice as many vertical trabeculae as horizontal trabeculae. If metabolic remodeling targets all trabeculae equally, then the absolute number of vertical trabeculae undergoing resorption would be greater than that of horizontal trabeculae.

Microdamage remodeling, meanwhile, addresses remodeling activity that targets damaged bone. It has been proposed that the presence of microdamage signals osteoclast activity, and that the spatial distribution of microcracks is random [20, 21]. Huiskes et al. have developed a model of bone remodeling that combines strain-signaled osteoblast activity with either uniform osteoclast activity (regulated by microdamage) or osteoclast activity that targets areas of disuse [20]. Simulations of this model in 2-D and in 3-D [21] in a subsequent work have corroborated *Wolff's law*, which states that bone remodels itself to adapt to the loading conditions under which is placed [22]. In other words, if the skeleton undergoes anisotropic loading where the loads are primarily along a preferred direction, then over time, the trabecular structure will remodel itself such that the bone is arranged to resist the loading in that direction. This typically results in a structure in

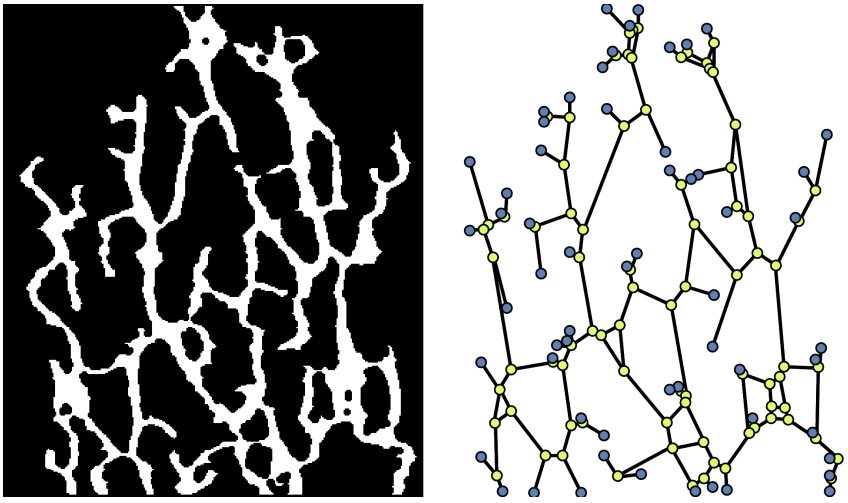

Figure 1.3: Binarized micro-CT image slice of vertebral trabecular bone (left) skeletonized and converted to a network (right).

which trabeculae are preferentially aligned along the direction of loading. As shown in the simulations of Huiskes et al. and Ruimerman et al., if the loading direction is rotated, then over time, the bone architecture will rotate along that direction as well [20, 21]. However, the adaptation of trabecular structure to changes in loading have yet to be confirmed in experiments on live specimens [23], but this may be due to the relatively short timescale of previous experiments compared to the timescale of bone adaptation [21].

1.2 Computational approaches

The web-like arrangement of trabecular bone calls to mind a network, i.e., a system of nodes, or vertices, that are connected by links, or edges. While the mathematical and computational infrastructure developed in the field of network science has been applied to a vast array of biological, social, ecological, and physical systems [24], including but very much not limited to vasculature, the brain, animal behavior, granular materials, and soil [25, 26, 27, 28, 29], it has rarely been applied to the study of trabecular bone [30].

In Chapter 2, we develop a novel network-based approach to modeling trabecular bone by "skeletonizing" micro-computed tomography (micro-CT) images of real human bone to extract the underlying topology, generating a network comprising links that represent trabeculae and nodes that represent the points where trabeculae intersect (Fig. 1.3). In doing so, we can represent trabecular bone in a compact mathematical form, as all of the information describing a network is contained in one matrix, called the adjacency matrix, from which topological measures can be extracted. Our approach stands in contrast to previous methods of trabecular analysis that primarily utilize specialized image processing techniques [18, 31]. However, since the networks are spatially embedded, we consider geometric properties in addition to length-scale-independent topological metrics in our analysis of trabecular bone.

To examine the mechanics of bone, we translate the networks to finite element models in which each trabecula is replaced by a beam, and we simulate compressive loading and deformation. While simplified, these models present a large reduction in computational time as compared to finer-grained "continuum" models used for *in silico* validation. The beam models allow us to relate the mechanical response of the bone to its topology and geometry at a range of scales. We examine the overall force-displacement response of the network as a whole, as well as the distribution of stress across beams.

Why does trabecular bone have the disordered, web-like structure that we observe in the human body? The answer may be due to an interplay of various factors: for instance, the anisotropy of trabecular bone may arise due to uniaxial loading (following Wolff's law), while its porosity allows it to hold marrow and blood vessels. To probe this, we may think of bone as the result of biological optimization — however, we do not know what is being optimized for. This is the inverse of more commonly-encountered problems: one may have some fixed quantity of material and must determine the optimal arrangement of this material in order to satisfy some objective(s). Using *multi-objective*

topology optimization (Chapter 3), we generate structures by optimizing objectives chosen to represent qualities that may be linked to the strength and function of bone: stiffness, surface area, and stability.

Topology optimization works as follows: starting from an initial density distribution, perform a finite element step that simulates mechanical deformation; perform an optimization step to update the density distribution; evaluate an objective function; and repeat until convergence. The objective function can be, for instance, a maximization of stiffness, surface area, or some other quantity. Combining multiple objectives, in our case as a weighted sum, gives multi-objective topology optimization. In this thesis, we generate topology-optimized bio-inspired structures that are not necessarily intended to mimic bone. Rather, we select the aforementioned three properties associated with bone and vary the respective weights of their objective functions to modulate the relative importance of each objective. In doing so, we analyze how changing these weights produce structures with varying strength and robustness.

We carry out similar analyses on topology-optimized bio-inspired structures as with real bone: skeletonization, network conversion, and mechanical simulation. In addition to simulating compressive loading in the linear regime, however, we implement a stress-based failure criterion to investigate fracture. To characterize failure locations, we apply community detection, a method of determining modularity in network structure. The development of algorithms for identifying community structure, as well as their application, is a major focus of network science. Community detection has been applied to a wide variety of topics including brain activity, social interactions, and ecological food webs [32, 33]. Most pertinently, however, it has previously been used to quantify the architecture of force chains in granular materials, which qualitatively resemble networks of connected filaments preferentially aligned with the direction(s) of loading [28], thereby evoking somewhat the anisotropic structure of trabecular bone.

1.3 Challenges in probing trabecular structure *in vivo*

Currently, analyzing the micro- and millimeter-scale structure of trabecular bone in humans requires high resolution images that cannot currently be acquired *in vivo*. The current standard for assessing the architecture of trabecular bone is micro-CT, or µCT, which can achieve resolution of order 10 µm voxel size or smaller (compare to average trabecular thicknesses, which are of order 200 µm). However, the large amount of ionizing radiation involved prevents its clinical application. Micro-CT is currently only applied *in vivo* to small animals. High-resolution peripheral quantitative computed tomography, or HR-pQCT, though, has been used to image bone architecture *in vivo* in distal extremities in human patients at a resolution of approximately 80 µm [34] — but this excludes imaging of vertebral trabecular bone, for example.

Magnetic resonance imaging (MRI), in contrast to X-ray tomography, does not involve ionizing radiation. However, patient motion severely limits the ability of MRI to resolve bone architecture. High resolution MRI such as micro-MRI can achieve a resolution of at best 140 µm in peripheral locations *in vivo* [35]. For *ex vivo* samples not subject to motion effects, micro-MRI can only achieve a resolution of 30 µm, poorer than that of micro-CT [36]. As we address in Chapter 4, however, it is possible to extract information regarding the texture of biological tissues, including trabecular bone, from k-space without acquiring a full image. We perform a *in silico* validation study of a novel magnetic resonance technique, and we identify a metric for classifying healthy and diseased trabecular bone from frequency-domain data.

1.4 Permissions and attributions

1. The content of Chapter 2 has previously appeared in A. Mondal, C. Nguyen, X. Ma, A. E. Elbanna, and J. M. Carlson (2019), *Phys. Rev. E* **99**, 042406. It is reproduced here with the permission of the American Physical Society.

2. The content of Chapter 3 is the result of a collaboration with D. Peetz, A. E. Elbanna, and J. M. Carlson and is based on a manuscript currently in submission and available at arXiv:1907.07860.

3. The content of Chapter 4 has previously appeared in C. Nguyen, K. J. Schlesinger, T. W. James, K. M. James, K. Masuda, R. L. Sah, and J. M. Carlson (2018), *R. Soc. Open Sci.* **5**, 180563 and is reproduced here under the terms of the Creative Commons Attribution License `http://creativecommons.org/licenses/by/4.0/`.

Chapter 2

Probing structure-function relationships with network models

2.1 Introduction

In this chapter, we capitalize on the network resemblance of trabecular bone and develop a streamlined modeling approach that draws from network science to relate architecture with mechanics.

The architecture of trabecular bone is typically characterized with histomorphometry, the image-analysis-based study of bone tissue to obtain quantitative information about its structure and remodeling [37, 38]. Modern histomorphometry is accomplished using high-resolution imaging, such as micro-CT, which can capture image resolution down to the order of a micron [39, 40]. However, the large amounts of radiation involved in high-resolution tomography limits its *in vivo* usage to distal extremities in humans [34]. In this study, we utilize high-resolution micro-CT images of cadaveric vertebral bone, from which we generate accurate 3-D reconstructions of trabecular volumes and extract histomorphometric parameters.

The web-like structure of trabecular bone closely resembles a network: each trabecula resembles a link, while the points at which multiple trabeculae meet, referred to here as branch points, resemble nodes. Hence, we capitalize on this resemblance by modeling trabecular bone as a network. We exploit the existing mathematical framework developed in network science to analyze the topology of trabecular bone in a streamlined fashion.

We begin by converting micro-CT images of trabecular bone into network models that are compactly represented in a mathematical form, in contrast to previous methods of trabecular analysis that involve specialized image processing techniques [18, 31]. To relate structure to mechanics, we also create two types of finite element models that respectively correspond to 3-D realizations of the bone images and of the network models.

We examine the statistical variability in architectural and mechanical properties across scales. At the smallest scales, we characterize individual trabeculae and branch points with network metrics. Moreover, we compute distributions of these metrics for a network derived from a volume of bone that may contain hundreds of trabeculae and branch points. For a mesoscale analysis, we coarse-grain an entire vertebral body into such volumes (Fig. 2.1) and compare distributions across these volumes.

Likewise, we analyze mechanical response across scales with simulated deformation of the bone models. The stress in one trabecula — here modeled as a beam in a finite element model — represents the smallest-scale mechanical measure, and mesoscale response is represented by the overall stiffness of bone volumes. We compare the stress distribution of a beam network and its stiffness with structural metrics. Analysis at the mesoscale reveals several correlations between architectural and mechanical quantities in bone.

2.2 Modeling bone as networks

2.2.1 Micro-CT image analysis

To develop network models of trabecular bone, we utilize a 37-µm resolution micro-CT image set obtained from the Bone 3D Project Team [41]. This set includes 970 axial image slices, each 2048 pixel × 2048 pixel (75 mm × 75 mm) in size, of vertebral body L3 from a human cadaver, imaged using the Scanco µCT 80 scanner. Stacked along the axial direction, the images encompass a volume with dimensions 75 mm × 75 mm × 35.9 mm.

Pre-processing of micro-CT images is performed with CT-analyser (CTAn) [42]. The raw images are binarized using the Otsu thresholding method [43]. All the images undergo a "despeckling" procedure to remove spurious pixels; all black or white clusters consisting of fewer than 100 pixels in three dimensions are removed. The stack is divided into small volumes of interest (VOIs) to facilitate future processing. Each VOI comprises a stack of 100 images that are each 100 pixel × 100 pixel, corresponding to a cube with dimensions $(3.7\text{ mm})^3$, or a volume of approximately 50 mm^3 (Fig. 2.1).

2.2.2 Generating networks

Network models of trabecular bone are derived using skeletonization, a process that isolates the medial axis of an image — the "skeleton" [44]. The medial axis of a 3-D object can be determined by fitting spheres such that each sphere touches the surface of the object at more than one point. Then the locus of the centers of the maximally fit spheres forms the medial axis. Due to the web-like structure of trabecular bone and the rod-like geometry of individual trabeculae, the medial axis of a section of trabecular bone typically resembles a set of connected lines that run through the centers of each of the trabeculae

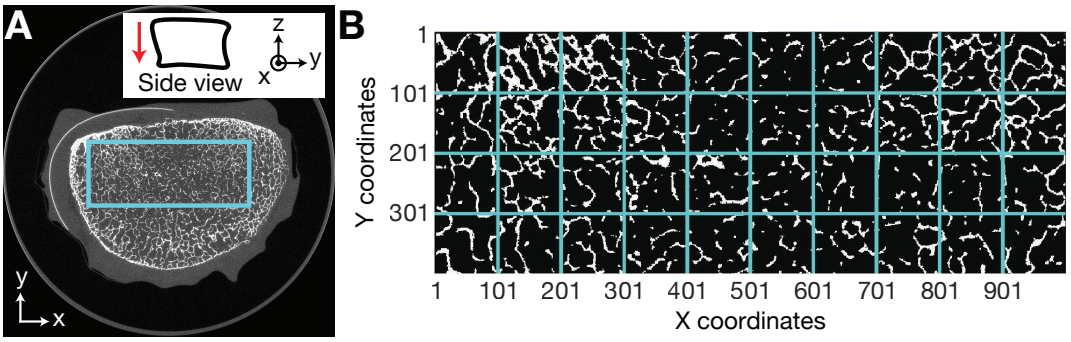

Figure 2.1: Trabecular bone images used in this study. A: micro-CT transverse image slice of human vertebral body L3 [41]. The highlighted region is divided into volumes of interest (VOIs) shown in B. The inset shows a schematic of a sagittal cross-section of a human vertebral body as it corresponds to our sample. The red arrow indicates the principal direction of loading. B: The selected region is divided into 100 pixel (3.7 mm) $\times$ 100 pixel tiles; each tile shown is the top image of a 100-image stack (Z-coordinate) that defines a VOI. The X, Y, and Z directions refer to the medial-lateral (eye-to-eye), anterior-posterior (front-to-back), and superior-inferior (head-to-foot, i.e., parallel to the spine) directions, respectively.

(Fig. 2.2). We use the Skeleton3D library [45] for MATLAB (MathWorks, Natick, MA) to compute the skeleton of each VOI. This is achieved by iteratively removing surface voxels from the volume in such a way that the topology of the sample is preserved. As a result, all branch points and cavities in the original shape remain after each iteration. This is repeated until what remains is a collection of segments no larger than one voxel thick [45].

The Skel2Graph library [45] for MATLAB is used to convert a skeleton into a network. Links are defined as individual trabeculae, and nodes as the branch points between trabeculae. The process of dividing the bone into VOIs results in isolated trabeculae in each VOI that "float" in space; these are removed, and a single connected component is isolated. The links are weighted with the average thicknesses of the individual trabeculae. Bone thickness is computed with the BoneJ plugin [46] for ImageJ (National Institutes of Health, Bethesda, MD).

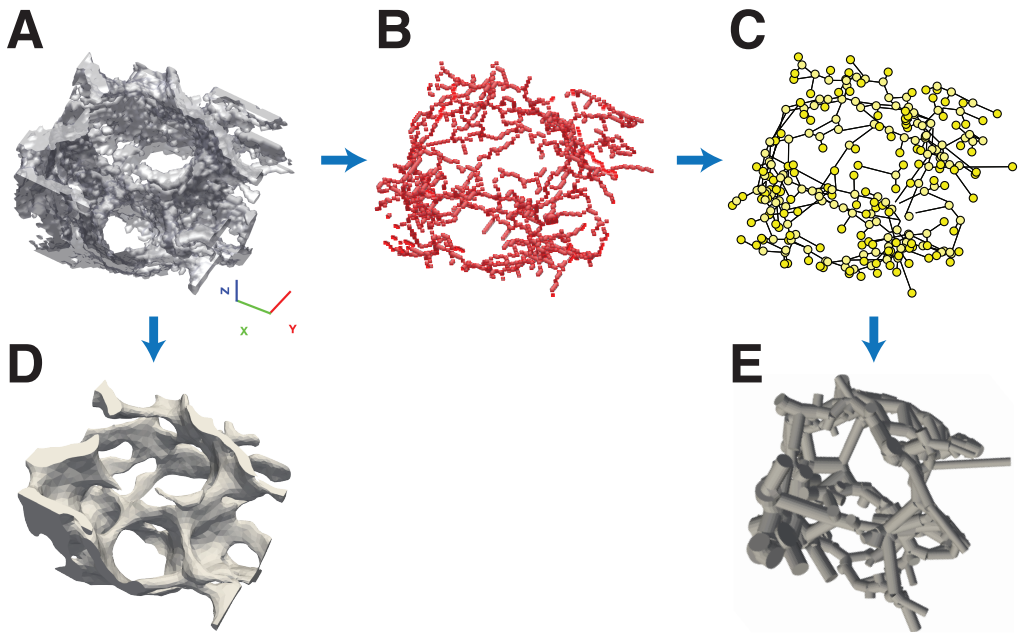

Figure 2.2: Trabecular bone modeling pipeline. Micro-CT image slices of bone are stacked to create a 3-D volume (A). The skeleton (B) is generated by iteratively thinning the volume until a one-voxel-wide line remains. Branch points in the skeleton are assigned as nodes (yellow circles) in a network (C), with edges representing trabeculae connecting the branch points. Endpoints of trabeculae created as a result of image segmentation are also assigned as nodes. A continuum finite element model (D) is generated by meshing the original bone images, while a beam-element model (E) is generated by converting each edge in the network to a beam, where the thickness of the beam is defined relative to the edge weight.

2.3 Structural analysis

We characterize the structure of bone by investigating histomorphometry, geometry, and network topology at the scale of individual trabeculae (of order 0.1 mm) and at the VOI scale (approximately a few mm). At the smaller scale, we determine characteristics of nodes and links, as well as their distributions within a VOI. At the larger scale, we compare the distributions of such characteristics across VOIs and examine the spatial distribution of structural properties (Fig. 2.3). We analyze a total of 40 VOIs, each measuring $(3.7\ \text{mm})^3 \approx 50\ \text{mm}^3$. Each VOI is small enough for structural and mechanical

properties to be calculated in a short amount of computational time while large enough to capture significant structural variation.

Topological characteristics of nodes considered here include degree and weighted degree. Degree refers to the number of links connected to a node, while weighted degree is the sum of the weights of the links connected to a node. Thus, the degree of a single node is an integer value, while the weighted degree is not necessarily an integer. For both of these measures, nodes of degree less than 3 are not considered, as the presence of these nodes is directly dependent on locations of the boundaries of VOIs. For example, nodes of degree 1 represent the ends of trabecular bone at the boundaries of VOIs. Nodes of degree 2, which are rare in trabecular bone and theoretically should not exist based on the definition of the trabecular networks, are the result of large, dense pieces of bone, which are classified as nodes by the Skel2Graph algorithm, connected to two trabeculae. Further details regarding network topological metrics are included in Appendix A.2.

For links, we consider geometric properties relevant to spatially-embedded networks: average thickness ("trabecula width"), link length, vertical orientation ("Z-orientation", Zo), and weighted vertical orientation ("weighted Z-orientation", Zo_w). We define Z-orientation as the dot product of the unit position vector of a link with the unit vector in the Z-direction (or superior-inferior direction, the primary loading axis in the spine). Z-orientation ranges from 0 to 1, where 0 and 1 refer to a link that is perpendicular and parallel to the Z-direction, respectively. Weighted Z-orientation is defined as the Z-orientation of a link multiplied by the corresponding weight of the link. We also analyze the average width of the voids ("pore width") between trabeculae. Pore width is a metric we introduce to examine the distribution of spaces between trabecula at the smaller scale. Further details regarding the calculation of these spatially-dependent metrics are included in Appendix B.

At the mesoscale, we compare averages of the above properties within each VOI across

the vertebral body. Following bone histomorphometry conventions, the average width of trabeculae in a VOI is called trabecular thickness, or Tb.Th, and the average of pore widths in a VOI is called trabecular separation or trabecular spacing, abbreviated Tb.Sp (Appendix A.1) [39, 46]. For weighted Z-orientation (but not unweighted orientation), we use the sum of the weighted Z-orientation of the links in a VOI as the VOI-scale measure, rather than the mean. We also determine the assortativity of each VOI, which is the tendency of nodes to be connected to other nodes that have similar properties. In this work, we specifically determine degree assortativity, the tendency of nodes to be connected to nodes of similar degree. Nodes with a high assortativity (near 1) are said to display assortative mixing and nodes with low assortativity (near -1) are said to display disassortative mixing. Networks with assortativity near 0 are called neutral. Furthermore, we compute the volume fraction (BV/TV), a traditional histomorphometric quantity, and the total number of links in the network model of each VOI.

Fig. 2.3A-G compares within-VOI (left) and across-VOI (right) distributions for seven structural metrics (degree, weighted degree, pore width/Tb.Sp, trabecula width/Tb.Th, Z-orientation, weighted Z-orientation, and link length). The within-VOI plots show distributions of each respective metric at the node/link scale for three representative VOIs. These illustrate the within-VOI statistical distribution of each metric for representative high, medium, and low values of the corresponding VOI-scale average. The across-VOI plots illustrate the spatial distribution of the average of each metric in each VOI. Fig. 2.3H-J illustrates only across-VOI distributions for three metrics: number of links, assortativity, and volume fraction, which are VOI-scale measures not defined at the individual node/link scale.

Distributions of degree (Fig. 2.3A) within a VOI consistently demonstrate a peak at degree 3 and a tail extending to larger degree values. In general, VOIs with a higher average degree and a higher peak at degree 3 also contain a few nodes of degree greater than

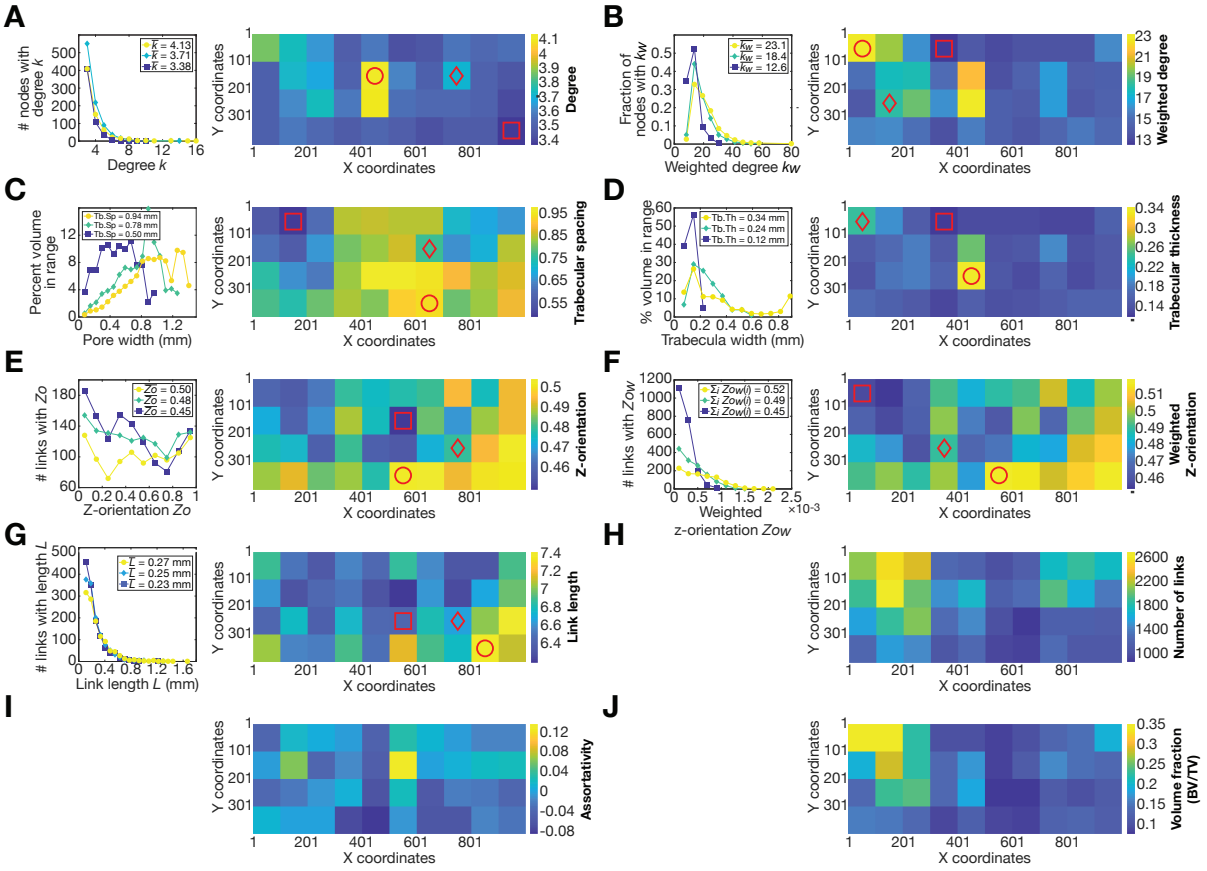

Figure 2.3: Distributions of structural metrics. A: degree; B: weighted degree; C: trabecular separation (Tb.Sp); D: trabecular thickness (Tb.Th); E: Z-orientation; F: weighted Z-orientation; G: link length; H: number of links; I: assortativity; J: volume fraction (BV/TV). Each panel consists of two plots, except for panels H, I, and J: the left plot illustrates the distribution of metrics at the node/link scale, and the right plot shows the distribution of metrics at the VOI scale. (Number of links (H), assortativity (I) and volume fraction (J) are only defined at the VOI scale.) The node/link-scale plots show distributions within three example VOIs; the mean (or sum, in the case of weighted Z-orientation) of each distribution is indicated in the respective top right corners. Values are binned, with markers indicating the midpoint of each bin, except for degree, which takes integer values. The VOI-scale plots illustrate the spatial distributions of structural metrics across the vertebral body. The color of each tile represents the average structural metric for one VOI. The three VOIs for which the histograms are plotted on the left are indicated on the right by shapes corresponding to their respective markers and illustrate results for representative high (yellow circles), mid-range (light green/blue diamonds), and low (dark blue squares) values of the corresponding VOI scale metrics.

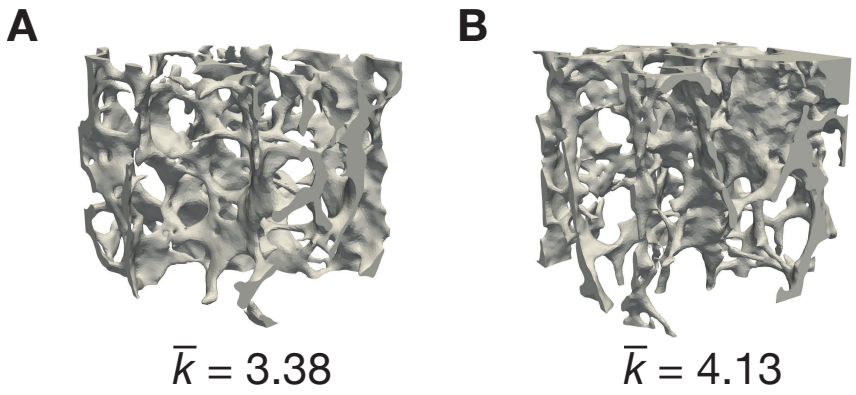

Figure 2.4: Illustration of 3-dimensional structure for two example VOIs. A: This sample corresponds to the example low-degree VOI indicated in Fig 2.3A and has an average degree of 3.38, the smallest of any of the VOIs analyzed in this work. B: This sample corresponds to the example high-degree VOI in Fig 2.3A and has an average degree of 4.13, the largest degree of all VOIs.

10. The yellow square-marked curve in Fig. 2.3A, corresponding to the largest degree, is one example, containing nodes of degree 10, 11, 13, 15, 16, 22, 24, 37, 72, and 110. Nodes of degree greater than 20 are not shown so that the low degree behavior of the distributions is visible. These nodes are responsible for the yellow curve having the highest average degree, despite the fact that the light blue diamond-marked curve encompasses more nodes of degree 3 through 9. Nodes of such high degree are uncommon in most of the trabecular bone samples analyzed in this work. They tend to exist only in VOIs that contain dense regions of bone. These regions do not share the characteristic rod-like geometry of most trabecular bone, but are connected to many trabeculae due to their large surface area. In the network conversion process, these regions are approximated as nodes of unusually high degree.

To illustrate how the 3-dimensional structure of VOIs varies for different values of average degree, Fig. 2.4 shows the continuum models generated by meshing the VOIs with the smallest (Fig. 2.4A) and largest (Fig. 2.4B) average degrees. These correspond to the blue square-marked tile and the red circle-marked tile in the right panel of Fig. 2.3A. Fig. 2.4A displays a web-like structure throughout its volume with visible trabeculae.

Fig. 2.4B displays an example of a VOI that contains a node of incredibly high degree. This node is located in the upper left corner of the the figure, where the VOI contains a dense section of bone.

The distributions of weighted degree (Fig. 2.3B) consistently display peaks between 10 and 15 while having significantly smaller fraction of nodes of weighted degree less than 10 and greater than 20. Certain VOIs have significantly higher weighted degree due to the presence of high degree nodes connected to links of large weight. These nodes can have weighted degrees in the hundreds, while the majority of nodes have weighted degrees less than one hundred. As a result, full distributions of the weighted degree of VOIs are heavily right-skewed. In Fig. 2.3B, all three of the VOIs have such high weighted degrees; we only show the nodes with weighted degree between 0 and 60 so that the shape of each distribution is visible. Despite only showing a fraction of the full range of this plot, we only obscure about 0.2% of the nodes in each of the three distributions, which make up the long tails of each of the distributions.

The trabecular separation Tb.Sp of a VOI (Fig. 2.3C) varies greatly across the bone volume, ranging from 0.5 to 1.0 mm. Distributions of pore width within a VOI also vary in shape. The dark blue square-marked VOI, corresponding to the lowest Tb.Sp, exhibits a relatively symmetric distribution centered around 0.5 mm, while the distributions of the green diamond (mid-range Tb.Sp) and yellow (largest Tb.Sp) circle-marked VOIs are peaked at higher pore width values, with a heavy tail at low Tb.Sp.

The trabecular thickness (Tb.Th) (Fig. 2.3D) of a VOI ranges from 0.12 to 0.35 mm, but the majority of VOIs have a Tb.Th less than 0.2 mm. The distributions of trabecula width within a VOI tend to have a sharp peak at small widths around 0.15 mm followed by a tail. The length of the tail reflects the size of the Tb.Th, with the dark blue square-marked distribution having the shortest tail and smallest Tb.Th.

The distributions of Z-orientation (Fig. 2.3E) indicate that some VOIs (e.g., the blue

square-marked distribution with the smallest average Z-orientation) contain more trabeculae oriented perpendicular to the Z-axis, while others have more trabeculae oriented along the Z-axis (e.g., the yellow circle-marked distribution with the highest average Z-orientation). Overall, the mean Z-orientation does not vary greatly between the VOIs and ranges from 0.45 to 0.5, where the lower limit indicates VOIs that contain a slight prevalence of trabeculae oriented transverse to the Z-axis.

The distributions of weighted Z-orientation (Fig. 2.3G) consistently display a decay with increasing length. The VOI-scale color map illustrates the sum of all weighted Z-orientation values in each VOI, rather than the mean, in order to facilitate comparison with VOI-scale (unweighted) Z-orientation. While weighted Z-orientation at the link scale ranges from 0 to 2.2×10^{-3}, it ranges from 0.45 to 0.52 at the VOI scale. This narrow range can be attributed to our general observation that the sum of the thicknesses of the links in a VOI is usually roughly twice that of the sum of the thickness of each link multiplied by its Z-orientation. Thus, when dividing these quantities to get the weighted Z-orientation, we find values that are close to 0.5.

Distributions of link length (Fig. 2.3G) consistently demonstrate a large decaying behavior, with each VOI having hundreds of links about 0.2 mm long but fewer than 20 links 0.9 mm or longer. The average link length of a VOI is heavily dependent on the range of lengths of the VOI. For instance, the yellow circle-marked VOI, which has the largest average link length of all VOIs, contains links as long as 1.7 mm, while the longest links in the blue square-marked VOI, which has the shortest average link length, are about 1.2 mm.

The number of links in the network model of each VOI varies greatly over the analyzed region (Fig. 2.3H). The network with the fewest links contains about 950 links, while the network with the greatest contains about 2600 links. However, a majority of networks contain fewer than 1500 links.

Fig. 2.3I shows that the VOIs analyzed here display neutral mixing (assortativity near 0), with the assortativity values ranging from -0.08 to 0.12. This indicates that the nodes in these trabecular bone networks show no strong tendency to be connected with nodes of either similar or dissimilar degree.

The majority of the VOIs have a volume fraction less than 0.2 (Fig. 2.3J). Seven adjacent VOIs on the left side of the plot have slightly higher volume fraction, signifying a denser region of bone spanning that section.

Table 2.1 contains the Pearson correlation coefficients (r-values) and corresponding probability values (p-values) for each pair of structural metrics, with significant correlations highlighted in bold. We define a weak correlation as corresponding to the absolute value of r-values ranging from 0 to 0.3, moderate correlation as 0.3 to 0.6, and strong correlation as 0.6 to 1; we assert that a correlation coefficient is significant if $p \leq 0.05$. Assortativity and weighted degree are significantly correlated with all of the other structural metrics. Volume fraction, Z-orientation, weighted Z-orientation, and link number are significantly correlated with all metrics except link length. Trabecular spacing is not significantly correlated with trabecular thickness or link length. Trabecular spacing is strongly negatively correlated with volume fraction, as is expected, and is also moderately correlated with Z-orientation. That is, a VOI with large average pore width tends to contain links that are less aligned with the vertical axis. Trabecular thickness is moderately negatively correlated with Z-orientation and weighted Z-orientation. Hence, in our sample, VOIs with thicker trabeculae on average may tend to contain trabeculae less aligned with the vertical axis.

Weighted Z-orientation is negatively correlated with both the number of links in a VOI and the volume fraction. Fig. 2.3F shows that the VOIs with high weighted Z-orientation are in the regions with the fewest links (Fig. 2.3H) and the lowest volume fraction (Fig. 2.3J). We were initially surprised by this result. However, for the bone

Metric	A	k	k_w	BV/TV	Tb.Sp	Tb.Th	L	Zo	Zo_w	No. links
A	—	**0.7219**, **0.001**	**0.6959**, **0.001**	**0.5610**, **0.001**	**-0.3207**, **0.0437**	**0.7260**, **0.001**	**0.6279**, **0.001**	**-0.3647**, **0.0207**	**-0.4550**, **0.0032**	**0.4757**, **0.0019**
k	—	—	**0.8651**, **<0.001**	**0.5715**, **< 0.001**	-0.2712, 0.091	**0.8730**, **< 0.001**	**0.6925**, **< 0.001**	**-0.6229**, **< 0.001**	**-0.7077**, **< 0.001**	**0.5208**, **< 0.001**
k_w	—	—	—	**0.7575**, **<0.001**	**-0.4083**, **0.0089**	**0.9051**, **< 0.001**	**0.7026**, **< 0.001**	**-0.5411**, **< 0.001**	**-0.6593**, **<0.001**	**0.5686**, **< 0.001**
BV/TV	—	—	—	—	**-0.8193**, **< 0.001**	**0.5040**, **<0.001**	0.2792, 0.0810	**-0.4630**, **0.0026**	**-0.6022**, **<0.001**	**0.8673**, **<0.001**
Tb.Sp	—	—	—	—	—	-0.1008, 0.5358	0.1522, 0.3484	**0.3169**, **0.0463**	**0.4665**, **0.0024**	**-0.9047**, **<0.001**
Tb.Th	—	—	—	—	—	—	**0.8672**, **<0.001**	**-0.4492**, **0.0036**	**-0.5229**, **<0.001**	**0.3225**, **0.0424**
L	—	—	—	—	—	—	—	-0.1569, 0.3337	-0.2063, 0.2016	0.0168, 0.9180
Zo	—	—	—	—	—	—	—	—	**0.9626**, **<0.001**	**-0.4578**, **0.0030**
Zo_w	—	—	—	—	—	—	—	—	—	**-0.6037**, **<0.001**
No. links	—	—	—	—	—	—	—	—	—	—

Table 2.1: Structural metrics at the VOI scale. A: assortativity; k: degree; k_w: weighted degree; BV/TV: volume fraction; Tb.Sp: trabecular separation; Tb.Th: trabecular thickness; L: link length; Zo: Z-orientation; Zo_w: weighted Z-orientation; No. links: number of links. Pearson correlation coefficient r and corresponding p-values between the structural metrics (Fig. 2.3) are shown. In each cell, the upper value is r and the lower value is p. Significant correlations with p less than 0.05 are highlighted in bold.

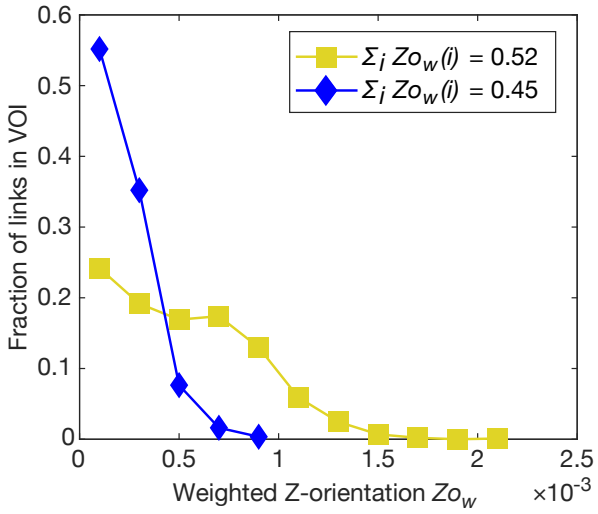

Figure 2.5: Distributions of weighted Z-orientation illustrating differences between high average Zo_w VOIs (yellow squares) and low average Zo_w VOIs (blue diamonds). The distribution of the representative high Zo_w VOI (marked in Fig. 2.3F by a circle) is much broader and displays a heavier tail compared to the narrower distribution of the representative low Zo_w VOI (marked in Fig. 2.3F by a square).

sample shown in Fig. 2.1, we observe that VOIs with lower volume fraction have a larger fraction of thicker links aligned with the Z-axis. Fig. 2.5 shows the distribution of weighted Z-orientations for the VOIs with the highest (yellow diamond-marked curve) and the least (blue diamond-marked curve) weighted Z-orientation. The yellow curve furthermore has among the fewest links of all VOIs and one of the lowest volume fractions, while the blue curve has among the most links and one of the largest volume fractions. The yellow distribution has a larger fraction of links with $Zo_w > 0.5$ than the blue distribution. We find that this is true for all VOIs with higher average weighted Z-orientation but low volume fraction and low number of links; they tend to have a larger range of weighted Z-orientation with a larger fraction of vertically oriented links.

We use principal component analysis (PCA) to identify uncorrelated metrics that explain the majority of the variation in the VOI mesoscale structural data (Fig. 2.3). We examine the fraction of the total variance in structural metrics explained by each

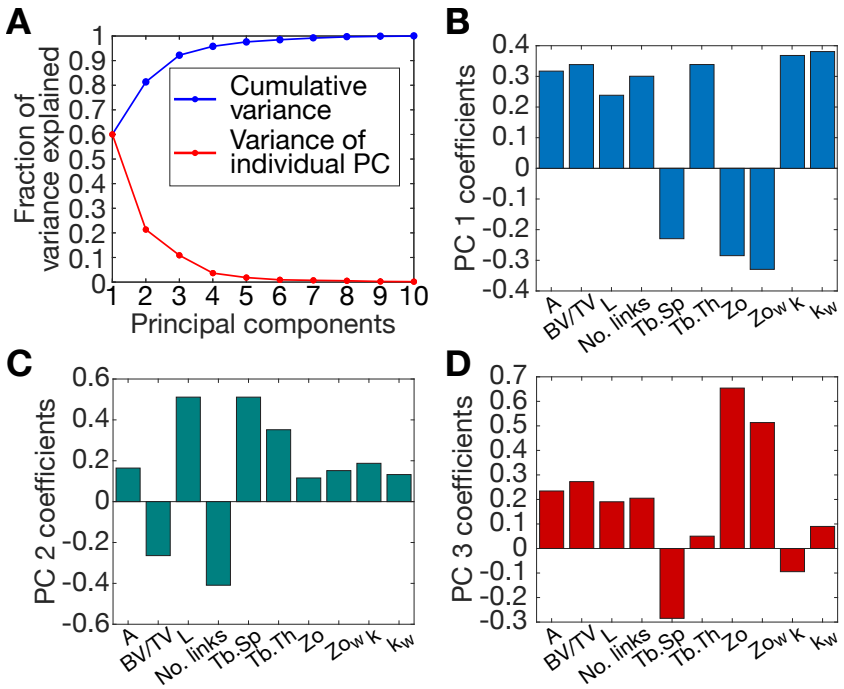

Figure 2.6: Principal component analysis of structural metrics. A: Fraction of variance explained by each principal component. The (upper) blue curve indicates the fraction of cumulative variance explained, while the (lower) red curve indicates the fractions explained by each principal component. The first three principal components explain 92.1% of the total variance in the structural metric data. B-D: Correlation coefficients of the first three principal components of the structural metric data feature space. PC 1, which explains about 60% of the data, only moderately or weakly correlates to any of the individual metrics. This is also true for PC 2, which explains about 21% of the variance in the data. Z-orientation is strongly correlated to PC 3, which explains about 11% of the variance in the data.

of the principal components (PCs) individually and cumulatively (Fig. 2.6A). The first PC explains approximately 60% of the variance, while the second and third explain approximately 21% and 11% respectively. In total, they explain approximately 92% of variance in the data. Since all the other components explain less than 10% of the variance in the data, we focus further analysis on only the first three PCs.

Fig. 2.6B-D shows the correlation coefficients between the structural metrics and each of the first three PCs. PC 1 and PC 2 are either weakly or moderately correlated to all of the metrics. Notably, all of the correlation coefficients in PC 1 are relatively similar

(between 0.25 and 0.40). PC 3 is strongly correlated to Z-orientation and moderately correlated to degree and weighted Z-orientation. PC 1 and PC 2 explain the majority of the variance in the structural metrics and are at best moderately correlated to the individual structural metrics. This result indicates that no smaller subset of the metrics (or linear combinations of them) can be used to capture the majority of the variance in the data, despite the significant correlations between almost all the structural metrics (Table 2.1).

2.4 Mechanical simulations

2.4.1 Finite element analysis

To analyze mechanical response, we convert the bone networks into finite element models that consist of beam elements representing each link. We refer to these as "beam models" (Fig. 2.2). We also construct continuum models generated from meshing the original micro-CT images (Fig. 2.2) to serve as an *in silico* validation of the beam models. We analyze both the bulk force-displacement response to compressive loading of the beam models and the distribution of stress in the beams. We individually carry out this analysis for each VOI in Fig. 2.1. Furthermore, we investigate how the structural properties of trabecular bone contribute to its mechanical response. We calculate the stiffness of the bone network in each VOI, and investigate correlations between the effective moduli and the structural metrics shown in Fig. 2.3.

We develop the beam models by converting each link in a network to a beam element (Fig. 2.2). The beam elements are rigidly connected such that, under deformation, the angle between two beams remains the same. The resulting models function as 3-D realizations of the network model. Simulations with the continuum models, which are

full-scale mesh reconstructions, are used to validate the simulation results of the beam model. The beam-element and continuum models are analyzed in Abaqus FEA (Dassault Systèmes, Vélizy-Villacoublay, France). Compared to the continuum models, the beam models correspond to a reduction in the degrees of freedom by about one order of magnitude, and require about an order of magnitude less computation time to solve.

We simulate compressive (top to bottom) loading in the linear-elastic regime. The elastic modulus is constant across a model and set to 10 GPa, and the Poisson ratio is set to 0.16, following ranges reported for trabecular bone in the literature [47, 48]. However, since the analysis is linear-elastic, a different choice of values simply corresponds to a linear scaling of the results.

The topmost and bottommost nodes of the VOI are identified as those lying in the transverse planes on the top and bottom of the VOI. The bottom nodes are held fixed in all dimensions, while the top nodes are displaced slowly in the -Z (superior-inferior) direction at a constant loading rate.

For each VOI, we validate the beam model by comparing results of the simulated compression with that of the continuum model, using the continuum result as an *in silico* validation. In the linear-elastic regime, initial comparisons (not shown) of the force-displacement curves indicate that the beam model has lower stiffness compared to the continuum model. In order to match the stiffness of the beam model to the continuum model, the radius of each beam was increased. For the example VOI shown in Fig. 2.7, an overall scale factor of 1.55 was required to match the force-displacement response (Appendix B.3). Our use of the scale factor is attributed to geometric differences between the beam and the continuum models. The cross-section of a trabecula is not exactly circular, but is approximated as circular in the formulation of the beams in the finite element model. Using a square cross-section for the beams while keeping the same thickness increases the overall cross-sectional area of the model and would slightly

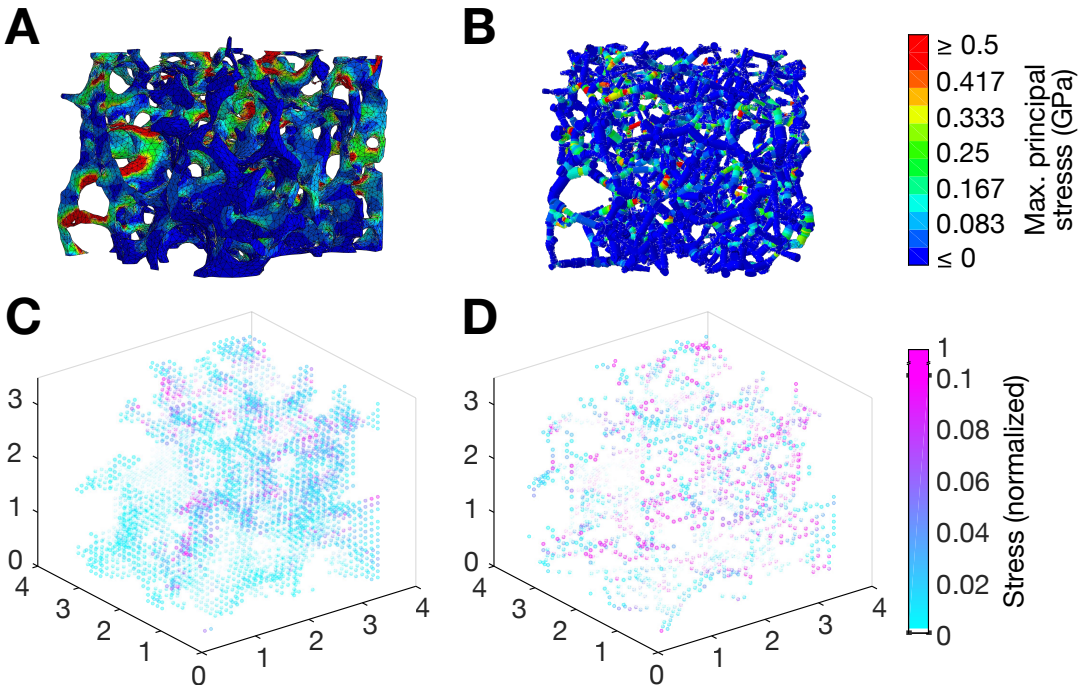

Figure 2.7: Finite element models of trabecular bone, for a sample VOI. The continuum model (A) and beam-element model (B) generated from the same VOI are compressed from the top. Colors show maximum principal stress in each element at the end of the simulation. C-D: Coarse-grained spatial distributions of maximum principal stress for the continuum (C) and beam-element (D) models. Each model is divided into a regular grid of $(0.11\ \text{mm})^3$ bins; each point corresponds to the average stress in one bin. Stress is normalized to the highest stress value (measured for a single element) in each model.

reduce but not entirely eliminate the scale factor. Moreover, while the individual beams have uniform thickness, the continuum model trabeculae have inhomogeneous thickness. Additionally, while the beam model approximates the branch points as nodes, the branch points in the continuum model are regions of bone with significant bulk properties that add to the stiffness of trabecular bone. The models used to produce the results shown here contain beams with circular cross-sections.

2.4.2 Stress distributions

Fig. 2.7A illustrates the stress states of each element of the beam and continuum models at the end of the simulations of linear compressive loading, colored according to the stress in each element. Here, stress refers specifically to maximum principal stress, the first (diagonal) element of the stress tensor under a transformation to a coordinate system with no shear stress. Because the two models have different numbers of elements and different types of elements (beams in the beam model, tetrahedral elements in the continuum model), to facilitate a comparison of the spatial stress distribution, we coarse-grain each model by dividing the $(3.7\text{ mm})^3$ VOI into a regular grid of $(0.185\text{ mm})^3$ bins and average the stress in each bin (Fig. 2.7B). While the locations of high stress are similar, the highest stresses in the continuum model are almost an order of magnitude greater than the beam model. (Note that Fig. 2.7B plots stress normalized by the maximum stress in one individual element for each model.) Both models exhibit a low-to-high-stress gradient along the +Z (superior-inferior) direction. However, this gradient is more pronounced for the beam model, while the continuum model contains greater spatial variation in stress. A trabecula is typically non-uniform in thickness, and can contain significantly thinner regions, but the network conversion process averages the thickness over a trabecula to produce the beam model. Hence, the continuum model can contain much thinner regions than the beam model, as well as relatively sharp corners that are smoothed in the beam model but which could be regions of localized stress in the continuum model.

During loading, the stress carried by individual beams in the VOI varies significantly. Fig. 2.8 shows the distribution of normalized stress in the beam model sample (Fig. 2.7A) undergoing compressive loading in the linear regime. While Fig. 2.8 shows the distribution of stress during the final timestep of loading, the shape of this distribution remains

constant in the linear regime for all timesteps. We define the parameters $\zeta_{0.001}$ and $\sigma_{0.9}$ to characterize this distribution, where $\zeta_{0.001}$ is the fraction of beams with normalized stress less than or equal to 0.001, and where ninety percent of beams bear a stress less than or equal to $\sigma_{0.9}$. In the VOI shown in Fig. 2.8, $\zeta_{0.001} = 0.340$ and $\sigma_{0.9} = 0.153$. For the VOIs studied in this work, the average value of $\zeta_{0.001}$ is 0.410, while the average value of $\sigma_{0.9} = 0.136$. $\zeta_{0.001}$ ranges from 0.3 to 0.6 and $\sigma_{0.9}$ ranges from 0.038 to 0.224 across all VOIs.

Note, however, that each beam has a different volume. We also determine alternative parameters $\zeta'_{0.001}$ and $\sigma'_{0.9}$ that account for the different volumes by expressing the cumulative normalized stress distribution over volume fraction rather than number of beams: $\zeta'_{0.001}$ represents the fraction of the total bone volume taken up by beams with normalized stress less than or equal to 0.001, and ninety percent of volume fraction bears a stress less than or equal to $\sigma'_{0.9}$. The average values of $\zeta'_{0.001}$ and $\sigma'_{0.9}$ are 0.428 and 0.067, respectively. $\zeta'_{0.001}$ ranges between 0.330 and 0.815, while $\sigma'_{0.9}$ ranges between 0.0017 and 0.125. Corresponding distributions of stress are illustrated in Fig. B.2 of Appendix B.

2.5 Relating structure and mechanics

We investigate the relationship between structural properties — histomorphometric, geometric, and network-topological metrics — and mechanical properties at both the individual link (or node) scale and the VOI mesoscale.

2.5.1 Individual link scale

At the scale of individual links, we analyze the stress borne by each link during the final timestep of compression in our simulations. We compare link structural features to the distribution of stresses about the links to determine whether any structural properties

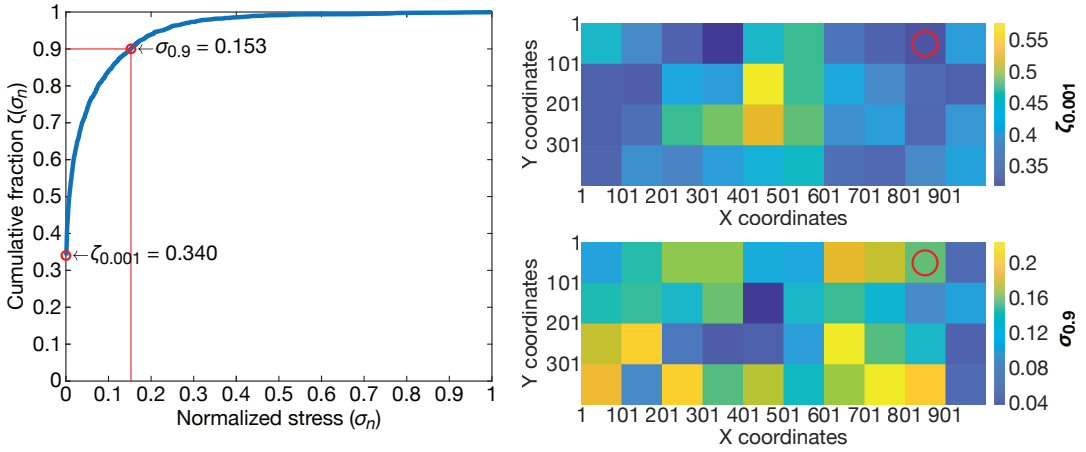

Figure 2.8: Distributions of stress. Left: Distribution of normalized maximum principal stress in the beam elements of an example beam model (Fig. 2.7) under compressive loading in the linear regime. To calculate normalized stress σ_n, we normalize stress σ with the largest value of stress in a beam at the final timestep of the compressive loading simulation. The function ζ is the fraction of the beams that bear a normalized stress less than or equal to σ_n. $\zeta_{0.001}$ is defined as the fraction of beams that bear a normalized stress less than or equal to 0.001 and $\sigma_{0.9}$ is defined as the normalized stress that satisfies the equation $\zeta(\sigma_{0.9}) = 0.9$. In this VOI, 34% of the beams bear a normalized stress less than 0.001 ($\zeta_{0.001} = 0.340$), while 90% of beams bear a normalized stress less than or equal to 0.153 ($\sigma_{0.9} = 0.153$). Right: Spatial distributions of $\zeta_{0.001}$ and $\sigma_{0.9}$ across the sample. The example VOI is indicated by the red circle.

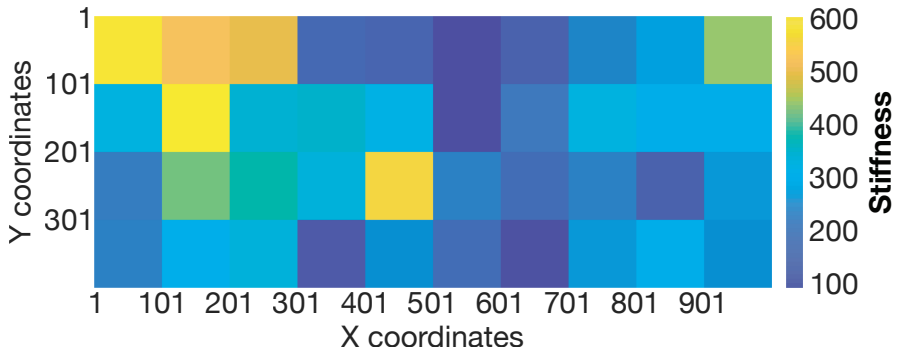

Figure 2.9: Spatial distribution of stiffness across the vertebral body. The color of each tile represents the stiffness for one VOI.

Metric	S	Width	L	Zo	Zo_w
Stress (S)	—	-0.0331, 0.2810	0.0453, 0.2106	**-0.1320**, **0.0081**	-0.0013, 0.3641
Trabecula width	—	—	0.0294, 0.3408	-0.0868, 0.0797	**0.5137**, **< 0.001**
Link length (L)	—	—	—	**-0.0792**, **0.0462**	-0.0187, 0.2003
Z-orientation (Zo)	—	—	—	—	**-0.4985**, **< 0.001**
Weighted Z-orientation (Zo_w)	—	—	—	—	—

Table 2.2: Comparing stress with structural metrics at the individual link scale. Pearson correlation coefficient r and corresponding p-values between structural metrics and stress at the individual link scale are shown. In each cell, the upper value is r and the lower value is p. The values reported here are the averages of the coefficients over all VOIs. Significant correlations with p less than 0.05 are highlighted in bold.

are correlated to mechanical properties at the individual link scale. For each VOI, we calculate Pearson correlation coefficients and corresponding p-values between the stresses and link metrics. We present the average of the r and p-values across all VOIs in Table 2.2. We observe significant but weak correlations between stress and Z-orientation. Weighted Z-orientation is also significantly correlated with both Z-orientation and trabecula width, which is unsurprising due to its definition. Additionally, the length of the links is weakly, negatively correlated to Z-orientation.

2.5.2 VOI scale

At the VOI mesoscale, we analyze the stiffness of each VOI. Stiffness is defined as the slope of the force-displacement curve in the linear regime. Fig. 2.9 shows the spatial

distribution of stiffness across all VOIs. In the linear-elastic regime, the stiffness is a constant over the loading process for each individual VOI. Fig. 2.10 compares stiffness with ten network-topological, geometric, and traditional histomorphometric metrics.

We find significant linear correlations between the stiffness of each sample and all structural metrics shown in Fig. 2.3. Stiffness is most strongly correlated with volume fraction ($r = 0.857$, $p < 0.001$), number of links ($r = 0.807$, $p < 0.001$), and weighted degree ($r = 0.791$, $p < 0.001$). We also observe significant, strong positive linear correlations between stiffness and degree ($r = 0.627$, $p < 0.001$) as well as stiffness and Tb.Th ($r = 0.623$, $p < 0.001$). Stiffness exhibits a significant, strong negative linear correlation with Tb.Sp ($r = -0.647$, $p < 0.001$). We also observe moderate but significant correlations between stiffness and assortativity ($r = 0.592$, $p < 0.001$), link length ($r = 0.400$, $p = 0.011$), Z-orientation ($r = -0.443$, $p = 0.004$), and weighted Z-orientation ($r = -0.555$, $p < 0.001$). These results indicate that the number of links, degree, weighted degree, and assortativity can be informative network topological features to supplement BMD in characterizing bone strength. Furthermore, weighted Z-orientation can be an informative geometric property of the spatially-embedded network, in addition to volume fraction, trabecular spacing, and trabecular thickness for histomorphometric analysis. The strong correlation between stiffness and volume fraction shows that trabecular networks tend to be stiffer as the ratio of bone volume to pore volume increases, and the strong correlation between stiffness and weighted degree indicates that stiffer trabecular networks have larger numbers of thicker trabecula connected to each other.

To determine whether all ten metrics are necessary to predict stiffness, we performed a multiple linear regression using the following model:

$$y = \beta_0 + \beta_1 x_1 + \beta_2 x_2 + \ldots + \beta_n x_n, \tag{2.1}$$

	β_i (fit)	Standard error	p
Intercept	0	0.057	1
Assortativity	0.009	0.097	0.927
Degree	**-0.635**	**0.191**	**0.002**
Weighted degree	**0.872**	**0.295**	**0.005**
Volume fraction	0.872	0.215	0.59
Tb.Sp	**0.416**	**0.192**	**0.038**
Tb.Th	-0.172	0.277	0.053
Link length	**-0.699**	**0.299**	**0.026**
Z-orientation	**0.753**	**0.355**	**0.042**
Weighted Z-orientation	**1.30**	**0.230**	**< 0.001**
Number of links	**0.914**	**0.287**	**0.004**

Table 2.3: Standardized linear coefficients, standard errors, and p-values for a multiple linear regression model relating stiffness with the ten structural metrics. Metrics with $p < 0.05$ are highlighted.

where y corresponds to stiffness and the x_i correspond to each of the structural metrics ($n = 10$). The data is standardized prior to fitting, and the standardized linear coefficients β_i are listed in Table 2.3.

There are forty different observations included in the regression analysis, one for each VOI. These observations correspond to the ten metrics calculated for each VOI. We find that the linear model is a significantly better fit to the data ($p < 0.001$) than a constant model under the F-test, and that the ten metrics are strongly predictive of stiffness (coefficient of determination $r^2 = 0.905$). Furthermore, significance values for

each of the individual metrics (Table 2.3) indicate the significant contribution of seven metrics to the prediction of stiffness: degree, weighted degree, trabecular spacing, link length, Z-orientation, weighted Z-orientation, and the number of links. Most notably, volume fraction does not contribute significantly in the linear model, despite its strong correlation with stiffness. Furthermore, removing any of these seven metrics, as well as Tb.Th, from the model decreases the adjusted r^2 (Appendix B.5), which penalizes the number of explanatory variables in the model. For a linear model containing only the aforementioned seven significant metrics, adding any additional variable to the model also decreases the adjusted r^2. This indicates that these seven metrics are the most informative metrics in predicting stiffness with a multilinear model. The model with ten significant metrics has an adjusted $r^2 = 0.872$. The model with seven significant metrics has an adjusted $r^2 = 0.882$.

We also performed a multiple linear regression using the model described by Eq. (2.1), with the principal components shown in Fig. 2.6. A model including all ten principal components has the same r^2 and adjusted r^2 as the model shown in Table 2.3. A model including the principal components which contribute most significantly to the prediction of stiffness ($p < 0.05$) has an r^2 of 0.878 and an adjusted r^2 of 0.864. These values indicate that a model consisting of the significant principal components does not perform as well as a model with the significant structural metrics.

2.6 Discussion

We introduce a network characterization of bone that provides a new framework for analyzing bone architecture. This approach incorporates existing mathematical and computational methods developed for graph theory and network science with finite element analysis, directly relating topological, geometric, and mechanical properties of

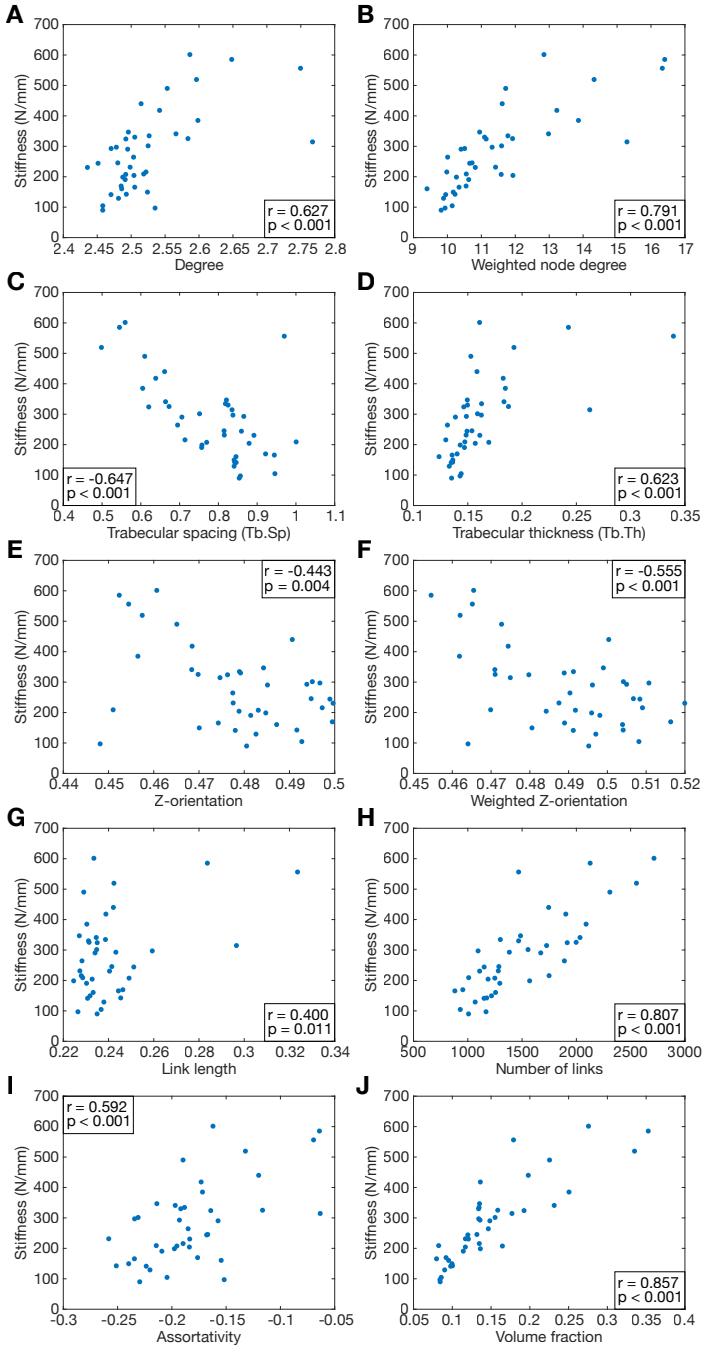

Figure 2.10: Stiffness compared with structural metrics at the VOI scale. For each VOI, the stiffness is plotted against the average degree (A), weighted degree (B), trabecular spacing (C), trabecular thickness (D), Z-orientation (E), weighted Z-orientation (F), and link length (G), as well as the overall number of links (H), assortativity (I), and volume fraction (J).

trabecular bone. Moreover, the beam models developed here provide streamlined, efficient alternatives to traditional methods of mechanical analysis of bone, which depend on computationally expensive image processing methods to conduct structural and finite element analysis. In this chapter, we use the network characterization and beam models to analyze bone structure and mechanics at the scale of individual trabeculae and at the scale of 50 mm^3 volumes of interest. Further studies will involve investigating trabecular bone at larger scales, extending to the entirety of the vertebra.

Our method of generating beam models of trabecular bone through skeletonization has some similarities with the network representation of soil samples developed in [29], as well as 3-D Line Skeleton Graph Analysis (LSGA) developed specifically for trabecular bone in [49]. LSGA analyzes the mechanical properties of trabecular bone by skeletonizing bone images and converting the skeletons into FEM beam models. LSGA also achieves an improved force-displacement curve fit with a more detailed bone model only after the thickness of the beams is increased. However, unlike the LSGA method, we use network science methods to further analyze the bone topology in addition to creating beam models. Additionally, we use the network and beam models to characterize trabecular bone not only at the VOI scale, but also at the scale of individual trabeculae, which is not analyzed with LSGA.

We analyzed the within-VOI distribution of network-topological, geometric, and traditional histomorphometric properties at the sub-millimeter scale (the level of individual links), as well as the spatial distribution across VOIs at the millimeter scale. The goal of our structural analysis in this chapter was to determine a set of useful metrics for describing trabecular bone structure, and we determined that these metrics are correlated with the stiffness of trabecular bone using 40 healthy trabecular bone samples. Future work can include a more comprehensive statistical analysis using a significantly larger data set containing both healthy and osteoporotic bone in order to characterize how the

structural metrics vary as the overall health of bone samples decreases.

Though the distributions of structural metrics shown in Fig. 3 are generally not normal distributions, we determine the mean value of the metrics as a convenient statistic to differentiate between VOIs. We follow the convention in network science of characterizing a network by its mean degree and/or weighted degree, and the convention in histomorphometry of using the mean trabecular thickness, spacing, and length. Future work can involve a more extensive statistical analysis on a larger data set to identify other markers for characterizing trabecular architecture.

Using principal component analysis, we find no subset of properties that captures the majority of the variation in the structural metrics, indicating that all metrics provide unique information about the structure of the trabecular networks. We also determine the Pearson correlation coefficients between structural metrics and stiffness, and find that stiffness is significantly (positively or negatively) correlated with all structural metrics analyzed. The strongest positive correlation observed was between stiffness and volume fraction, corroborating previous studies which also find that volume fraction explains a large percentage of the variation of stiffness in osteoporotic bone for similarly sized VOIs (spatial dimensions on the millimeter scale) [50, 51]. We furthermore demonstrate a positive correlation between stiffness and weighted degree that is considerably stronger than the correlation between stiffness and degree (which characterizes connectivity without taking thickness into consideration) and the correlation between stiffness and trabecular thickness (which characterizes thickness without connectivity). This may indicate that stiffer networks contain links that are both thicker and more interconnected.

We use multiple linear regression to identify seven metrics that contribute the most to explaining the variance in the data in a linear regression model: degree, weighted degree, trabecular spacing, link length, Z-orientation, weighted Z-orientation, and the number of links all had significant p-values in the multiple linear regression (Table 2.3).

These metrics are determined by computing a slightly different set of measures: degree, trabecular thickness, trabecular spacing, link length, Z-orientation, and number of links. Additionally, we use multiple linear regression with the principal components of the structural metric data to determine whether or not they present a better fit to stiffness. We find that that a model consisting of the significant structural metrics fits the stiffness data better than a model consisting of the significant principal components (adjusted $r^2 = 0.882$ for the former versus adjusted $r^2 = 0.864$ for the latter).

It is surprising that the analysis did not identify volume fraction as a significant ($p < 0.05$) variable for the prediction of stiffness, considering that volume fraction exhibits the strongest linear correlation with stiffness out of all 10 structural metrics in a linear regression model (Fig. 2.10). This does not indicate that volume fraction is uninformative in the prediction of stiffness. Its lack of significance in the multiple linear regression implies that it does not improve the predictive ability of a linear model which includes the seven significant metrics previously indicated. However, volume fraction is known to be the primary predictor of stiffness in porous media [52]. Previous studies have indicated nonlinear relationships between mechanical properties, including compressive yield strength and elastic modulus, and volume fraction in trabecular bone [53]. In this chapter, we use multiple linear regression analysis to identify the smallest subset of metrics that captures the most variation in stiffness; future work will extend the current regression model to account for the possible nonlinear dependence of stiffness on volume fraction and other variables in order to improve predictive power.

From the stress distribution across the elements of the beam models, we find that only a small number of beams withstand a load comparable to the maximal stress on a network, while the majority of links bear a stress less than or equal to one-third of this maximal stress. Further development of our modeling framework will extend the beam model to the nonlinear plastic regime, and ultimately to the point of failure, to investigate

how the failure of individual links affects the distribution of stress on the network and the overall compressive strength of the network. This may prove informative in predicting the fracture susceptibility of a trabecular network and can serve as a biologically-motivated application of previous studies characterizing the failure of disordered elastic networks [54]. Furthermore, simulating the response of bone to other types of loading conditions, such as shearing, tension, or rapid impacts, can be useful in developing a comprehensive model of fracture.

Our results identifying relationships between structural metrics and mechanical properties suggest these mesoscale metrics may prove informative for bone health. Extensions of our work to comparisons between healthy and osteoporotic bone samples may inform future diagnostics. In particular, extensions of the analyses of Table 2.1 and Fig. 2.10 to diseased bone may inform the characterization of fracture resistance by identifying structural differences between healthy and diseased bone. Additionally, applying network analysis to bone at various stages of disease or aging may provide insight into how healthy bone changes over time.

In clinical applications, high-resolution *in vivo* measurements are increasingly appreciated as necessary for the evaluation of bone fragility. Innovative techniques for high-resolution data acquisition of fine tissue structure are already in development (Chapter 4) [55], as well as techniques for *in vivo* mechanical assessment such as reference point indentation [56]. The methods developed in this chapter aim to complement advances in medical diagnostic measurements by identifying biomarkers that may be useful to target using clinical procedures. Moreover, should high-resolution *in vivo* imaging of human bone throughout the body become feasible, network models can be generated from bone scans of patients and used to assess fracture risk. Our framework can hence inform the development of improved procedures for assessing bone health and detecting the onset of disease.

Chapter 3

Fracture in topology-optimized bio-inspired networks

3.1 Introduction

In pursuing a more complete understanding of how the microarchitecture of trabecular bone contributes to its emergent strength and function, we can also mine nature for insight on how to engineer bio-inspired materials that are strong and resilient. Materials found in nature must be spatially arranged to withstand repeated loading while facilitating various biological functions. In this chapter, we use multi-objective topology optimization, finite element modeling, and network science methods to generate and analyze a range of networked structures with varying emphases placed on maximizing stiffness, perimeter, and stability. We explore how differently weighting these objectives influences robustness and resistance of these structures to failure.

The bio-inspired structures we develop here are motivated by the challenge of reverse-engineering trabecular bone. Compared to the hard, dense cortical bone, trabecular bone is weaker but has roughly ten times the surface area. The pores in trabecular bone hold

bone marrow, nerves, and blood vessels, and the increased surface area facilitates bone resorption and remodeling. This tradeoff between the pore distribution and strength drives our choice of objectives in constructing structures guided by the emergent properties of vertebral trabecular bone.

Continuum topology optimization is a method that, given a set of objectives and constraints, optimizes the distribution of material within a domain [57]. We are motivated to use topology optimization to generate bone-inspired structures by the premise of Wolff's law [22]: over time, trabecular bone remodels its architecture to adapt to the loads it is regularly subjected to. That is, it will 'self-optimize' itself into a structure that is more stiff along the primary loading directions. Analogously, multi-objective topology optimization starts from an initial density distribution, applies specified loads that in our case represent uniaxial loading in vertebrae, and minimizes a weighted sum of objective functions to achieve a desired architecture. Here, the objective functions represent compliance (inverse stiffness), perimeter (the 2-D analog of surface area), and stability. Conceptually speaking, we assume that real bone is the outcome of a biological optimization procedure, but the quantities being optimized are unknown. While the topology-optimized structures are not intended to mimic bone, in isolating material properties associated with bone and varying the weights of corresponding objective functions, we examine how the relative weighting impacts overall toughness and robustness to failure.

The topology-optimized structures are disordered planar networks. Following the modeling approach detailed in Chapter 2, we extract from them graph models which allow us to extract topological metrics that quantify the architecture of the network. We further analyze the mechanical response of the topology-optimized networks by converting the networks to beam-element models. We simulate compressive loading in similar fashion as in Chapter 2, with the addition of a failure criterion to simulate fracture. In

combining these computational methods, we relate the mechanics of bone-like structures to their architecture and identify how topology informs fracture. Our results inform the development and design of bio-inspired networked structures that are robust and strong.

3.2 Multi-objective topology optimization

The topology optimization process begins by assuming an initial two-dimensional density distribution on a discretized uniform grid of elements, then iteratively 1) performs a finite element analysis step that simulates mechanical deformation, 2) carries out a gradient-based optimization step that updates the density distribution, and 3) evaluates the objective until convergence [58]. Three objectives were used: compliance (inverse stiffness) minimization, perimeter maximization, and stability maximization. The objective functions are combined as a weighted sum to form a single objective function that is evaluated in the iterative optimization procedure. Adjusting the weights of each objective function can result in highly variable topologies.

Each element has a density that can take on any value between 0 (void) and 1 (solid), but intermediate values are penalized using the solid isotropic material with penalization model (SIMP) [57] to ensure that the result contains binary density values. We include an area constraint in the optimization problem so that the total area of each generated structure is effectively constant. While the topology optimization method developed here is limited to 2-dimensional structures, it can be generalized to three dimensions, albeit with a higher computational cost.

The most basic topology optimization problem is that of minimizing compliance (weights of perimeter and stability functions are set to zero) with an area constraint. The topology optimization problem for minimization of compliance C, with a constraint

on the area fraction, is conventionally defined as

$$\min_{\rho} C = \mathbf{u}^T \mathbf{K} \mathbf{u}, \tag{3.1}$$
$$\text{s.t. } \frac{1}{A_\Omega} \sum_{e=1}^{N} \rho_e A_e \leq A,$$

where $\mathbf{K}$ is the material stiffness matrix, $\mathbf{u}$ is the vector of displacements, A_Ω is the total area of the domain, ρ_e is the density of element e, A_e is the area of each element, and A is a specified total area fraction. Here, $\mathbf{u}$ is related to the vector of applied loads, $\mathbf{f}$, through the relation

$$\mathbf{K}\mathbf{u} = \mathbf{f}. \tag{3.2}$$

Compliance is minimized, or equivalently, stiffness maximized, to minimize the displacement undergone by the structure in response to loading. Minimizing compliance alone produces a structure primarily consisting of thick rods aligned with the principal direction of loading (Fig. 3.1A). Hence, an anisotropic architecture can give rise to increased stiffness when the elements (trabeculae) are preferentially aligned with the loading direction.

However, trabecular bone does not consist of thick parallel rods. The surface of trabecular bone is necessary for its remodeling cycle, which requires contact with surrounding bone marrow for new osteoclasts to form [59]. Bone is resorbed by osteoclasts, with new bone deposited on the surface by osteoblasts. Trabecular bone also has a much higher surface area compared to cortical bone and consequently a large number of pores that hold marrow, nerves, and blood vessels.

Reverse-engineering trabecular bone to produce a structure of similar flexibility and lightness will require taking perimeter into account as in the objective function. Here we define P, the perimeter (2-D) or surface area (3-D) of the structure, in a dimension-

agnostic form as

$$\max_{\rho} \; P = \int \Delta\rho \; \mathrm{d}\Omega, \tag{3.3}$$

where ρ is the material density or volume at any point in the structure. Numerically, this translates to a sum of density changes across all element boundaries. Setting the perimeter function weight to a non-zero value and optimizing for both compliance and perimeter, while keeping the same volume, results in a structure with a greater number of thinner struts, rather than fewer, thicker ones. Most of these thin struts are aligned in the principal loading direction, while a few are transverse.

Previous studies applying topology optimization to explore trabecular bone structure have considered only compliance as an objective function and included a perimeter constraint [60, 61]. However, depending on the weights used, including only compliance (and perimeter) objective functions can result in an unstable model, such as one that consists of long, thin vertical rods. The instability of this model is represented by its critical buckling load, $P_{crit} = \max_{i=1,\ldots,N_{dof}} P_i$. The objective in this case is to maximize the critical buckling load defined by the generalized eigenvalue equation

$$\left[\mathbf{G}(\mathbf{u}) - \frac{1}{P_i}\mathbf{K}\right] \mathbf{\Phi_i} = 0, \quad i = 1, \ldots, N_{dof}, \tag{3.4}$$

where $\mathbf{G}(\mathbf{u})$ is the geometric stiffness matrix and $\mathbf{\Phi_i}$ is the eigenvector associated with the ith buckling load. To avoid degeneracy of the eigenvalues $1/P_i$, which can result in poor or incorrect convergence of the optimizer, we apply a bound formulation [57] such

that the stability optimization problem is written as

$$\begin{aligned} &\min_{\rho} \ \beta, \\ &\text{s.t. } \alpha^i \left(\frac{1}{P_i}\right) \leq \beta, \ i = 1, \ldots, N_{dof}, \\ &\left[\mathbf{G}(\mathbf{u}) - \frac{1}{P_i}\mathbf{K}\right] \mathbf{\Phi_i} = 0, \ i = 1, \ldots, N_{dof}, \end{aligned} \tag{3.5}$$

where α is a number slightly less than 1, e.g. 0.95, which ensures that each eigenvalue is slightly larger than the next. Note that this bound formulation will only actively impact eigenvalues near one end of the spectrum and eigenvalues in the interior or near the other end of the spectrum will inherently satisfy the constraint. As a result, we can safely truncate the series from N_{dof} terms to a much smaller number such as $n = 10$. Optimizing for stability as well as compliance and perimeter further increases the number of struts as well as those oriented at a nonzero angle to the primary loading (vertical) direction.

The multiple objectives are combined as a weighted sum, where the weights can be varied to change the relative importance of each objective:

$$\begin{aligned} &\min_{\rho} \ w_1 C_0 - w_2 P_0 + w_3 \beta_0, \\ &\text{s.t. } \alpha^i \left(\frac{1}{P_i}\right) \leq \beta, \ i = 1, \ldots, N_{dof}, \\ &\left[\mathbf{G}(\mathbf{u}) - \frac{1}{P_i}\mathbf{K}\right] \mathbf{\Phi_i} = 0, \ i = 1, \ldots, N_{dof}, \\ &\frac{1}{A_\Omega} \sum_{e=1}^{N} \rho_e A_e, \\ &\sum_{i=1}^{3} w_i = 1, \end{aligned} \tag{3.6}$$

where w_i are the respective weights on each of the objective functions C_0, P_0, and β_0,

which refer to normalized compliance, perimeter, and stability, respectively (Eqs. 3.1, 3.3, and 3.6). Here we normalize by independently optimizing for each of the objectives separately and then evaluating each objective function on each optimized structure. The functions are then normalized relative to the maximum and minimum values across each of the structures.

Note that the purpose of normalization is to make the magnitude of each function more consistent. As a result, the actual values of the function weights for one system are somewhat arbitrary in that they depend on the normalization procedure used. As such, the weights are only truly meaningful when compared relative to each other and/or across different optimization problems. It is possible, once the optimization is completed, to compute the actual contribution of each objective to the aggregate cost function. Examples are given in Table C.1 in Appendix C.

We generate topology-optimized structures for a total of seven different sets of objective weights. One example structure for each parameter set is shown in Fig. 3.1; all remaining structures are included in Appendix C.2. Each set contains twelve different structures. Each structure is generated from the same initial density distribution, with a small perturbation added to ensure that each optimization with the same weights will converge to a different structure. We label each set of structures with the letters C, P, and/or S, representing compliance, perimeter, and stability objectives, respectively, followed by the corresponding weight (times 100) of the objective function used to generate the structures.

Fig. 3.1A is an example structure from the set labeled C99999P00001, which is representative of optimizing all but entirely for compliance. The weight of the compliance function is 0.99999, rather than 1 even. If the compliance weight were 1, for some initial conditions, it is possible that the result would be a contiguous piece of material with no porosity. Hence, we assign a very small weight of 0.00001 to the perimeter objec-

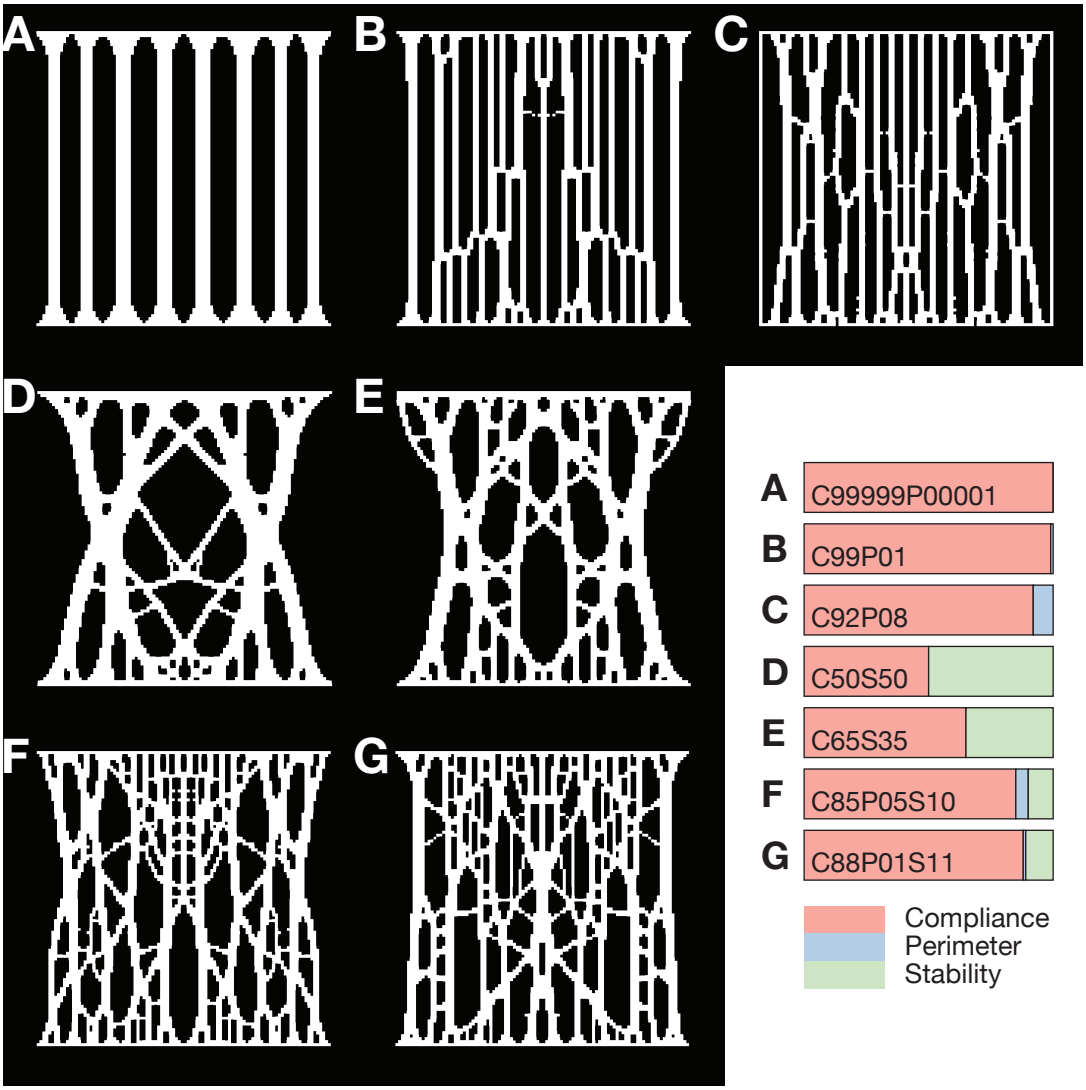

Figure 3.1: Example 2-D topology-optimized structures generated by varying objective weights. The horizontal bar plot in the lower right shows the relative weights assigned to the compliance, perimeter, and stability objectives for each image. Weights sum to one. Panels A-G: C99999P00001, C99P01, C92P08, C50S50, C65S35, C85P05S10, and C88P01S11, respectively. A total of 12 structures were generated for each of the seven parameter sets shown here; all structures for each parameter set are shown in the Supplemental Material.

tive; combined with the different initial conditions, this promotes variation in topology. Stability is not considered in this case.

Figs. 3.1B-C, labeled C99P01 and C92P08, respectively, are generated by including weights for both compliance and perimeter, resulting in an increased number of thinner

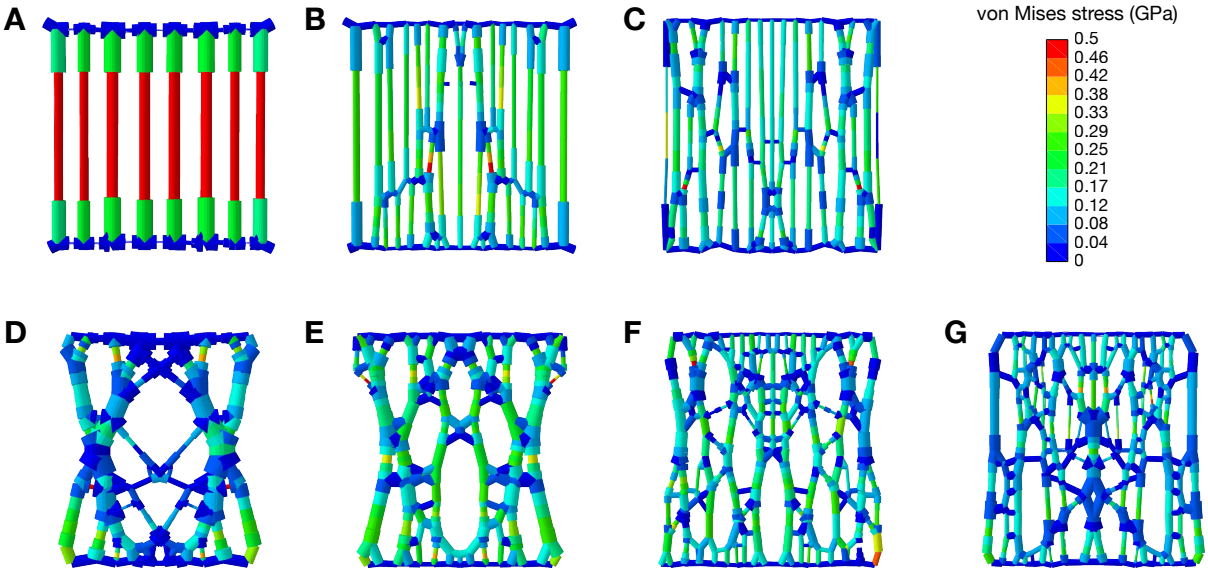

Figure 3.2: Example beam element models. Color of beams represents spatial distribution of von Mises stress in example structures for each parameter set. Each model is shown at the timestep immediately preceding the first element failure in each respective simulation. A: C99999P00001; B: C99P01; C: C92P08; D: C50S50; E: C65S35; F: C85P05S10; G: C88P01S11.

struts and consequently a greater number of pores.

Figs. 3.1D-E, labeled C50S50 and C65S35, respectively, are generated by including weights for compliance and stability, but omitting the perimeter objective. The resulting structures consist of much thicker struts that are largely oriented at an angle to the vertical. The structures are also noticeably concave at each side.

Figs. 3.1F-G, labeled C85P05S10 and C88P01S11, respectively, are generated from combining all three objectives. These structures contain more struts and small pores than the other sets, with a few longer vertical columns joined by a number of shorter angled elements.

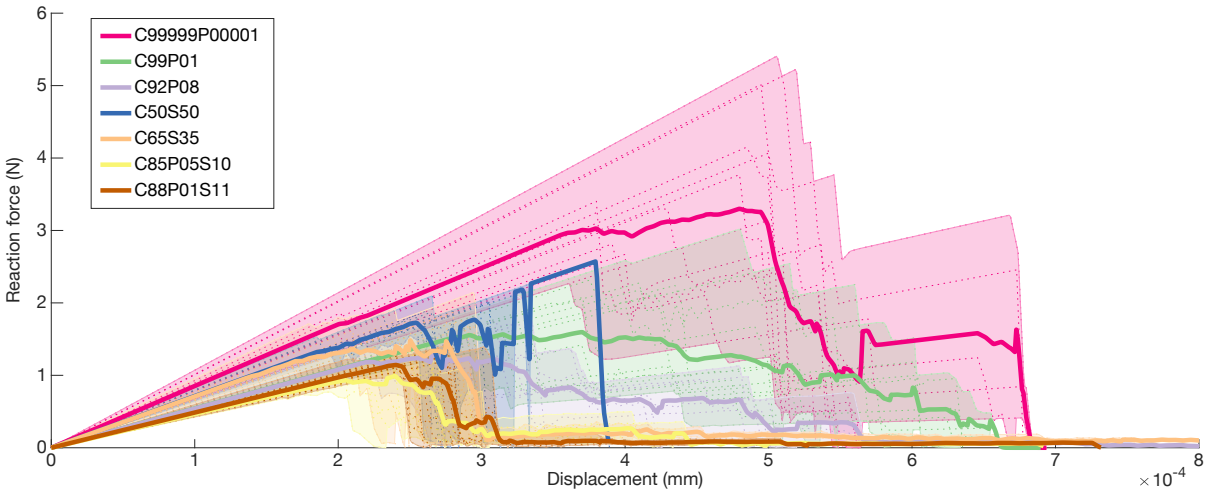

Figure 3.3: Force-displacement response. The force-displacement curve for each structure is indicated by a thin dashed line; the average curve for each parameter set is shown as a thick solid line. Shaded areas represent the regions spanned by the highest and lowest reaction force for each parameter set.

3.3 Network modeling and mechanical simulation

3.3.1 Skeletonization

From topology-optimized images, we generate graph models, following the procedure described in Section 2.2.2, that allow us to utilize existing graph theoretical methods to efficiently analyze the topology of networked structures. Converting a topology-optimized structure to a graph begins with skeletonization, or progressively thinning the image until its one-pixel-wide medial axis is found, followed by conversion to a graph by setting nodes at branch points where 3 or more struts meet, with edges corresponding to struts themselves. The edges are weighted according to the respective average thicknesses of corresponding struts. Skeletonization and graph conversion are accomplished using the Skeleton3D and Skel2Graph toolboxes for MATLAB [45]. Strut thicknesses are computed using the BoneJ plug-in [46] for ImageJ (National Institutes of Health, Bethesda, MD).

3.3.2 Beam element models

To simulate mechanical loading and deformation, we translate these graphs into streamlined finite element models. Rather than meshing the trabecular model, we generate beam-element models from the graphs, where each link is represented by a Timoshenko beam with a uniform thickness corresponding to its weight (Fig. 3.2). Nodes in the beam-element model correspond directly to nodes in the network.

Mechanical loading is simulated with Abaqus FEA. The beam-element model is compressed from the top and bottom, representing loading along the superior-inferior direction, the primary loading axis in vertebrae. The von Mises stress at each link is computed at each time step, along with the force and displacement of each node. von Mises stress is a stress invariant often used as a yielding criterion in ductile materials and in two dimensions is given by

$$\sigma_{\text{von Mises}} = \sqrt{\sigma_{11}^2 - \sigma_{11}\sigma_{22} + \sigma_{22}^2 + 3\sigma_{12}^2}$$

where σ_{ij} is the ij-th element of the Cauchy stress tensor.

We solve the models in the linear-elastic regime, where the stress is linear as a function of strain. We also model failure by setting von Mises stress as a failure criterion; when the stress in a beam reaches the critical stress value, the beam is said to have failed and is removed from the simulation. We arbitrarily set the failure criterion to be a von Mises stress of 0.5 MPa; as the response is linear, this value can be scaled up or down with no qualitative change in the overall behavior.

We note that the skeletonization and network conversion process is limited by its inability to fully capture non-uniform trabecular thicknesses or increased bulk at branch points (nodes). This tradeoff, however, greatly simplifies modeling and provides a streamlined approach to relating topology with mechanics. To improve the resolution of tra-

becular thickness in beams with nonuniform widths, we divide longer beams into five segments, such that each segment can have a different thickness.

3.3.3 Bulk force-displacement response

Force-displacement curves for the seven beam-element models generated from the topology-optimized structures (Fig. 3.1) are compared in Fig. 3.3. We model the structures in the linear-elastic regime with a von Mises stress failure criterion. The force-displacement curves are hence linear until the initialization of beam failure, whereupon they exhibit large decreases until reaching zero, at which point the structure is said to have failed completely. The force-displacement response after this point exhibits fluctuations that are artifacts of wave propagation in the simulation and are not considered in the analysis of the results. The curves in Fig. 3.3 are truncated where the reaction force reaches zero, and the full force-displacement curves for each model are included for completeness in Appendix C.3.

On average, stiffness (the slope of the force-displacement curve in the initial linear regime) is greatest for C99999P00001, the parameter set for which compliance minimization was most highly weighted. However, C50S50 and C65S35 demonstrate slightly higher average stiffness than C99P01 and C92P08, which have greater compliance minimization weights. The models with lowest stiffness are C85P05S10 and C88P01S11.

We use two additional metrics to quantify mechanical response: the peak reaction force typically attained at the onset of element failure, and the maximum displacement at total system failure (when the reaction force reaches 0). The peak force represents the strength of the model, while the maximum displacement serves as a proxy for the ductility of the structure as it undergoes fracture. A large maximum displacement could indicate that stresses redistribute such that the entire structure does not fail imme-

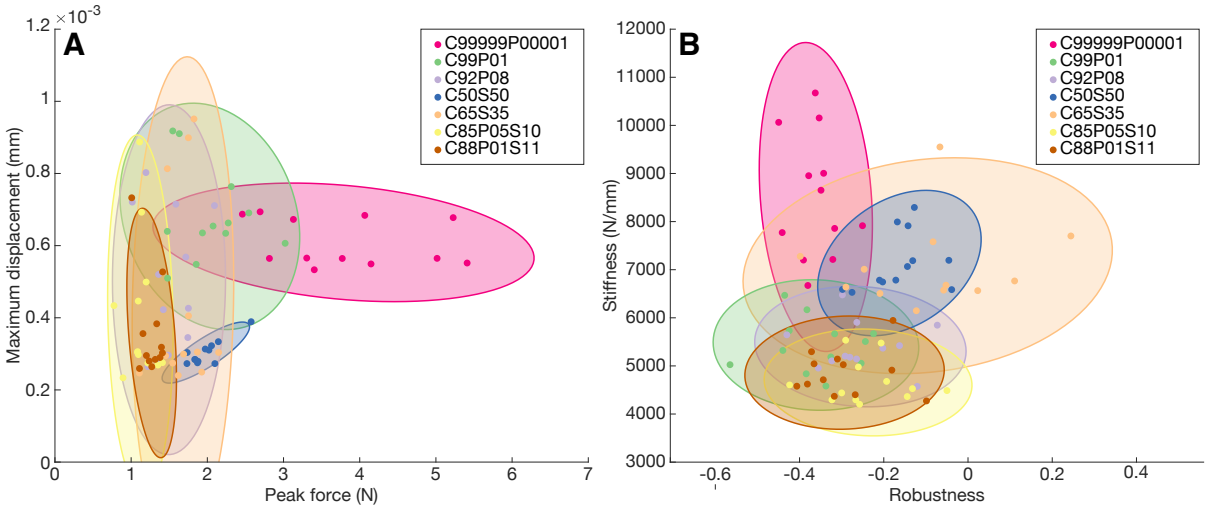

Figure 3.4: Ashby plots comparing properties of different optimization parameter sets. Panel A compares the maximum displacement before complete failure with the peak reaction force attained. Panel B compares stiffness, the slope of the force-displacement curve in the linear regime prior to failure, with robustness, measured as the relative change between the peak forces of the original and perturbed models. Shaded ellipses represent 2σ confidence intervals.

diately when the first failure occurs. The distributions of peak force and maximum displacement are compared in an Ashby plot in Fig. 3.4A. The highest peak forces are given by C99999P00001, followed by C99P01, while the peak force for the other parameter sets are comparable. The maximum displacement varies greatly for some parameter sets, in particular C92P08, C65S35, C85P05S10, and C88P01S11, while the variation in displacement is considerably smaller for C99999P00001 and C50S50.

We note that while C99999P00001 demonstrates the highest peak forces, it also has the largest variation in peak force. Hence, slight variations in structure across models, despite being generated under the same optimization criteria, can result in significantly different mechanical response. To probe robustness, we perturb each structure slightly and subject them to the same loading conditions as the original models. For each model, each node is shifted in both x- and y- coordinates by a small random distance of order 1% of the length of the structure.

For the purposes of this work, we define robustness as the relative change in peak force between the original and perturbed models: $(F_{\text{peak, original}} - F_{\text{peak, perturbed}})/F_{\text{peak, original}}$. Robustness is plotted against the stiffness of the original model in Fig. 3.4. In some cases, the perturbed model can exhibit a greater peak force than the original model, indicated by a positive robustness score. We observe that C99999P00001, which demonstrated the greatest variation in peak force among original models, exhibits relatively low robustness, with large spread in stiffness values. C65S35 exhibits the greatest variation in robustness, with several instances in which the perturbed model was stronger than the original model. C50S50 shows slightly lower robustness than C65S35; C50S50 and C65S35 exhibit roughly similar stiffness values and are the second stiffest models after C99999P00001. C99P01, C92P08, C85P05S10, and C88P01S11 demonstrate similar stiffness and robustness.

We note that the C50S50 structures lie on an approximately 45-degree line in the Ashby plot shown in Fig. 3.4. This suggests that these structures achieve a delicate balance between strength and ductility in which both mechanical markers increase hand in hand. This property is similar to what has been reported for some biological materials with superior mechanical properties such as mollusk shell, spider silk, and bone.

Our results suggest that while assigning almost all weight to compliance minimization can produce structures that are on average stiffer and tougher, these structures can be prone to small perturbations in geometry or objective weights. Moreover, optimizing for compliance and perimeter without accounting for stability can result in structures that are less robust and less stiff than those generated by assigning considerable weight to stability maximization. We observe that some structures in the C50S50 and C35S65 families exhibit positive robustness where geometric imperfections may lead to an increase in their strength and stiffness. This suggests that assigning significant weight to stability may enhance mechanical response under uncertain conditions. However, structures with small weights on both perimeter and stability objectives remain weaker and less robust

Set	$\zeta_{0.001}$	$\sigma_{0.9}$
C99999P00001	0.612	0.378
C99P01	0.421	0.397
C92P08	0.236	0.475
C50S50	0.199	0.391
C65S35	0.260	0.270
C85P05S10	0.187	0.241
C88P01S11	0.162	0.293

Table 3.1: Average $\zeta_{0.001}$ and $\sigma_{0.9}$ values for each set. $\zeta_{0.001}$ gives the fraction of beams with normalized stress less than or equal to 0.001, and $\sigma_{0.9}$ gives the normalized stress value wherein 90% of beams bear stress less than equal to this value. Stress is normalized to the largest stress value in a single beam in each individual structure.

than those for which perimeter is not considered.

3.3.4 Stress distribution

The fragility of these structures may be linked to the spatial distribution of stress: whether the stress is distributed relatively evenly or concentrated in a few beams. The distribution of (von Mises) stress across beams can vary greatly between parameter sets, as visualized in Fig. 3.2. Fig. 3.5 illustrates the distribution of stress, normalized to the highest stress value in one beam in each model, averaged over all models in a set (histogram). In the models without stability objectives (top row), a large area fraction exhibits no stress, demonstrated by a considerable peak at 0. The distribution for C99999P00001, however, shows that in some models, a small fraction of links bears almost all of the stress. In contrast, the models with stability objectives (bottom row) demonstrate a peak at 0 with relatively heavy tails.

Fig. 3.5 also shows the cumulative fraction of beams that bear normalized stress values between 0 and 1 (colored shaded regions). For C99999P00001, and to a lesser extent, C99P01, a notable fraction of beams have normalized stress close to 0. Their cumulative distributions rise sharply compared to those with stability objectives before flattening

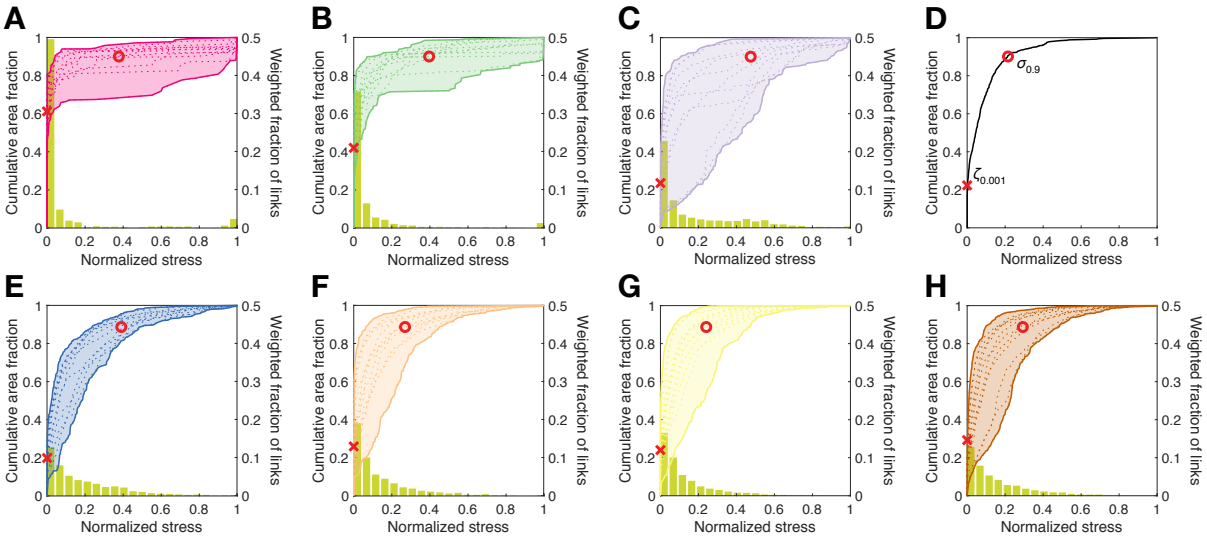

Figure 3.5: Stress distributions. A: C99999P00001; B: C99P01; C: C92P08; D: example cumulative stress distribution; E: C50S50; F: C65S35; G: C85P05S10; H: C88P01S11. Histograms represent the average distribution of normalized stress for each parameter set, weighted by the thickness of each link. The shaded regions illustrate the variation in the cumulative distribution of normalized stress, expressed in terms of the fraction of area occupied by the links (normalized by the area of the entire model). Dotted lines within the shaded regions correspond to the distributions of each individual model. Red crosses represent average $\zeta_{0.001}$ and $\sigma_{0.9}$ for each parameter set, as illustrated by the example in the panel D.

out. To quantify the stress distribution, we compute two metrics $\zeta'_{0.001}$ and $\sigma'_{0.9}$. $\zeta'_{0.001}$ is the fraction of total area with normalized stress less than or equal to 0.001, and $\sigma'_{0.9}$ is the normalized stress value such that 90% of the total area bears stress less than or equal to this value; these metrics were previously defined in the context of trabecular bone in . Average values for $\zeta_{0.001}$ and $\sigma_{0.9}$ are tabulated in Table 3.1. $\zeta_{0.001}$ is highest for C99999P00001; approximately 61% of the total area — corresponding to 67% of beams — bear almost no stress, followed by C99P01 at 42% (52% of beams). For the remaining models, which all include stability weights except for C92P08, $\zeta_{0.001}$ is lower, representing between 16% and 26% of area that is unstressed, indicating that stress is distributed more evenly for these models.

For $\sigma_{0.9}$, the highest values are found for the three models with the highest compliance weights. These models have relatively high $\zeta_{0.001}$ values as well, thus containing a larger percentage of low-stress area with the stress more evenly distributed on the remaining elements. $\sigma_{0.9}$ is moreover relatively high for C50S50, which also has a low $\zeta_{0.001}$ value, indicating that the stress distribution is less skewed. Overall, $\sigma_{0.9}$ ranges between 0.24 and 0.47 for all models, implying that a small percentage of beams bear large stresses.

The models with stability objectives are most similar in visual resemblance to trabecular bone, and the shape of their stress distributions is also the most similar to that of bone (Figure 2.8). For the models with stability objectives, however, $\zeta_{0.001}$ remains much lower than for bone, which is on average approximately 0.43 (Section 2.4.2), while this value is surpassed for C99999P00001 and C99P01. For bone, approximately 6.7% of the total volume fraction bears less than 90% of the normalized stress, indicating that the stress distributions are considerably less skewed for the topology-optimized models than for bone — note, however, that the topology-optimized structures generated here are two-dimensional, while the bone volumes analyzed previously are three-dimensional.

3.3.5 Community detection

We use community detection to investigate whether the topology of the network encodes information about likely points of failure. We observe that locations of failure — i.e., the most stressed beams in the finite element models — do not generally correspond with the thinnest elements, and there is no preferred orientation associated with the failed beams. We hypothesize that elements corresponding to links that connect two different communities — "boundary links" — are more likely to fail than elements within a community.

Community detection is a method of determining clusters (communities) that contain dense within-cluster connections, with sparse connections to the rest of the network [24]. The development of community detection algorithms and their application as a beginning phase of network structure or function diagnostics is a focus of network science [62]. Community detection has been used to characterize social interactions, brain function, and much more, but most pertinently to characterize force chains in granular materials [63, 64]. Granular packings have been described by assigning nodes to individual particles and edges to contact forces between particles [28]. Community detection can extract information about force chains, networks that typically resemble interconnected filaments primarily aligned with the principal axes of loading.

Here, we perform community detection to identify whether failure locations reside in any particular locations within the network topology. Community detection typically involves maximizing a modularity function Q that identifies community structure relative to a null model P [24, 28]:

$$Q = \sum_{ij} [W_{ij} - \gamma P_{ij}] \delta(g_i, g_j), \tag{3.7}$$

where W_{ij} is the weight of the edge between nodes i and j, γ is a resolution parameter

that controls community size, P_{ij} specifies the expected weight of the edge between nodes i and j under the null model, g_i is the community assignment of node i, and $\delta(g_i, g_j)$ is the Kronecker delta.

The null model is commonly chosen to be a random rewiring of nodes with the degree distribution kept constant (Newman-Girvan null model):

$$P_{ij} = \frac{s_i s_j}{2m}, \tag{3.8}$$

where s_i is the weighted degree of node i and m is the sum of all edge weights in the network (i.e., $m = \frac{1}{2}\sum_{ij} W_{ij}$). This null model assumes that connections between any pair of nodes is possible. However, because the networks are spatially embedded, and long-range connections that span large spatial distances are impossible, we choose a *geographical null model*, initially developed for use in the study of brain networks and subsequently adapted for granular networks [63]:

$$P_{ij} = \rho B_{ij}, \tag{3.9}$$

where ρ is the mean edge weight of the network and $\mathbf{B}$ is the binary adjacency matrix of the network (i.e., the adjacency matrix where all nonzero edge weights have been set to 1).

The geographical null model produces communities that are anisotropically aligned with the vertical direction and thus reminiscent of force chains. The resolution parameter γ modulates the size and number of communities. We set γ to 1.6. Examples of community structure are shown in Fig. 3.6.

We observe that failures tend to occur at the boundaries between communities, i.e., in links that connect two different communities. We quantify statistical significance with

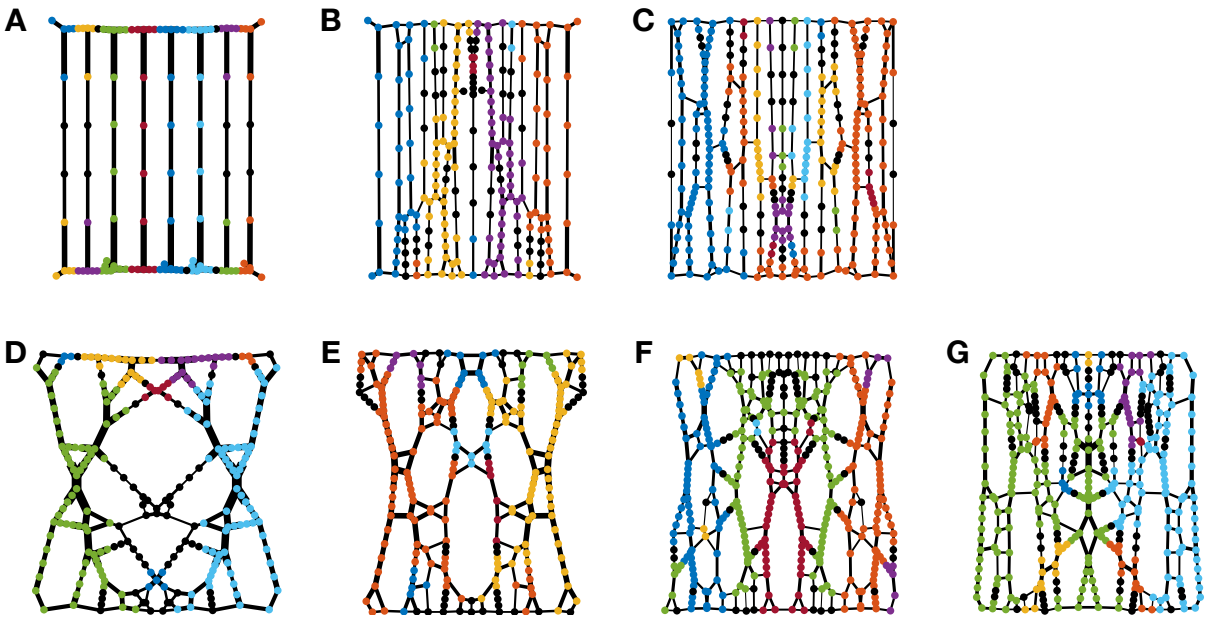

Figure 3.6: Example of community structure for each parameter set. A: C99999P00001, B: C99P01, C: C92P08, D: C50S50, E: C65S35, F: C85P05S10, G: C88P01S11. Nodes are colored to distinguish between communities. Black nodes represent communities of one node.

the Bayes factor, which represents the inverse of the ratio of probability of the data given the null hypothesis — that the probability q of a failure occurring at a boundary link is equal to the fraction of boundary links in the network l_{bd}/L — to the probability of the data given the alternative hypothesis — that the probability q of failure occurring at a boundary link is unknown and where we assume a uniform prior on $[0, 1]$. The Bayes factor is given by

$$BF = \frac{P(F_{bd} = f | F_{tot}, q \text{ unknown})}{P(F_{bd} = f | F_{tot}, q = l_{bd}/L)}, \tag{3.10}$$

where F_{bd} is the number of failures at boundaries, F_{tot} is the total number of failures, l_{bd} is the total number of boundary links, and L is the total number of links. Furthermore,

$$P(F_{bd} = f | F_{tot}, q = l_{bd}/L) \tag{3.11}$$

$$= \binom{F_{tot}}{f} (l_{bd}/L)^f (1 - l_{bd}/L)^{F_{tot}-f}, \tag{3.12}$$

and

$$P(F_{bd} = f | F_{tot}, q \text{ unknown}) \tag{3.13}$$

$$= \binom{F_{tot}}{f} \int_0^1 q^f (1-q)^{F_{tot}-f} dq \tag{3.14}$$

$$= \binom{F_{tot}}{f} \mathrm{B}(f+1, F_{tot}-f+1), \tag{3.15}$$

where B is the beta function. Then the Bayes factor is given by

$$BF = \frac{\mathrm{B}(f+1, F_{tot}-f+1)}{(l_{bd}/L)^f (1-l_{bd}/L)^{F_{tot}-f}}. \tag{3.16}$$

If $BF > 10^2$, or similarly $\ln BF > 5$, then the evidence strongly supports the alternative hypothesis over the null hypothesis.

We find that the fraction of failures that occur at these boundary links ranges between 0.58 and 0.73 for structures in sets C50S50, C65S35, C85P05S10, and C88P01S11 (Table 3.2). The fractions are smaller for the sets without stability objectives, and decreases as the compliance weight increases. In contrast, the fraction of links in the networks that are boundary links ranges between 0.25 and 0.32.

The average values of F_{bd}, l_{bd}/L, and $\ln BF$ are tabulated in Table 3.2, while their distributions are illustrated in Figure 3.7. The Bayes factors are lowest for C99999P00001 and C92P08. Moreover, the spread of F_{bd} values for C99999P00001 and C92P08 are the largest, with some structures having very few failures at boundaries in the case of C99999P00001. We observe that models with high compliance weights and no stability objective contain a greater number of vertical beams and are less disordered in structure, which can result in community detection being less useful at characterizing failure locations. Overall, we find that all Bayes factors support the significance of the hypothesis that probability of failure occurring at a boundary is not the same as the probability

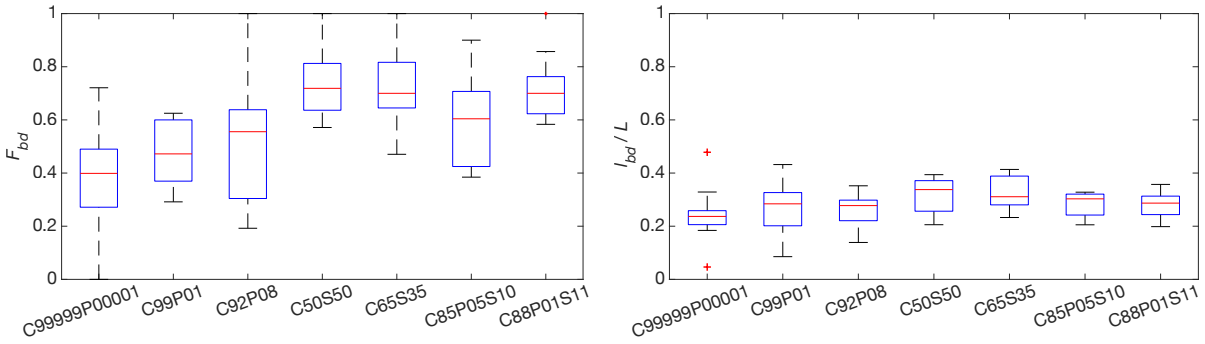

Figure 3.7: Variation in fraction of failures that occur at boundaries between communities (F_{bd}), and overall fraction of edges that join two different communities (l_{bd}/L).

Set	F_{bd}	l_{bd}/L	$\ln BF$
C99999P00001	0.359	0.255	12.6
C99P01	0.469	0.264	25.9
C92P08	0.517	0.265	19.6
C50S50	0.724	0.321	43.0
C65S35	0.733	0.324	43.6
C85P05S10	0.576	0.279	49.6
C88P01S11	0.722	0.283	96.0

Table 3.2: Fraction of failures that occur at boundaries between communities (F_{bd}), and overall fraction of edges that join two different communities (l_{bd}/L). Logarithm of Bayes factor > 5 indicates statistical significance.

that a link represents a boundary.

3.4 Discussion

We use multi-objective topology optimization to generate networked structures inspired by trabecular bone. An analysis of the stress distribution and fracture patterns in these structures reveals the contribution of compliance, perimeter, and stability objectives to strength and resilience. We observe that in structures with the greatest weight maximizing stiffness, with little to no consideration given to optimizing for stability, mechanical response is sensitive to small geometric perturbations. In comparison, structures generated with greater weight given to the stability objective are more robust.

Each topology-optimized structure analyzed in this chapter is constrained to have the same area fraction, but mechanical response can vary widely among structures that otherwise have the same objective weights. This corroborates previous findings that bone mass density is an incomplete predictor of fracture resistance in trabecular bone [1, 15, 16, 17, 18]. Moreover, this variation is most notable for structures optimized primarily for compliance. Prior studies of topology-optimized structures inspired by trabecular bone involve solely compliance minimization with perimeter constraints [60, 61]. Here, we find that when perimeter and stability weights are taken into account, the reaction force and displacement maxima shift significantly. This may suggest that compliance minimization alone overestimates the behavior of a realistic biological material. Since these materials are typically multifunctional, introducing multiple objectives beyond compliance in topology optimization will provide more flexiblity in balancing various tradeoffs without greatly compromising the mechanical response. When considered on its own as a design principle, Wolff's law, which states that bone adapts itself to resist the loads under which it is placed, and hence typically results in increased bone mass along principal loading axes, may result in structures that are less robust. In real biological tissues, Wolff's law is likely not the sole factor governing remodeling processes, and it may hence be important to use robustness as an objective for bio-inspired design.

Our mechanical simulations are linearly elastic, followed by brittle failure initiated by a stress-based criterion. An entire beam fails at once when the stress in the beam reaches a specified threshold, but in bone, the nonuniform thicknesses of trabeculae would result in beams that fail progressively. Our division of each beam into five segments serves to mitigate this discrepancy. Moreover, taking into account inelasticity and subscale energy dissipation mechanisms can improve realistic modeling of bone-like structures.

Our observation of substantial variation in the distribution of stress across different models suggests an investigation into the extent to which topology optimization can

engineer redundancy in structures. A structure with redundant or sacrificial beams may have higher toughness as the failure of some beams might not immediately result in catastrophic system failure, and stress can be redistributed through remaining beams.

It will be valuable to draw further biological inspiration from the changes in bone structure that occur due to aging, e.g. increases in anisotropy. Currently, our topology-optimization results are static and the objectives used are not chosen with regard to a material that undergoes age-related geometric changes. Additional insight into aging processes can be achieved by extending the modeling procedure to begin with our original topology-optimized structures as initial conditions, followed by an optimization process that reflects the conditions of aging bone.

It is also of interest to apply our methodology to experiments, for instance by laser cutting or 3-D printing topology-optimized structures and testing mechanical compression *ex silico*. Moreover, generating larger and denser (in terms of struts per unit area) structures can allow us to explore the behavior of cracking and how crack patterns can change with different objective weights. Driscoll et al. have studied the relationships between rigidity and crack patterns in both simulated random networks and experimental 2-D disordered honeycomb lattices [54]. Moreover, Berthier et al. have used edge betweenness centrality to predict locations of failure in experimental 2-D disordered networks [65]. Edge betweenness centrality is a measure that describes the frequency at which an edge lies on the shortest path between pairs of nodes in a network. Indeed, edge betweenness centrality as a failure marker is akin to our use of "boundary links" in characterizing failure locations as calculating edge betweenness can be used for determining community structure as per the Girvan-Newman method [33]. Edges connecting different communities have high edge betweenness centrality.

The modeling framework developed in this chapter has wide-ranging applications for the design of materials and networked structures inspired by nature. While we focus on

macroscale architecture in this work, engineering additional architecture at micro- and nanoscales can lead to improved function as bone, along with other naturally-occurring materials such as wood and nacre, exhibits structure and mechanisms of strength at a range of scales [66, 67]. Characterizing the contribution of multiscale organization to emergent strength can further inform the development of bio-inspired materials.

Chapter 4

Novel magnetic resonance technique for clinical assessment of trabecular health

4.1 Introduction

In this chapter, we discuss a newly introduced method that allows for clinically probing the health of trabecular bone (and potentially other biological tissues) in live patients. Currently, bone architecture cannot be directly imaged *in vivo* in high resolution in all parts of the skeleton. Imaging techniques that can be accomplished *in vivo* include quantitative computed tomography (QCT), high-resolution magnetic resonance imaging (HR-MRI, or micro-MRI), and high-resolution peripheral quantitative computed tomography (HR-pQCT) [68]; HR-MRI and HR-pQCT have been used to probe the morphology of trabecular bone, but neither reach the resolution of micro-CT. Meanwhile, mechanical methods for assessing bone strength, stiffness, and hardness are primarily undertaken *ex vivo*. However, *reference point indentation* has been developed as a method of mechani-

cally assessing bone *in vivo* via an instrument containing a probe that is inserted through the skin and tissue beneath to indent the underlying bone [56, 69, 70, 71], and can be applied in a rapid procedure in the clinical setting.

Here, we focus on computationally validating a magnetic resonance (MR) technology called µTexture, developed by bioProtonics, Inc. [55], for non-invasively probing the texture of various biological tissues including trabecular bone. µTexture overcomes the motion limitations of existing MRI methods to acquire high-resolution data that can inform the detection and monitoring of disease. A vast number of diseases, such as hepatitis C, nonalcoholic fatty liver disease, and pulmonary fibrosis, are linked to changes in tissue texture in the heart, liver, and other organs [72, 73, 74]. We focus, however, on the structural damage and changes in anisotropy that occur in trabecular bone with the onset and progression of osteoporosis and osteopenia.

While micro-CT is the current standard for obtaining high-resolution images of bone and other tissues, the large amount of radiation involved prevents its clinical use, limiting its application to isolated samples or small animals [1]. In contrast, µTexture is designed to be implemented clinically for diagnosis and monitoring of disease. MRI does not involve ionizing radiation, but existing MR methods cannot achieve the resolution of micro-CT. In traditional MRI, measurements are made in the spatial frequency domain; the raw data matrix is referred to as k-space, which is Fourier transformed to obtain the final image. Rather than acquiring a 2-dimensional image, µTexture finely samples one point of k-space at a time to obtain high-resolution data in the spatial frequency domain, at frequencies relevant to the texture of the targeted tissue. Hence, µTexture is not limited by patient motion as in traditional MRI, and can probe smaller length scales than existing MR methods.

Here, we simulate µTexture measurements on trabecular bone tissue to determine acquisition parameters that will provide valuable diagnostic information related to the

structure of the probed tissue. We furthermore computationally validate the diagnostic ability of µTexture in the case of osteoporosis by developing a "ratio metric" for classification of healthy and diseased bone.

As discussed in Chapter 2 and in Appendix A.1, trabecular architecture is quantified with histomorphometry, the study of the shape and form of tissue, typically from analysis of high-resolution images. Commonly-used histomorphometric parameters include trabecular thickness (Tb.Th), trabecular separation (Tb.Sp), and trabecular number (Tb.N) — Tb.Th decreases with age and disease; Tb.N decreases as well, resulting in an increased Tb.Sp [75, 76]. Histomorphometric measures can indeed serve as informative diagnostic markers for the health and strength of trabecular bone. However, Tb.Th and Tb.Sp are typically reported as average values over a region, but the thickness and spacing can be highly variable throughout a volume of bone. Measures of variability in Tb.Th and Tb.Sp, e.g., moments or other characteristic quantities of their distributions, may provide further diagnostic information. The anisotropy of the trabecular structure has also been shown to be predictive of bone mechanics [77].

Micro-CT is the imaging standard for histomorphometry, but high amounts of radiation involved places limitations on acquiring high-resolution images of *in vivo* human bone. The highest resolution obtainable for *in vivo* imaging of bone is accomplished with HR-pQCT (high-resolution peripheral quantitative computed tomography), developed for use on distal extremities in humans, which images at a resolution of approximately 80 µm. Furthermore, the best resolution of micro-MRI (high-resolution MRI) is about 30 µm for *ex vivo* samples where motion effects are not prohibitive [36]; applied *in vivo* to peripheral locations, resolution of approximately 140 µm has been achieved in imaging bone [35]. In comparison, trabecular thicknesses are roughly 100 µm on average and are lower for osteoporotic bone. Here, we use *ex vivo* 9-µm resolution micro-CT images of human bone to obtain ground-truth histomorphometric measurements, and we simulate

diseased bone profiles by virtually eroding bone elements in these images.

While µTexture is an MR technique, it is not a procedure that is applied to existing MR images. Rather, it is a technique for obtaining frequency-space data using clinical MR equipment without acquiring full 2-D or 3-D images. In this chapter, we first introduce and detail the µTexture technique for probing biological tissues by measuring the MR signal at specific spatial frequencies relevant to the tissue texture. We then conduct an *in silico* validation of µTexture by simulating µTexture measurements, using micro-CT data as ground truth, to obtain spatial frequency information associated with trabecular structure. We start by transforming high-resolution micro-CT images into spatial frequency data, and extract a subset of this data at frequencies specifically chosen to be relevant to the structure of trabecular bone. We use the simulated µTexture measurements to calculate a ratio metric, which we then use to train a classifier to distinguish between healthy bone and bone that has been artificially eroded to simulate osteopenia and osteoporosis. We apply this classifier to bone with osteoporotic characteristics to show that the ratio metric can be used to identify diseased bone, indicating that a full 2-D image is not required to yield diagnostic information derived from bone architecture.

4.2 MR technique for probing biological texture

We have developed an MR technique known as µTexture [78] which allows for fast acquisition of magnetic resonance (MR) data from *in vivo* biological tissues, while overcoming most of the motion limitations of other commonly used diagnostic MR imaging techniques [79, 80]. µTexture is able to resolve the texture of biological tissues at wavelengths down to less than 40 µm, or even smaller in conjunction with machine learning techniques, compared with the ∼80 µm resolution of HR-pQCT or ∼140 µm resolution of micro-MRI available for *in vivo* human clinical use. In contrast to typical MRI, which

acquires data from all or most of k-space and takes the Fourier transform to obtain an image, µTexture probes k-space one point (or small region) at a time, acquiring a measure of signal magnitude vs. k-value (frequency) at the desired points or regions in k-space for a selected volume of tissue. That is, µTexture focuses on obtaining frequency-domain data at specific frequencies relevant to the texture of the targeted tissue.

Patient motion severely affects traditional MRI at the resolution required to image the fine texture of biological tissues. Even when the patient holds their breath during imaging, cardiac pulsatile motion and twitching can cause blurring. Imaging at higher resolution lengthens the data acquisition time and worsens the motion-induced blurring. Furthermore, on top of the longer times required to image higher k-values (shorter wavelengths), signal strength weakens as k increases. Because µTexture trades acquisition of a full 2-D image for a high-resolution profile at a few chosen k-space values, the acquisition time required to obtain relevant frequency-domain information about the tissue is vastly reduced. µTexture acquires measurements from one k-value on the time scale of milliseconds, small enough such that blurring due to patient motion is negligible.

µTexture uses a custom pulse sequence (Fig. 4.1) to isolate a small, targeted region, which is typically a prism with one dimension designated as the "analysis" dimension and the other two the "cross-section" dimensions. Within one µTexture excitation, the prism is excited and phase-encoded for the desired k-value or values (hereinafter referred to as a k-encode), and the signal is measured. Up to $\sim$10 k-values can be measured in one repetition time (TR; the time interval between excitations), though Fig. 4.1 describes an example procedure in which one k-value is measured in each TR. These steps can be repeated several times within the same analysis volume and the magnitude of the signals can be averaged to improve the signal-to-noise ratio. The signals from several different non-overlapping prisms, in a technique called interleaved acquisition, can also be acquired in one TR. Additional wavelengths can be probed by repeating the encoding of other k-

values over subsequent TRs, thereby building up a sampling of k-space pertinent to the pathogenesis of a disease.

As measurements from one k-value are done in a single TR, they are inherently immune to motion during signal recording. The protons in the VOI are independent, without coherence or interference effects, and the proton spin direction is decoupled from the molecular orientation. The encoded spins move with the tissue regardless of translation, rotation, or distortion of the tissue; as long as the VOI stays within the receiver and the homogeneous magnetic field, the signal is not affected. Furthermore, because µTexture probes texture, rather than acquiring an image, there is no need for precise spatial coherence between subsequent excited volumes. Hence, in a series of k-encodes over several TRs, each measurement is independent. Thus, µTexture is tolerant to motion across excitations, and this motion immunity is not tied to the fast (milliseconds-long) acquisition but to the fact that data within a chosen k-value is acquired within a single TR.

While in this chapter we focus on probing trabecular bone through isolated vertebral samples that have been washed to remove soft tissue, µTexture can be used to measure multiple chemical species in a tissue that may have differing spatial compositions. Unlike typical MRI, µTexture can probe large enough regions with signal averaging to map chemical species as a function of wavelength. With volume selection and no k-encoding, µTexture can be used to measure the NMR spectrum in order to correlate chemical species with the measured textures. One potential application is in characterizing inflammation, as the water signal of healthy tissue may be relatively organized compared to inflamed tissue, in which the water may have migrated, resulting in a more disordered composition.

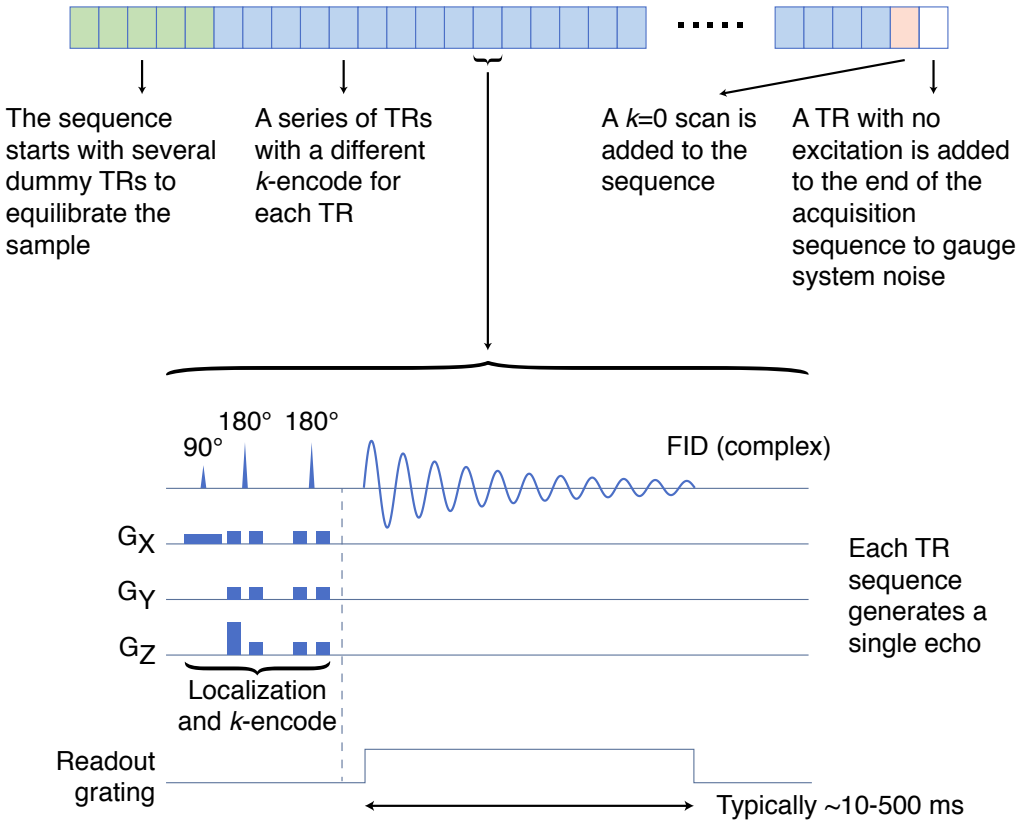

Figure 4.1: Example schematic of the µTexture measurement procedure, consisting of a repeated set of singular k-value encodings. Each TR encodes a different k-value; an example pulse sequence timing diagram for one TR is highlighted at the bottom of the figure. The free induction decay (FID) is acquired for the full T_2^* period, from which the measure for a chemical species of interest (e.g., water) at the encoded k-value is determined. The dark blue rectangles in the timing diagram represent slice-select gradients, crusher gradients, or k-encoding gradients. In this example, the z-axis is the analysis direction. Note that one of the crusher gradients is modified to k-encode the tissue.

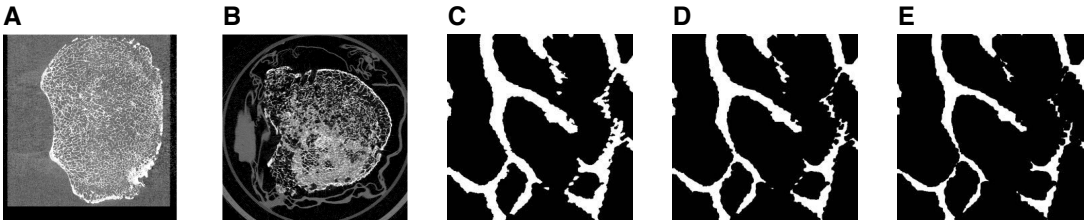

Figure 4.2: Example raw micro-CT image slices and comparison of thresholded and eroded images. A: Example 9 µm-resolution micro-CT image slice from vertebral body dataset F60L3. The image slice lies in the transverse plane and is 56.1 mm wide and 59.4 mm long. B: Example transverse slice from osteoporotic vertebral dataset AE15TH11, 52.0 mm × 52.0 mm. Image contrast has been increased in panels AB to improve visibility. CDE: 5 mm × 5 mm section of micro-CT image, eroded at various stages to simulate effect of osteoporosis. C: Baseline thresholded (healthy) section. D: The same section as in C, eroded with radius of 2 voxels (osteopenic). E: The same section as in C, eroded with radius of 4 voxels (osteoporotic).

4.3 Trabecular bone samples

To computationally validate the effectiveness of µTexture, and to identify optimal cross-section sizes and other measurement parameters for diagnostic power, we simulate µTexture data acquisition utilizing test datasets constructed from micro-CT scans of *ex vivo* vertebral bone samples. We transform the micro-CT scans into frequency space and extract the signal intensities at frequencies relevant to trabecular bone texture. We first simulate µTexture measurements on the trabecular bone within two healthy vertebral bodies, labeled AE12L2 and F60L3. An example of a micro-CT image slice from vertebral body F60L3 is shown in Fig. 4.2A. We also simulate osteoporotic bone by artificially eroding the healthy bone images; examples of eroded regions at different levels of erosion are compared with a baseline thresholded image in Fig. 4.2C–E. Furthermore, we compare our results with those from two osteoporotic vertebral bodies, labelled AE15TH10 and AE15TH11; an example image slice from AE15TH11 is shown in Fig. 4.2B.

4.3.1 Micro-CT image sets

We simulate µTexture measurements on micro-CT images of *ex vivo* human vertebral specimens obtained from a local organ bank and scanned at the Cartilage Tissue Engineering Lab at the University of California, San Diego. There are a total of two image sets generated from two specimens from two non-osteoporotic patients, and two from an osteoporotic patient. Each set comprises image slices of one vertebral body. The specimens were obtained from different vertebra; the non-osteoporotic image sets were taken from L2 and L3, and the osteoporotic image sets from TH10 and TH11. The non-osteoporotic vertebral bodies were obtained from a 75-year-old female (F60L3) and a 32-year-old male (AE12L2); neither patients had any bone-related diseases at the time of death. The two osteoporotic vertebral bodies were obtained from a 52-year-old male who died of chronic obstructive pulmonary disease and labelled AE15TH10 and AE15TH11, respectively. All images have a voxel size of 9 µm isotropic.

4.3.2 Sample preparation and imaging

The vertebral specimens are kept frozen before digestion with KOH. Specimens are thawed, and the vertebral bodies are dissected from the spinal column with a bone saw. Each vertebral body is placed in a beaker, to which 300 mL 1M KOH is added. The healthy samples are incubated at 56°C for 5 hours, with the KOH replaced after the first 1.5 hours of incubation. The healthy samples are washed with Milli-Q water several times to remove soft tissue, then incubated for another hour in KOH, for a total of 6 hours of incubation. The osteoporotic samples are incubated for a total of only 4.5 hours.

For all samples, the KOH is neutralized with the addition of glacial acetic acid at 0.052 times the volume of KOH. The samples are then washed with Milli-Q water, sonicated for 15 minutes at room temperature, washed again with Milli-Q water, then stored in 70%

ethanol at room temperature before imaging. The samples are imaged in the sagittal plane using a Skyscan 1076 (Bruker, Kontich, Belgium) micro-CT scanner at a 9 µm voxel size.

4.3.3 Histomorphometry of trabecular bone

Histomorphometric analysis of micro-CT images is accomplished using Bruker CT-analyser, or CTAn [42]. All images must be thresholded before histomorphometric analysis can be performed. The images are thresholded with 2-dimensional Otsu thresholding [43], followed by a 'despeckling' process in which black and white speckles, which are artefacts of image noise, below a specified threshold size are removed.

Analysis performed in CTAn gives average Tb.Th and Tb.Sp values for dataset AE12L2 of 0.15 mm and 0.71 mm, respectively. F60L3 has slightly higher Tb.Th and Tb.Sp of 0.19 mm and 0.81 mm, respectively. While the sample is non-osteoporotic, it is taken from a considerably older patient. The Tb.Th values fall within ranges reported in the literature for human vertebral bone, though the Tb.Sp is slightly low [18, 81].

AE15TH10 and AE15TH11, in comparison, have lower Tb.Th values, but also lower Tb.Sp values. The average Tb.Th for AE15TH10 and AE15TH11 are 0.072 and 0.073 mm, respectively, while the average Tb.Sp are 0.45 and 0.44 mm, respectively. However, these two datasets exhibit lower bone volume fractions of 10.7% and 10.0%, compared to 15.7% and 16.5% for AE12L2 and F60L3, respectively.

4.3.4 VOI selection

To focus the analysis on trabecular structure, we select volumes of interest from the interior trabecular region of the bone images, excluding portions of the images that contain the cortical shell or areas outside the bone. We subdivide this interior trabecular

region into non-overlapping contiguous rectangular VOIs that encompass as much of the region as possible. From vertebral body F60L3, we generate a total of 106 5 mm × 5 mm × 5 mm VOIs from a usable region of trabecular bone spanning roughly 25 mm × 30 mm × 36 mm, and from vertebral body AE12L2, we generate a total of 166 $(5\text{ mm})^3$ VOIs from a region spanning roughly 30 mm × 30 mm × 35 mm. The size of the VOIs was chosen such that the superior-inferior, anterior-posterior, and medial-lateral directions could be used as analysis directions, and where the VOI would be long enough in the analysis direction to contain several repeats of the trabecular pattern in order to achieve high signal-to-noise ratio. In calculating the ratio metric, we further subdivide the VOIs into 25 1 mm × 1 mm × 5 mm prisms, the signals from which are averaged together, since integrated power within our chosen frequency bands increases for narrower cross-sections (see Appendix D, Figs. D.1 and D.2). The same procedure is followed for the osteoporotic samples, yielding 13 VOIs for AE15TH10 and 15 VOIs for AE15TH11.

4.3.5 Image erosion

To simulate diseased bone, we artificially erode the micro-CT images of the healthy samples at various degrees to produce thinner trabeculae and wider spacings (Fig. 4.2C–E). The erosion process is performed by initially thresholding the images, following the Otsu and despeckling procedure described above, and then eroding the thresholded image with a kernel (or structuring element) of a chosen erosion radius. That is, a cubical (as the erosion is performed in 3-D) kernel twice the erosion radius in length is used to remove voxels from the surfaces of each bone element in the VOI. The higher the erosion radius, the more voxels are removed (the thinner the bone elements). Image erosion is not performed on images of the osteoporotic samples.

Note that at higher erosion radii, such as in Fig. 4.2E, the trabecular elements can

be eroded to the point of splitting in two, uniting gaps on either side of the elements. This can also result in isolated trabecular elements artificially created from the erosion process, though these are typically small enough to be identified and removed through the despeckling procedure. We also find that trabecular number decreases with increased erosion radius (Fig. 4.3).

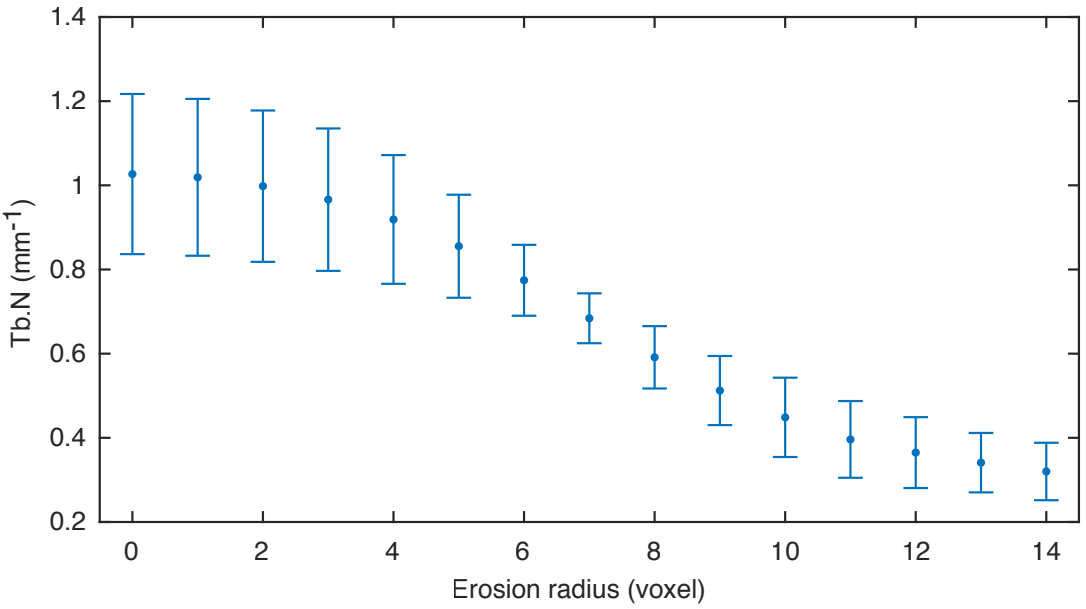

Figure 4.3: Trabecular number (Tb.N), which loosely represents the 'frequency' of the repeating trabecula-void pattern. 5 mm × 5 mm × 5 mm VOIs are thresholded, then eroded with varying erosion radii. One voxel corresponds to a (9 µm)^3 cube. Error bars indicate one standard deviation from average over 10 samples.

4.4 Results

4.4.1 µTexture measurement simulation

Simulated µTexture measurements on human vertebral trabecular bone consist of intensities at specified frequency values within chosen VOIs. First, we select rectangular prisms from several stacked micro-CT image slices and collapse each prism in two chosen

cross-section dimensions (i.e., averaging the 3-D spatial signal in the two cross-section dimensions) to obtain a 1-D spatial signal the length of the analysis dimension. We then compute the discrete Fourier transform of the 1-D signal. However, a μTexture measurement examines one spatial frequency in one TR, though measurements at different spatial frequencies (as many as ∼10 in a single excitation) are possible. Thus, to simulate a suite of μTexture measurements, we extract from the full spectrum the intensities of a selected subset of k-space values to represent a direct acquisition of signal intensities.

In order to obtain a Fourier spectrum that contains information regarding the texture of the trabecular bone, the length of the analysis dimension should be long enough to contain several repeats of the "pattern" of trabecular bone and spacing. Furthermore, the prism should be relatively narrow in the cross-section dimensions, such that averaging over these dimensions does not result in excessive washing-out of structure. In practice, however, narrowing the cross-section size, while helpful in delineating structure, will also reduce the signal-to-noise ratio.

4.4.2 Trabecular ratio metric

Architectural parameters can be readily calculated from 2-D images of trabecular bone with histomorphometry software. However, extracting structural information from frequency-domain data within a small subset of k-space is more subtle, particularly due to the variability in Tb.Th and Tb.Sp. We identify a quantity that can be extracted from a small number of k-values, as determined from simulated μTexture measurements, which can give insight into trabecular structure and serve as a diagnostic marker of bone disease.

Following Faber et al. [82, 83], we calculate a Fourier transform ratio metric to characterize trabecular bone and classify baseline (healthy) and eroded (simulated osteoporotic)

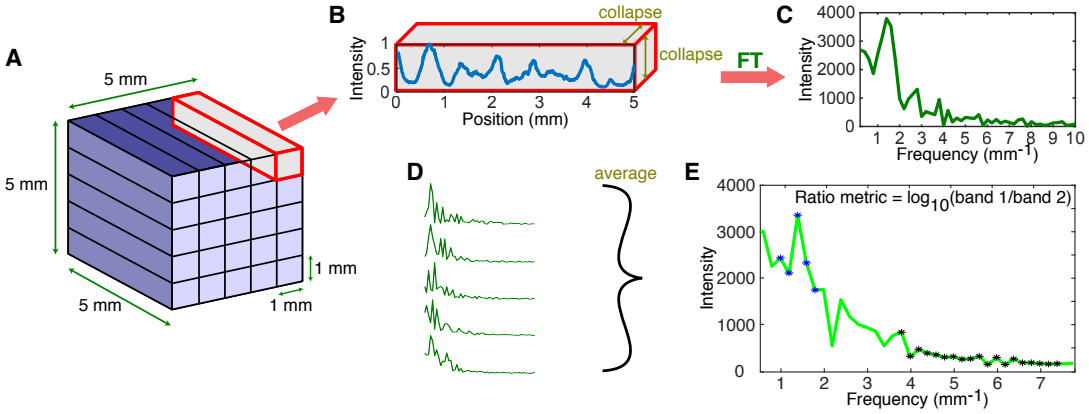

Figure 4.4: Workflow for calculating ratio metric. A: A $(5\text{ mm})^3$ VOI is evenly divided into 25 1 mm $\times$ 1 mm $\times$ 5 mm prisms. B: Each prism is collapsed along the dimensions measuring 1 mm in length. The resulting 1-D signal in the spatial domain, plotted as a function of the length of the analysis dimension (5 mm), is shown normalized to between 0 and 1. C: The Fourier transform is applied to the 1-D (non-normalized) spatial signal. The full spectrum is truncated to show the first few peaks, excluding the DC signal. D: 1-D Fourier spectra are calculated in the same manner as B and C for all the prisms in A, and averaged. E: The ratio metric is calculated from the mean spectrum by averaging the points in the low-frequency band (blue stars) and averaging the points in the high-frequency band (black stars) before taking the (log-transformed) ratio of the two values.

structures. Faber et al. began with 2-D micro-CT images of trabecular bone. For each image, the discrete 1-D Fourier transform was calculated line-by-line for each pixel row of the image. The Fourier spectra were then averaged, resulting in one 1-D Fourier spectrum for each image. The ratio metric was then determined by averaging the intensities within a chosen low-frequency band and a chosen high-frequency band, taking the ratio of the average low-frequency intensity to the average high-frequency intensity, and taking the base-10 logarithm to better approximate a normal distribution.

In contrast to the micro-CT images used in Faber et al., μTexture is not used to obtain entire 2-D position-space images. Hence, we develop an alternate method of calculating the ratio metric that more accurately simulates the μTexture measurement. First, we begin with 3-D VOIs selected from the trabecular interior of the vertebrae. We then take various small samples within a VOI (Fig. 4.4A). Each sample is the same length as

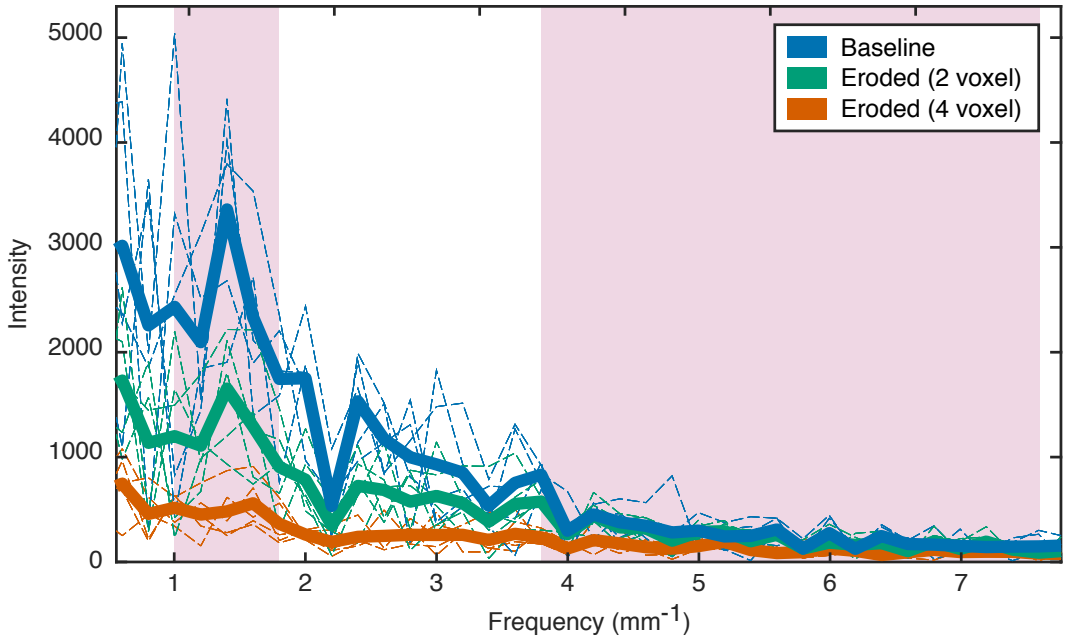

Figure 4.5: Comparing frequency-space intensities of healthy and simulated diseased bone. The Fourier spectra of a baseline thresholded VOI and the same VOI eroded to two different extents (2-voxel radius, simulating osteopenia; and 4-voxel radius, simulating osteoporosis) are shown. The baseline Fourier spectrum is the same as that shown in Fig. 4.4E. Each individual dotted line is generated by isolating a 1 mm $\times$ 1 mm $\times$ 5 mm prism generated from stacking micro-CT images, collapsing it in the cross-section (1 mm $\times$ 1 mm) dimensions, then taking the Fourier transform of the 5-mm-long 1-D spatial signal. The thick lines are generated by averaging together the dotted lines of corresponding color, such that each thick line represents a $(5\text{ mm})^3$ VOI. The pink shaded areas correspond to the low- and high-frequency bands used in calculating the ratio metric (Fig. 4.4).

the original VOI in a chosen analysis direction, but is much narrower in the two cross-section directions. We find that the integrated power within our chosen frequency bands increases as the analysis length increases and the cross-section size decreases (Figs. D.1 and D.2). We select these samples to have a cross-section size of 1 mm $\times$ 1 mm, which is on the order of the smallest resolution and machine parameters that can be acquired with µTexture, with the same analysis length of 5 mm. Since in practice, the samples cannot overlap in position space, we choose the samples to lie side-by-side spanning the entire VOI, for a total of 25 non-overlapping samples, comparable to the number of samples

that can be acquired in a few TRs with interleaved acquisition.

We then average each of these samples into a 1-D signal along the analysis direction (Fig. 4.4B). We compute the discrete Fourier transform of each of these samples (Fig. 4.4C), average the spectra (Fig. 4.4D), and calculate the ratio metric (Fig. 4.4E). As in Faber et al. [82], the ratio metric is defined as the base-10 logarithm of the ratio of average signal intensity in the low-frequency band to the average intensity in the high-frequency band.

In Faber et al. [82], the frequency bands corresponded to short and wide Tb.Sp ranges. In our case, we fix the band widths and locations to coincide roughly with Tb.Sp and Tb.Th distributions (of non-eroded structure) as determined with histomorphometric analysis in CTAn. The bands are located at $[1, 1.8]$ mm^{-1} and $[3.8, 7.4]$ mm^{-1} for low and high frequencies, respectively, corresponding to wavelengths of $[0.56, 1]$ mm for Tb.Sp and $[0.13, 0.26]$ mm for Tb.Th. However, the ratio metric is calculated from simulated raw µTexture measurements, which represent signal intensities, and as such actual values of Tb.Sp and Tb.Th are not used. Fig. 4.5 compares sample Fourier transforms for a baseline thresholded VOI and the same VOI eroded to two extents to simulate osteopenia (2-voxel erosion radius) and osteoporosis (4-voxel radius). The frequency bands used to calculate the ratio metric are highlighted.

Fig. 4.6 compares the distributions of ratio metric for baseline data and eroded data, for both the 2-voxel radius (simulated osteopenia) and 4-voxel radius (simulated osteoporosis) cases from vertebral image sets AE12L2 and F60L3. The respective baseline distributions for each dataset coincide with each other. The 2-voxel eroded distributions (Fig. 4.6ACE) overlap more strongly with the baseline distributions than the 4-voxel distributions (Fig. 4.6BDF), as is expected. The eroded distributions for F60L3 (Fig. 4.6CD) is shifted to slightly higher values of ratio metric than for AE12L2 (Fig. 4.6AB). Overall, the baseline and eroded distributions for both datasets remain mostly separate but

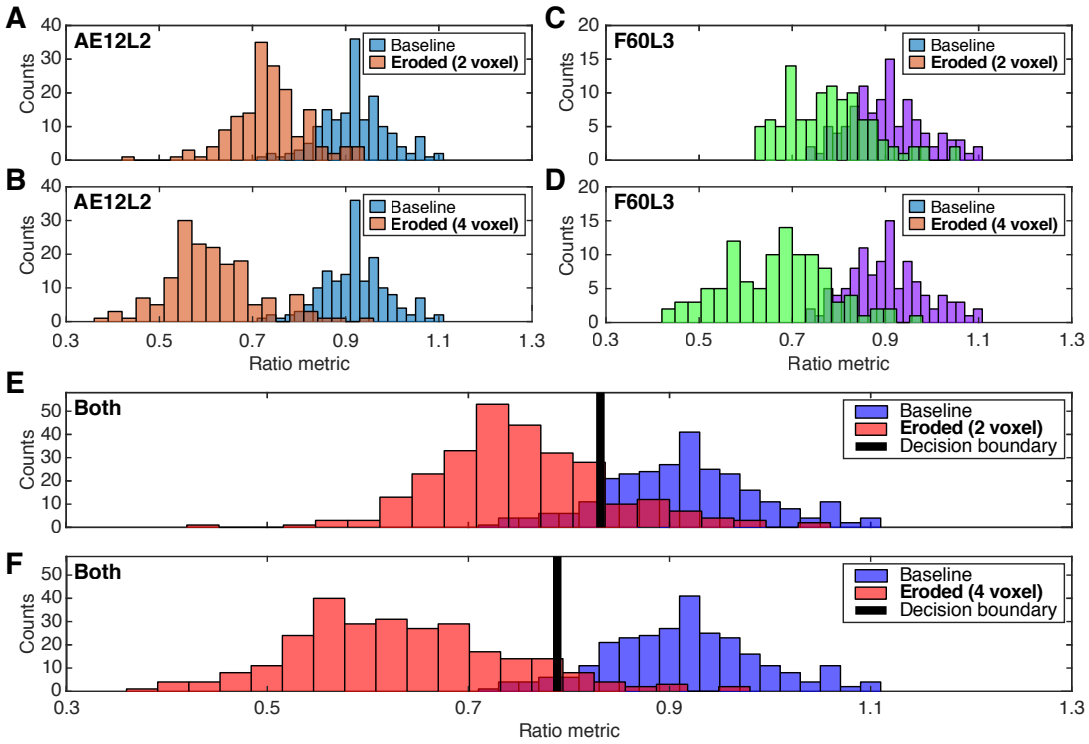

Figure 4.6: Comparing baseline and simulated diseased bone for the two healthy vertebral body samples. Each plot compares the histograms of ratio metric, a quantity determined from simulated μTexture measurements, for baseline data and simulated osteopenic or osteoporotic data, taken from a healthy vertebral dataset or datasets (AB, AE12L2; CD, F60L3; EF, AE12L2 and F60L3 combined). Each histogram (bars of the same color) corresponds to the distribution of ratio metric values calculated from either the baseline (healthy) VOIs taken from a dataset, or the same VOIs after undergoing the erosion procedure to simulate osteopenic (2-voxel radius; panels ACE) or osteoporotic (4-voxel radius; panels BDF) damage. The ratio metric values were calculated by simulating μTexture measurements on 1 mm × 1 mm × 5 mm with a 5-mm medial-lateral analysis direction. A support vector machine (SVM) classifier is trained on the baseline and eroded ratio metric values plotted in panels EF to determine the decision boundary (vertical black line) that best separates the two classes.

demonstrate some overlap between $[0.7, 1.0]$.

We verify that a bone VOI can be correctly labelled as healthy or osteopenic / osteoporotic (eroded) based on the ratio metric. That is, we use the ratio metric as the sole input feature for two-class classification. We determine the decision boundary using a support vector machine (SVM) with a linear kernel function, implemented in MATLAB. We perform 5-fold cross-validation and calculate the average sensitivity (fraction of eroded bone correctly classified) and average specificity (fraction of healthy bone correctly classified) to assess the classifier; we repeat this process a total of 50 times to minimize the effect of the partitioning of the data on the classification accuracy. Overall, we find that the sensitivity and specificity can vary significantly depending on the chosen analysis direction. For a classifier trained and tested on VOIs taken from dataset AE12L2, choosing the anterior-posterior analysis direction gave the highest sensitivity and specificity of 0.968 ± 0.003 and 0.954 ± 0.004, respectively, for the simulated osteoporotic (4-voxel eroded) case. For the simulated osteopenic (2-voxel eroded) case, the sensitivity and specificity are slightly lower due to the increased overlap in distributions and are 0.924 ± 0.008 and 0.916 ± 0.003, respectively.

For dataset F60L3 in the simulated osteoporotic case, the anterior-posterior analysis direction gave a sensitivity of 0.890 ± 0.009 and a specificity of 0.857 ± 0.005, while the medial-lateral analysis direction gave a slightly lower sensitivity of 0.888 ± 0.009 and a higher specificity of 0.907 ± 0.007. For simulated osteopenia, the anterior-posterior direction gave sensitivity and specificity of 0.762 ± 0.014 and 0.782 ± 0.012, respectively; the medial-lateral direction gave sensitivity and specificity of 0.761 ± 0.011 and 0.793 ± 0.014, respectively.

For a classifier trained and tested on VOIs from both healthy vertebral datasets combined, the medial-lateral direction gave the highest sensitivity (0.920 ± 0.003 for the 4-voxel case, 0.847 ± 0.004 for the 2-voxel case) and specificity (0.946 ± 0.003 for the

4-voxel case, 0.873 ± 0.006 for the 2-voxel case). The corresponding data and decision boundary are shown in Fig. 4.6EF. Average ratio metric values are tabulated in Table D.1 of Appendix D, and sensitivities and specificities for each analysis direction and dataset are tabulated in Tables D.2 (for the 2-voxel case) and D.3 (for the 4-voxel case). Moreover, for a diagnostic application, the decision boundary could be moved in order to prioritize minimizing false negatives, for example, at the expense of increasing the number of false positives.

A question arises as to whether a smaller region of bone can provide sufficient diagnostic information. We determine the SVM classification accuracy when varying the number of sub-samples within each $(5\text{ mm})^3$ VOI, i.e., varying the size of the cross-sectional area of the prism targeted by μTexture. We systematically increase the number of sub-samples between one (a 5 mm × 1 mm × 1 mm prism, and thus the smallest possible resolvable cross-section) and 25 (constituting the entire VOI). For classifying healthy and 4-voxel eroded bone, we found that the SVM accuracy is significantly lower when the cross-sectional area is less than 5 mm^2 (Fig. 4.7). However, for larger areas, the accuracy exhibits no significant trend, and any small variation in the accuracy could be attributed to small variation in the bone itself.

The frequency bands used for calculating the ratio metric contain 5 frequency points (for the low-frequency band) and 19 frequency points (for the high-frequency band), respectively. We investigate whether narrower bands, which would correspond to fewer μTexture measurements, result in a significant decrease in classification accuracy. We keep the same low-frequency band, but use a narrower high-frequency band of $[3.8, 5.6]$ mm^{-1}, which contains 10 points, to calculate the ratio metric, with a medial-lateral analysis direction. We train the SVM classifier on these values of the ratio metric for the thresholded and 4-voxel eroded bone sets, and we achieve, averaged over 50 runs of 5-fold cross-validation, average sensitivity of 0.890 ± 0.005 and specificity of 0.938 ± 0.005.

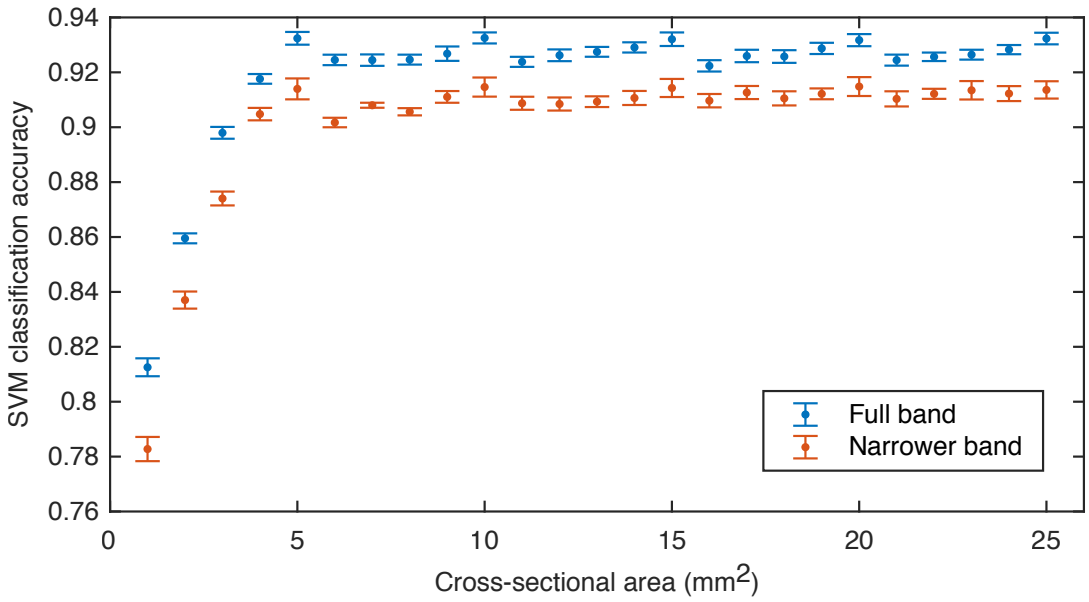

Figure 4.7: SVM classification accuracy for healthy and 4-voxel eroded bone as a function of cross-sectional area. The number of sub-VOI samples used to calculate the ratio metric is varied between 1 and 25, corresponding to cross-sectional area between 1 and 25 mm^2. The accuracy does not exhibit a significant trend when the cross-sectional area is larger than 5 mm^2. Training data is taken from both vertebral bodies AE12L2 and F60L3, with medial-lateral analysis direction. Blue points indicate ratio metric determined with original frequency bands; orange points indicate ratio metric determined with narrower high-frequency band (10 frequency points). Each point is averaged over 50 iterations of 5-fold cross-validation to minimize partitioning bias; error bars indicate one standard deviation.

Figure 4.7 illustrates the change in classification accuracy as a function of total sample cross-sectional area.

4.4.3 Osteoporotic bone

We now apply our classifier trained on artificially eroded bone to images of bone with osteoporotic characteristics. The osteoporotic vertebral bodies AE15TH10 and AE15TH11 both contain a smaller volume of trabecular bone than the healthy bodies and thus we generate much fewer VOIs from the respective CT images, obtaining 13 $(5\ mm)^3$ VOIs from AE15TH10 and 15 VOIs from AE15TH11. We determine the ratio

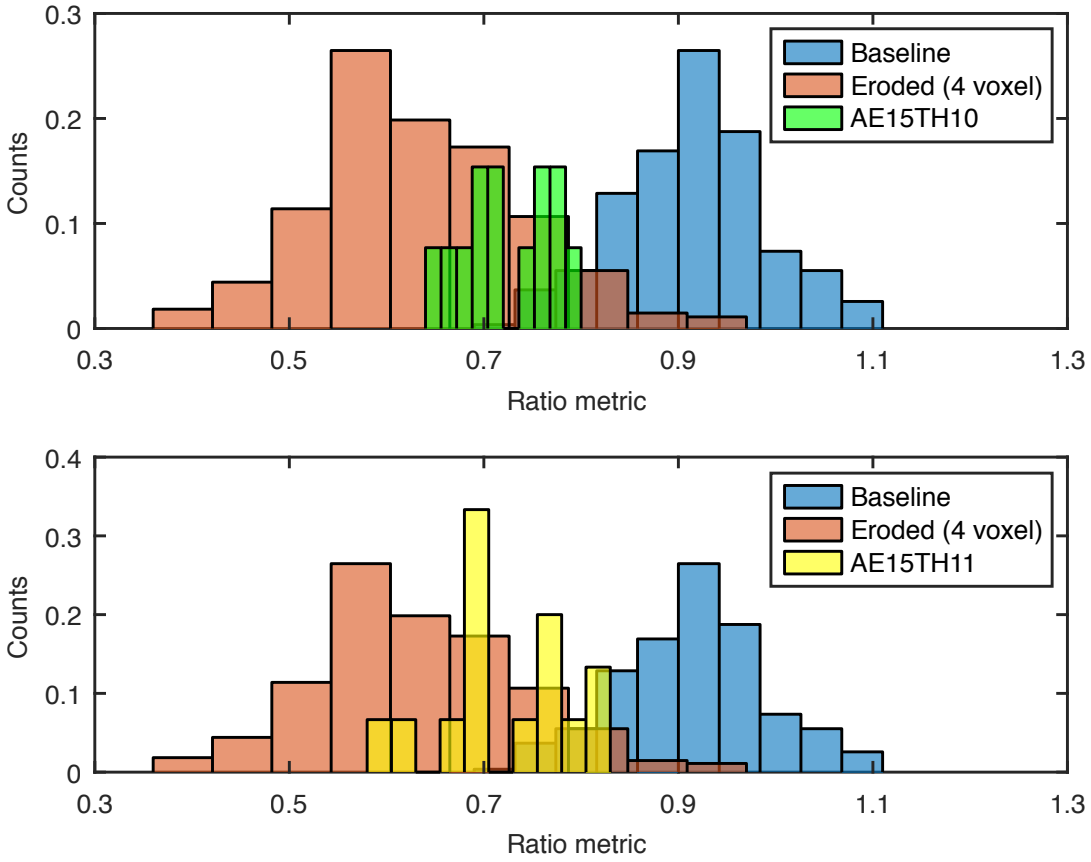

Figure 4.8: Comparing ratio metric distributions for healthy, eroded, and osteoporotic bone. Each plot compares the ratio metric histograms for baseline (blue) and eroded (orange) VOIs from datasets AE12L2 and F60L3, and the ratio metric histogram for the thresholded VOIs from each of the osteoporotic datasets (AE15TH10, green, top; AE15TH11, yellow, bottom). As in Fig. 4.6, the ratio metric was calculated using the medial-lateral analysis direction. Due to the much smaller number of osteoporotic VOIs, counts are normalized such that the total number of counts in each histogram equals 1.

metric for each of the VOIs, and use the SVM classifier trained on the baseline and artificially 4-voxel eroded data (using VOIs from both healthy vertebral bodies) to classify the osteoporotic VOIs. We find that classification accuracy is higher for the medial-lateral analysis direction than the anterior-posterior analysis direction. Fig. 4.8 compares the ratio metric distributions for AE15TH10 and AE15TH11 with the distributions from the healthy baseline and eroded data (from AE12L2 and F60L3, using the medial-lateral analysis direction) used to train the classifier. The osteoporotic ratio metric distributions coincide with the eroded ratio metric distribution, but also partially overlap with the baseline distribution. Applying the SVM classifier, VOIs from AE15TH10 are classified with a sensitivity of 0.92, while VOIs from AE15TH11 are classified as osteoporotic with a sensitivity of 0.80. Sensitivities and specificities for other analysis directions are tabulated in Table D.4 of Appendix D.

4.5 Discussion

In this chapter, we introduce an MR technique called µTexture, which can be used to rapidly acquire high-resolution information at scales ∼40 µm about the complex architecture of biological tissues. Focusing on the specific case of osteoporosis in trabecular bone, we identify a diagnostic marker called the ratio metric that is predictive of deterioration in both osteoporotic and artificially eroded bone samples. Importantly, we demonstrate *in silico* that the ratio metric can be determined from only a few k-space values, which can be acquired rapidly with µTexture in small targeted regions within a bone. This procedure provides diagnostic information without the need to acquire an entire 2-D MR image or even a 1-D spectrum, thus avoiding the motion limitations that have previously limited the ability to probe complex bone architecture *in vivo*. By enabling the acquisition of predictive structural information in a short and non-invasive clinical procedure,

µTexture has the potential to supplement traditional bone density measurements and significantly improve the detection and monitoring of osteoporosis.

We demonstrate the feasibility of our proposed procedure through simulations of the µTexture measurement on high-resolution micro-CT bone data. We calculate the ratio metric from simulated measurements on healthy bone and artificially eroded versions of healthy bone, and find that an SVM classifier can distinguish the healthy and eroded bone using the ratio metric, with high sensitivity and specificity. We apply our classifier to simulated measurements of the ratio metric using micro-CT images of osteoporotic bone, and find that the metric is able to accurately classify healthy and diseased bone. We also show that a ratio metric measured with narrower frequency bands (i.e., fewer k-space measurements) can be used to classify healthy and eroded bone with only a minor sacrifice in accuracy, suggesting that µTexture measurements within only a few TRs could be sufficient to measure a diagnostic predictive of osteoporosis.

We note that a potential limitation of µTexture involves frequencies relevant to bone beyond which µTexture can probe. While the average trabecular thickness is on the order of 100 µm in healthy humans, Tb.Th for osteoporotic patients is much lower, and some trabeculae can be thinner than the ∼40 µm limiting wavelength of µTexture. Despite this, our results in this chapter show that µTexture is a promising tool for rapidly, non-invasively, and effectively supplementing current methods of diagnosing and monitoring bone disease. Providing information about the complex architecture of bone, which is known to be a crucial factor in determining bone strength and fragility, this procedure has the potential to substantially improve osteoporosis detection.

We also note that characterization of bone strength depends not solely on the geometry and histomorphometry at this ∼100 µm mesoscale, as can be probed with µTexture, but also on the micromechanics of bone constituents, such as mineralized collagen fibrils, at smaller scales [3, 4]. µTexture is unable to probe these scales, but a combination

of mesoscale textural measurements and microscale mechanical modeling can provide a more complete characterization of bone strength.

While this initial study focuses on trabecular bone, the methods described can be generalized to other biological tissues. µTexture can be utilized to investigate textural changes at scales down to ∼40 µm (and smaller, with the use of machine learning techniques) in a variety of tissues, including the development of fibrosis in the lungs, liver, heart, or kidney; the degradation of neuronal architecture with Alzheimer's and other neurodegenerative diseases; and the formation of tumours marked by angiogenesis, thereby informing diagnosis at early stages of disease. Furthermore, µTexture can be implemented clinically as a short, non-invasive procedure that can be repeated over time to monitor disease progression.

4.5.1 Methodological considerations

Our initial validation of the µTexture technique and the diagnostic ratio metric uses simulated measurements on a relatively small sample of four human vertebrae. Although these four bones provide a large set of VOIs for analysis and the results show promising classification performance, future work will examine the characteristics of trabecular bone across a larger dataset from a wider demographic range of individuals, in order to determine the performance of the proposed diagnostic across the population in clinical settings.

It is known that osteoporosis risk and bone architecture depend on several demographic characteristics. For example, women are more likely to develop osteoporosis than men, and the condition affects white, Hispanic, and Asian women more than black women [10]. Future studies will characterize distributions of the ratio metric across a representative sample of the population, and determine how classification boundary depends

upon factors such as age, ethnicity, or sex.

In this analysis, we use artificial erosion of healthy bone samples as a model of bone disease, in addition to testing our methods on osteoporotic bone. This choice erodes all bone elements uniformly. However, this is not necessarily the case in actual osteoporotic bone tissue, especially due to preferential resorption of unloaded trabeculae. Indeed, we observe that variability and anisotropy are fundamental characteristics of trabecular bone architecture across the samples in this study. Previous studies have emphasized the relationship between the anisotropy of trabecular bone and its mechanical properties, though additional measures are needed to fully predict bone fracture [15, 77]. The method proposed in this work determines the ratio metric through measurements on several small VOIs within the larger bone sample, without considering spatial variability in structure explicitly. Importantly, the method classifies healthy and diseased bone successfully even with this limitation. However, future work will extend the analysis of the variability in trabecular architecture in healthy and diseased bone. This variability in itself may provide important diagnostic information about the health and strength of trabecular bone, which could be leveraged to enhance the predictive capacity of the metric that we introduce here.

Finally, in this initial validation, we choose several parameters that may affect the classification outcome, including the sizes of the VOIs that μTexture samples from the bone. As described above, the ideal cross-sectional VOI size, across which the signal is averaged, will give a good trade-off between a higher signal-to-noise ratio and a finer structural resolution. For this analysis, we chose these sizes guided by both the practical limits on VOI size imposed by μTexture, and a study of which sizes produce the largest signal in the frequency bands of interest. Future work, however, will work to optimize this and other parameters through more in-depth investigations of larger datasets, in order to enable the best classification performance in clinical applications.

Chapter 5

Conclusion

In this thesis, we have developed a unique framework of integrated computational methods to probe the architecture of trabecular bone and trabecular bone-inspired structures. Recent *ex vivo* studies (e.g. [18]) have demonstrated that bone mineral density cannot fully capture the variance of bone strength, but that architectural measures can supplement BMD for a more complete characterization. Our network science and finite element analysis methods provide us with great flexibility in directly relating topological and geometric properties with mechanical response at not only the whole-network scale, but at the scale of individual trabeculae.

In this work, we quantify the importance of connectivity and trabecular orientation for stiffness, but we also examine how structures that prioritize stiffness at the expense of stability can be robust in the presence of geometric perturbations. We furthermore introduce a community detection approach for characterizing fracture locations which is inspired by prior studies of force chains in networks derived from granular packings. This method is likely to be applicable across domains and can be incorporated into a more comprehensive diagnostic tool for fracture susceptibility.

We validate an application of magnetic resonance technology to clinically assess bone

health *in vivo*. We show that a "ratio metric" extracted from frequency-domain data can be used to distinguish between healthy and osteoporotic bone. While we have focused on trabecular bone for the validation study in Chapter 4, this MR technique is organ-agnostic and can potentially be applied to other biological tissues in order to probe pathological changes in texture. Moreover, it is easily implementable using existing clinical equipment, opening up new avenues for precise, patient-oriented detection and monitoring of disease.

5.1 Future directions

Quantifying the strength, robustness, and resilience of bone at millimeter scales is only one part of the picture. Bone is a complex material with structured components at many smaller scales (Fig. 5.1). Efforts exist to probe each of these constituents, but a complete characterization of bone strength and fracture resistance must link together the spatial scales spanning nanoscale polymer networks and interfaces, microscale mineralized collagen fibrils, and the trabecular architecture at large. Possible modeling approaches are highlighted in Fig. 5.1, but *in silico* and *ex silico* analyses should be undertaken in tandem such that data can inform the design of models, and computational results can inform the design of experiments. The scale of macroscopic trabecular architecture is relatively data-rich: micro-CT technology is able to image large-scale trabecular structure in high resolution, and mechanical tests can be performed in the laboratory on *ex vivo* specimens for precision analysis of the elastic properties of bone. However, the smaller scales of trabeculae and mineralized collagen fibrils are data-poor in comparison, but micro- and nanoindentation techniques, for example, which involve indenting a test sample with an extremely small, hard tip, have been developed for testing bone strength at these small scales.

At the microscale are mineralized collagen fibrils, the "building blocks" of bone.

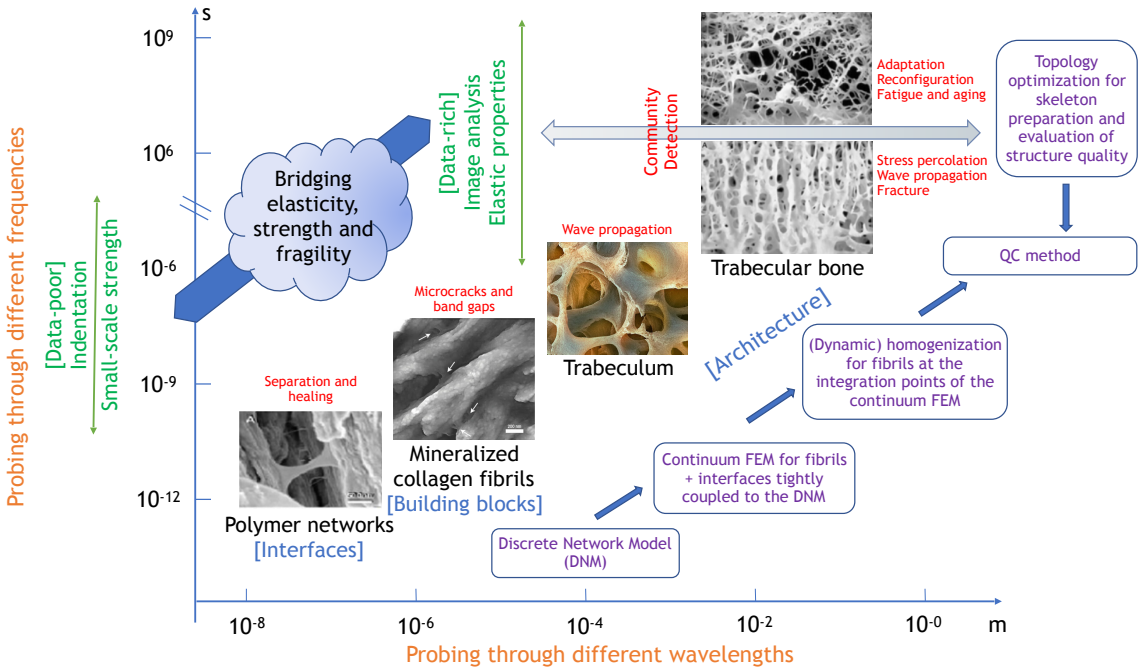

Figure 5.1: Overview schematic of the hierarchical structure and strength mechanisms in trabecular bone, and modeling approaches to bridge spatial scales. Figure courtesy of Ahmed Elbanna.

Mineralized collagen fibrils consist of platelets of stiff hydroxyapatite (calcium phosphate) embedded in a soft matrix of collagen molecules. The platelets, which are elongated in one direction, are arranged periodically within the matrix, resulting in the potential emergence of band gaps for elastic and acoustic waves. The existence of band gaps will influence the response of bone to dynamic loading. Understanding the relationship between band gaps and fracture resistance is especially important as the bulk of loads placed on bone are dynamic (e.g., from walking or running, or from impacts such as falling), rather than static or quasistatic, as considered in our previous work.

It has also been found that mineralized collagen fibrils contain fracture resistance mechanisms at the nanoscale known as sacrificial bonds and hidden length [84]. The fibrils are embedded in an organic matrix that functions as a glue to hold them together. When fibrils start to separate due to applied forces, this "glue" forms filaments that

resist the separation of the fibrils. Weak "sacrificial" bonds in the filaments break first, allowing energy to dissipate; these sacrificial bonds can reform when the load is removed. (Sacrificial bonds and hidden length have been observed at even smaller length scales, in the constituent molecules of bone tissue [85].) Integrating the (micro-)scales of band gaps within fibrils and the (nano-)scales of the interfaces between fibrils and the surrounding matrix will be important for identifying the emergent collective behavior of the building blocks of bone.

Our work presented here can be highly synergistic with a wide range of other disciplines. Complex, hierarchical materials are found in many biological, geological, and physical systems, and the modeling framework described in this thesis can be extended and applied to other systems such as earthquake faults, polymers, and other biological tissues, as well as engineered systems such as truss structures and bio-inspired materials. Nacre, for instance, is another naturally-occurring composite material that comprises inorganic platelets embedded semi-regularly in an organic matrix [86], and has inspired the development of impact-resistant glass [87]. As with bone, understanding the mechanisms of strength and dynamics that span multiple spatial and/or temporal scales is necessary for quantifying strength and predicting vulnerabilities in these systems.

Appendix A

Structural and topological metrics

This appendix contains a detailed list of metrics commonly used in histomorphometry and network science.

A.1 Histomorphometric quantities

The terminology for the histomorphometric quantities defined below follow from the standardized nomenclature proposed in [37]. In this work, histomorphometry is performed using Bruker CT-analyser [42] and BoneJ [46], and the calculation methods described below are those utilized by these software packages.

Trabecular thickness (Tb.Th). The local thickness of trabeculae is typically measured using a sphere-fitting procedure, wherein the trabecular bone volume is first skeletonized to identify the medial axes of the trabeculae, and spheres are fit along these axes. The local thickness at a point is given by the diameter of the largest sphere that contains the point and is bounded within the edges of the structure. Tb.Th is usually defined as a single value representing the mean trabecular thickness within a specified region, though the distribution of Tb.Th is commonly used as well.

Trabecular separation (Tb.Sp). Trabecular separation, or sometimes trabecular spacing, is determined with the same method as trabecular thickness, but applied to the voids rather than the bone.

Trabecular number (Tb.N). Trabecular number is a measure of the density of trabeculae and represents the number of crossings of bone per unit length on a random linear path through a specified volume. Trabecular number can be measured directly, or can alternatively be defined as

$$Tb.N = \frac{1}{Tb.Th + Tb.Sp}$$

Degree of anisotropy (DA). The degree of anistropy measures the extent to which trabeculae are preferentially aligned along a certain direction. If a structure is isotropic, then there is no preferential alignment. Anisotropy can be probed by measuring the mean intercept length (MIL). MIL analysis involves measuring how many times a straight line sent through a volume would pass through bone; the MIL is the length of the line divided the number of times it passes through bone. More specifically, a grid of lines is sent through the volume and rotated over a large range of angles (in 3-D space). The MIL for each angle is calculated as an average over the grid. Each MIL value can be visualized as a line passing through the origin, oriented at its corresponding angle, with length equal to the MIL. An ellipsoid is fit to this 3-D distribution of MIL; the resulting ellipsoid can be described by three orthogonal vectors collected into a tensor. The degree of anisotropy can be expressed either as the maximum eigenvalue of this tensor divided by the minimum (ranging from 1, completely isotropic, to infinity, completely anisotropic), or as 1 minus the ratio of the minimum eigenvalue to the maximum (ranging from 0 for completely isotropic to 1 for anisotropic).

In this work, we do not calculate the degree of anisotropy with histomorphmetric

methods. Rather, by representing trabecular bone as spatially-embedded networks, we determine the distribution of orientation; we calculate the angle each link makes relative to the vertical direction.

Percent bone volume (BV/TV). The percent bone volume measures the fraction of total volume that is occupied by bone. For a binarized image, then, this is equivalent to the number of voxels with value 1 divided by the total number of voxels.

A.2 Graph topological metrics

Networks can be mathematically summarized by graphs, a collection of *nodes* or *vertices* that are connected by *edges* or *links* (in this work, we use the terms edges and links interchangeably). All information about a network with N nodes is encompassed by an $N \times N$ matrix called the adjacency matrix, typically denoted $\mathbf{A}$. The elements of $\mathbf{A}$ represent the edges between nodes and are 0 if an edge does not exist between a pair of nodes or a nonzero number if an edge exists. Edges can be weighted to symbolize the varying strength of connections between nodes. If the connections are unweighted, the nonzero elements are equal to 1, and the graph is a binary graph. If the connections are weighted, the nonzero elements are equal to the corresponding edge weights. The diagonal elements of $\mathbf{A}$ are 0 unless the network contains self-loops. The graphs considered in this thesis are *simple graphs* and therefore do not contain self-loops or multiple edges between a pair of nodes.

If the network is undirected, $\mathbf{A}$ is symmetric. For a directed network, an edge has a direction, pointing from one node to another. Hence A_{ij} is not necessarily equal to A_{ji}, and $\mathbf{A}$ is generally not symmetric. In this thesis, all networks are undirected.

Degree. The degree of a node is the number of edges connected to the node. For an

undirected network, the degree k of node i is given by

$$k(i) = \sum_j A_{ij} \tag{A.1}$$

where A_{ij} refers to the element of the adjacency matrix in row i and column j, which is 0 if there does not exist an edge between nodes i and j; 1 if there is an edge between nodes i and j and the network is unweighted; or a nonzero value representing the edge weight between nodes i an j if the network is weighted.

The networks analyzed in Chapters 2 and 3 are weighted, with edge weights corresponding to the average trabecular thicknesses of the trabeculae represented by the edges.

Assortativity. Assortativity refers to the tendency of nodes to be connected to nodes with similar characteristics. In particular, we consider *degree assortativity*, which measures the likelihood that nodes are connected to other nodes of similar degree, i.e., high-degree nodes connected to other high-degree nodes, and low-degree nodes connected to other low-degree nodes. The degree assortativity is described by a Pearson correlation coefficient given by

$$r = \frac{\sum_{ij}(A_{ij} - k_i k_j/2m)k_i k_j}{\sum_{ij}(k_i\delta_{ij} - k_i k_j/2m)k_i k_j}, \tag{A.2}$$

where A_{ij} is the element of the adjacency matrix corresponding to the link between nodes i and j, k_i is the degree of node i, m is the total number of links, and δ_{ij} is the Kronecker delta [24]. If the assortativity is positive (up to 1), then like is linked to like, and *assortative mixing* is said to occur. If assortativity is negative (down to -1) like is linked to unlike, resulting in *disassortative mixing*. If assortativity is 0, then the network is said to be neutral.

It must be mentioned, however, that this is not the most efficient way to calculate

assortativity; rather, we can write

$$r = \frac{S_1 S_e - S_2^2}{S_1 S_3 - S_2^2}, \tag{A.3}$$

where $S_n = \sum_i k_i^n$ and $S_e = \sum_{ij} A_{ij} k_i k_j = 2 \sum_{\text{edges}(i,j)} k_i k_j$, where the sum over edges (i, j) refers to a sum over all distinct pairs of nodes i and j that are connected by an edge (rather than summing over all pairs of nodes, regardless of whether or not they are connected) [24].

Modularity. Roughly speaking, modularity is a measure of how easily a network can be partitioned into groups of nodes that share similar characteristics: the fraction of links that connect nodes of the same type, minus the expected fraction of links connecting nodes of the same type if the links were randomly assigned between nodes. Let c_i represent the type of node i, or rather the "community" it belongs to. The total number of links between nodes of the same type is given by

$$\frac{1}{2} \sum_{ij} A_{ij} \delta(c_i, c_j), \tag{A.4}$$

where δ is the Kronecker delta and the $\frac{1}{2}$ is due to the double counting of links that occurs when summing over i and j. If links were distributed at random, the expected number of links between nodes i and j would be $k_i k_j / 2m$. If node i has degree k_i, and there are m total links in the network (and $2m$ ends of links), then the probability that the end of one link connected to node i is connected to node j would be $k_j / 2m$, where k_j is the degree of node j. Then the expected number of links that connect all pairs of nodes within the same community is

$$\frac{1}{2} \sum_{ij} \frac{k_i k_j}{2m} \delta(c_i c_j). \tag{A.5}$$

The modularity Q is given by the difference of expressions A.4 and A.5, divided by the total number of edges (m):

$$Q = \frac{1}{2m} \sum_{ij} \left(A_{ij} - \frac{k_i k_j}{2m} \right) \delta(c_i, c_j). \tag{A.6}$$

Community structure. Community structure follows from the concept of modularity: a network has community structure it can easily be partitioned into clusters wherein nodes within a cluster are densely connected to each other, but sparsely connected to nodes outside the cluster. The technique of identifying community structure is known as community detection and is often achieved by maximizing the modularity. Modularity maximization is computationally extremely difficult and many heuristic algorithms have been developed for community detection, one common method being the Louvain method. Various software packages exist for performing community detection; this work uses the GenLouvain package developed for MATLAB [88].

The modularity function that is maximized need not be identical to Eq. A.6. A general expression for modularity is given by

$$Q = \sum_{ij} \left(A_{ij} - \gamma P_{ij} \right) \delta(c_i, c_j), \tag{A.7}$$

where γ is a specified *resolution parameter* that modulates the size of the communities, and P_{ij} is the *null model* term. A common choice of null model is the *Newman-Girvan null model* [89], whereby

$$P_{ij} = k_i k_j / 2m,$$

recovering the modularity expression in Eq. A.6 (times $2m$). This null model, which, again, corresponds to a random rewiring of links, assumes that any two nodes can be connected. However, this may not always be the case for a given network, and alternative

null models may be used, especially if physical properties must be taken into account. One choice is the *geographical null model*, initially developed in the context of neuroscientific networks with ordered nodes connected only to their nearest neighbors (chain networks) [32]. Geographical null models have also been applied to force networks in granular materials, which consist of nodes that represent individual particles and links representing forces between particles [28, 63, 64]. Such a network has spatial constrains in that only nodes that represent particles in contact can be connected. The geographical null model is given by

$$P_{ij} = \rho B_{ij}, \tag{A.8}$$

where ρ is the average weight of edges in the network, and B_{ij} is the ij component of the *binary* adjacency matrix $\mathbf{B}$. The binary adjacency matrix is the same as the adjacency matrix, except that all nonzero elements are set to 1.

Appendix B

Appendix for Chapter 2

This appendix contains supplementary information for Chapter 2.

B.1 Data availability

The data analyzed in this work are available online at the following Figshare repositories:

- https://doi.org/10.6084/m9.figshare.7771046.v1
- https://doi.org/10.6084/m9.figshare.7771043.v1
- https://doi.org/10.6084/m9.figshare.7771040.v1
- https://doi.org/10.6084/m9.figshare.7834859.v1

Datasets comprise thresholded and despeckled micro-CT images constituting the 40 VOIs; the respective skeletonizations; network models generated from the skeletonized bone and corresponding histomorphometric, geometric, and topological metrics; and networks representing the pores between trabeculae (the "dual" of the bone networks).

B.2 Structural metrics

In addition to the standard histomorphometric and network topological metrics described in further detail in Appendix A.1 and A.2, we also introduce several structural metrics used in our analysis.

Pore width. Pore width refers to the average width of a pore within trabecular bone and is calculated using the method of sphere fitting [90], which is also used to determine trabecular thickness (Appendix A.1). In this work, we make a distinction between pore width and trabecular separation in that Tb.Sp is used to refer to an average value representative of an entire VOI, while pore width refers to the size of an individual void.

Trabecula width. Trabecula width refers to the average width of a trabecula, also calculated with sphere fitting. Again, we use trabecula width to refer to the width of a single trabecula, while trabecular thickness (Tb.Th) refers to the average of trabecula widths in an entire VOI.

Link length. The length of a link in the network model, equivalent to the length of the medial axis of the corresponding trabecula.

Link orientation. Link orientation captures the extent to which a link points along a specified axis. For a specific link d, we can define a vector $\vec{d}$ connecting the nodes of the links. For a given axis a with corresponding unit vector $\hat{a}$, the link orientation with respect to a is defined as:

$$O_a(d) = \frac{\vec{d} \cdot \hat{a}}{||d||}. \tag{B.1}$$

This metric can be thought of as the direction cosine between the a axis and link d. This is not broadly applicable to any graph as it can only be applied to networks embedded in physical space. In this thesis, we define the principal direction of loading as being parallel to the Z-axis (corresponding to the superior-inferior direction parallel to the spine). We

focus on orientation with respect to this direction, which we call Z-orientation, due to the role the loading direction plays in the anisotropy of trabecular structure. Past studies have shown that with age and osteoporosis, trabeculae with low Z-orientation tend to be preferentially resorbed and become thinner on average, while those with a high Z-orientation (more parallel to the loading direction) retain their thickness or even become thicker since they are preferentially rebuilt [91].

Weighted link orientation. Weighted link orientation refers to orientation weighted by the thickness of the corresponding link. For a link d, the weighted orientation WO with respect to direction a is defined as:

$$WO_a(d) = \frac{O_a(d)w(d)}{\sum_i w(i)}, \tag{B.2}$$

where $O_a(d)$ is the orientation of link d, $w(d)$ is its weight (thickness), and $\sum_i w(i)$ is a sum over all weights of links in the network. The sum of weighted link orientation over all the links in a VOI gives the VOI-scale measure of the weighted orientation and indicates the prevailing directionality of a trabecular network. As with link orientation, we focus on the weighted Z-orientation in this work.

Number of links. The total number of links in a network, representative of the number of trabeculae.

B.3 Comparison of mechanical response

We validate our beam model approximation by comparing results of simulated compression with that of a continuum model. Initial comparisons between the two show that the continuum model is stiffer than the beam model. In order to match the stiffnesses of the two models, the radius of the beams in the beam model is increased by an overall

scale factor of 1.55 for the example VOI shown in the main text. Figure B.1 indicates agreement of the force-displacement curves (in the linear regime) of the continuum model and the beam model after incorporating the overall scale factor.

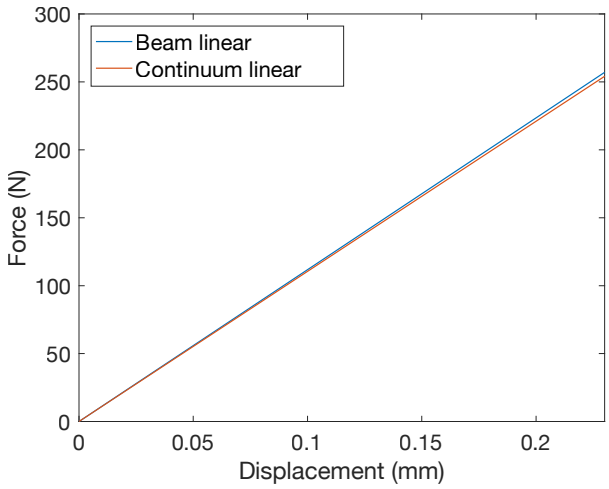

Figure B.1: Force-displacement curve for the beam-element and continuum models in the linear regime. The force-displacement response is nearly identical, and the two lines overlap.

B.4 Stress distribution

As discussed in Chapter 2.4.2, the cumulative distribution of stress shifts when the differing volume fractions of each beam is taken into account. Fig. B.2 is the counterpart to Fig. 2.8, wherein the cumulative fraction of beams is replaced by the cumulative volume fraction. $\zeta'_{0.001}$ is the fraction of the total bone volume encompassed by beams with normalized stress less than or equal to 0.001, and ninety percent of the total volume fraction bears a stress less than or equal to $\sigma'_{0.9}$.

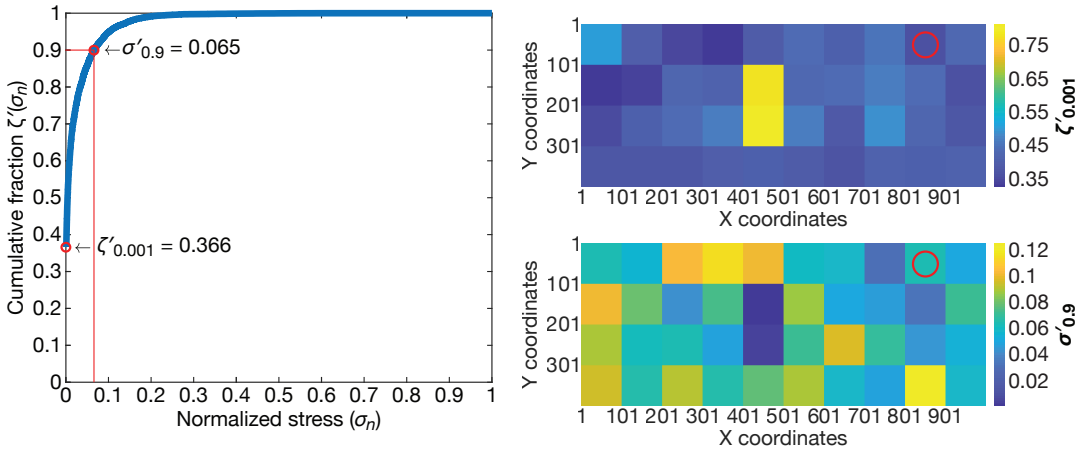

Figure B.2: Left: Distribution of normalized maximum principal stress in the beam elements of an example beam model (Fig. 2.7) under compressive loading in the linear regime. Stress σ_n is normalized to the largest value of stress in a beam at the final timestep of the compressive loading simulation. The function ζ' is the fraction of the total bone volume encompassed by the beams that bear a normalized stress less than or equal to σ_n. $\zeta'_{0.001}$ is defined as the volume fraction of beams that bear a normalized stress less than or equal to 0.001 and $\sigma'_{0.9}$ is defined as the normalized stress that satisfies the equation $\zeta'(\sigma_{0.9}) = 0.9$. In this VOI, 37% of the total volume bears a normalized stress less than 0.001 ($\zeta_{0.001} = 0.366$), while 90% of the total volume bears a normalized stress less than or equal to 0.065 ($\sigma_{0.9} = 0.065$). Right: Spatial distributions of $\zeta'_{0.001}$ and $\sigma'_{0.9}$ across the sample. The example VOI is indicated by the red circle.

Variable omitted	Adjusted r^2
None	***0.872***
Assortativity	0.878
Degree	**0.829**
Weighted degree	**0.837**
Volume fraction	0.875
Tb.Sp	**0.856**
Tb.Th	0.875
Link length	**0.859**
Z-orientation	**0.853**
Weighted Z-o	**0.857**
Number of links	**0.740**

Table B.1: Adjusted r^2 values for multiple linear regression with nine variables. We determine the redundancy of variables in the multiple linear regression model by comparing the adjusted r^2 of a ten-variable linear model against that of all possible nine-variable models, each of which are labeled with the variable omitted. The adjusted r^2 for the ten-variable model (no variables omitted) is italicized and indicated in bold. The variables whose omission results in a reduction of the adjusted r^2 are highlighted in bold.

B.5 Multiple linear regression

We quantify the redundancy of metrics in our multiple linear fit by calculating the adjusted r^2 for our model. The adjusted r^2 measures the predictiveness of a model with a penalty for the number of explanatory variables. For a linear model containing degree, weighted degree, trabecular spacing, link length, Z-orientation, and weighted Z-orientation, adding any additional variable to the model, with the exceptions of assortativity and trabecular thickness, also decreases the adjusted r^2.

Variable added	Adjusted r^2
None	***0.882***
Assortativity	0.878
Volume fraction	0.879
Tb.Th	0.879

Table B.2: Adjusted r^2 values for multiple linear regression with five variables. We determine the redundancy of variables in the multiple linear regression model by comparing the adjusted r^2 of a 7-variable linear model consisting of the 7 significant metrics (Table III of the main text), with the adjusted r^2 of all possible eight-variable models. Each of the eight-variable models is labeled by the variable that is added to the seven-variable model. The adjusted r^2 for the seven-variable model (no variables added) is italicized and indicated in bold. All eight-variable models result in a decrease in the adjusted r^2.

Appendix C

Appendix for Chapter 3

This appendix contains supplementary information for Chapter 3.

C.1 Methodological considerations

The individual objective functions in the optimization problem (Eq. 6 of the main text) are normalized so that their respective magnitudes are more consistent. Given that the compliance and stability functions can take values at or near infinity (for purely void structures) and the maximum value of the perimeter function is limited by the filter length scale (an alternating solid-void design with no structural links), a finite normalization scheme may disproportionately normalize those functions relative to the perimeter function. As a result the function weights may appear disproportionate, but could be made more similar (or even uniform) by using modified normalization factors. For reference, Table C.1 shows the percent of the weighted objective sum contributed by each function for the compliance and perimeter models (a 50-50 split indicates equal weighted values for each function).

Model	Compliance Contribution	Perimeter Contribution
C92P08_1	63.2	36.8
C92P08_2	64.3	35.7
C92P08_3	65.0	35.0
C92P08_4	63.2	36.8
C92P08_5	77.9	22.1
C92P08_6	68.4	31.6
C92P08_7	61.3	38.7
C92P08_8	72.0	28.0
C92P08_9	70.5	29.5
C92P08_10	56.5	43.5
C92P08_11	62.4	37.6
C92P08_12	65.8	34.2
C99999P00001_1	100.0	0.0222
C99999P00001_2	100.0	0.0288
C99999P00001_3	100.0	0.0303
C99999P00001_4	100.0	0.0274
C99999P00001_5	100.0	0.0192
C99999P00001_6	100.0	0.0118
C99999P00001_7	100.0	0.0083
C99999P00001_8	100.0	0.0158
C99999P00001_9	100.0	0.0117
C99999P00001_10	100.0	0.0140
C99999P00001_11	100.0	0.0220
C99999P00001_12	100.0	0.0205
C99P01_1	94.6	5.4
C99P01_2	90.7	9.3
C99P01_3	92.2	7.8
C99P01_4	91.5	8.5
C99P01_5	93.9	6.1
C99P01_6	94.3	5.7
C99P01_7	96.0	4.0
C99P01_8	93.9	6.1
C99P01_9	95.0	5.0
C99P01_10	93.0	7.0
C99P01_11	95.0	5.0
C99P01_12	93.7	6.3

Table C.1: Percent contribution of compliance and perimeter functions to weighted objective sum for models with no stability objective.

C.2 Topology-optimized structures

Twelve structures were generated for each of the seven sets of objective weights. The initial density distribution was perturbed slightly for each optimization run to produce variation in architecture. Structures for each parameter set are shown in Figs. C.1-C.7.

C.3 Force-displacement response

While we only consider the force-displacement response between the origin and the point at which it has reached zero for each structure (indicating total failure), we include the full force-displacement curves here for completeness (Fig. C.8). The data used to generate Fig. 4 of the main text are also shown as boxplots in Fig. C.9 to facilitate comparison between the response of the original and perturbed models.

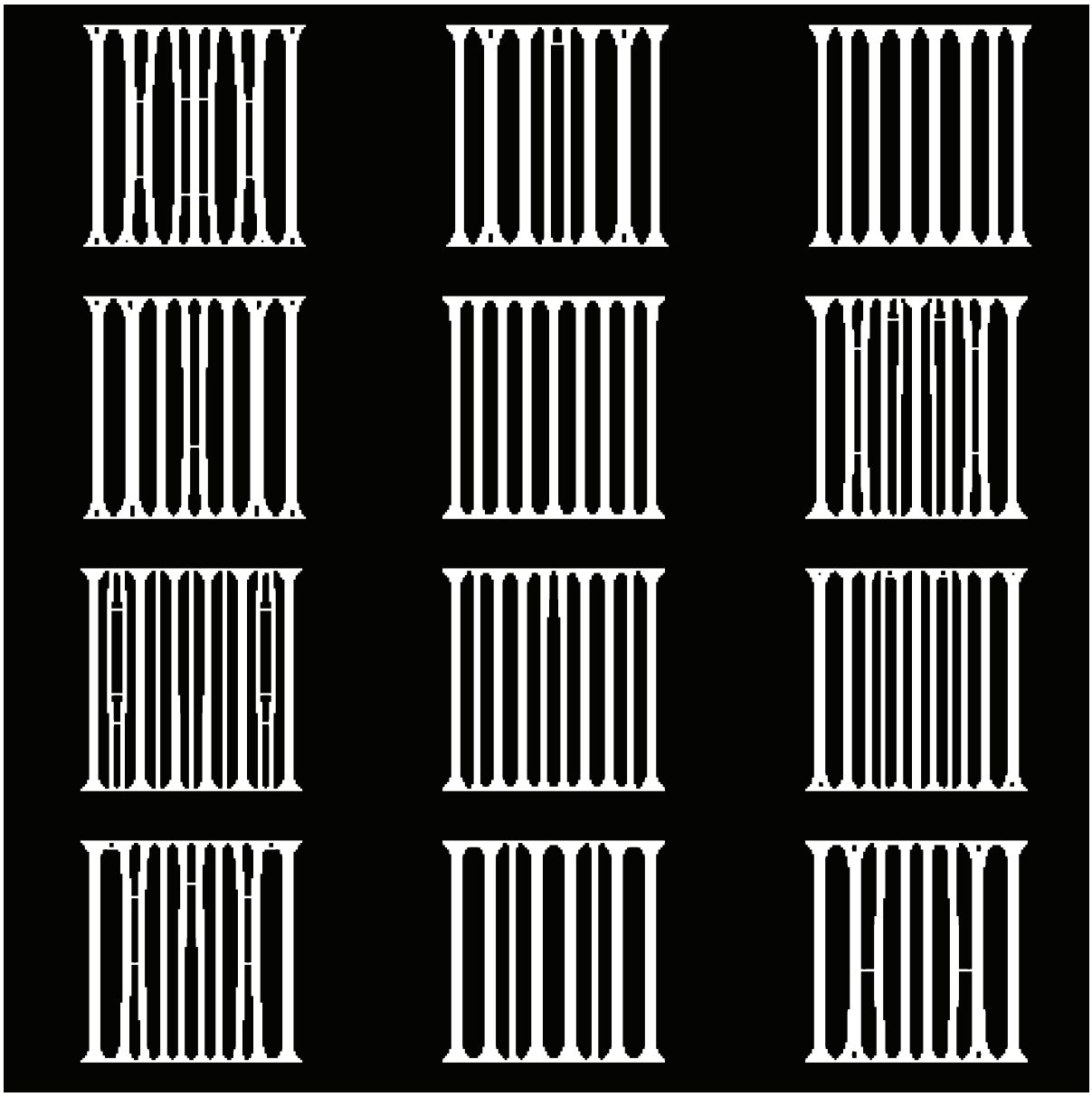

Figure C.1: Structures generated using C99999P00001 objective weights.

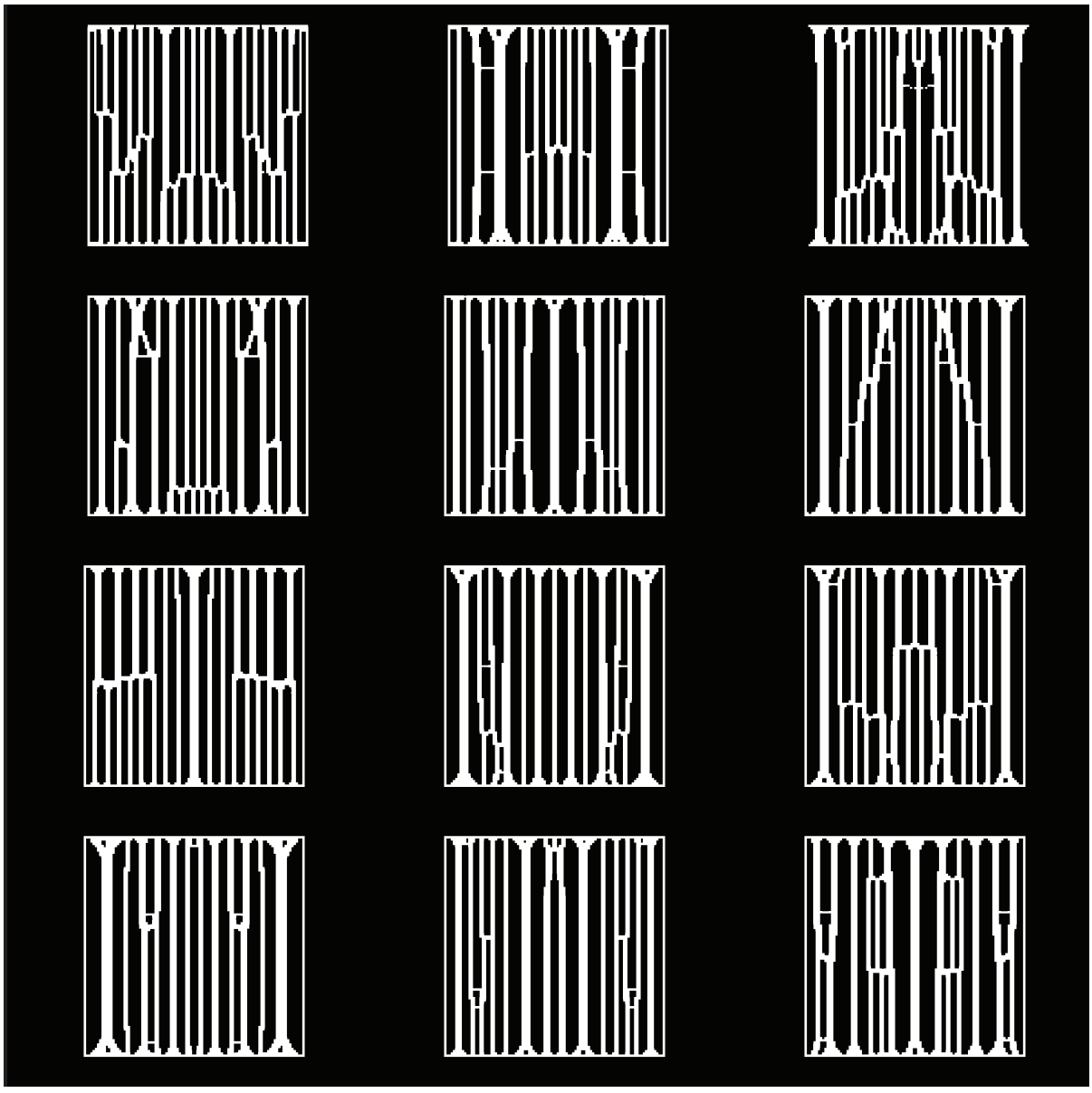

Figure C.2: Structures generated using C99P01 objective weights.

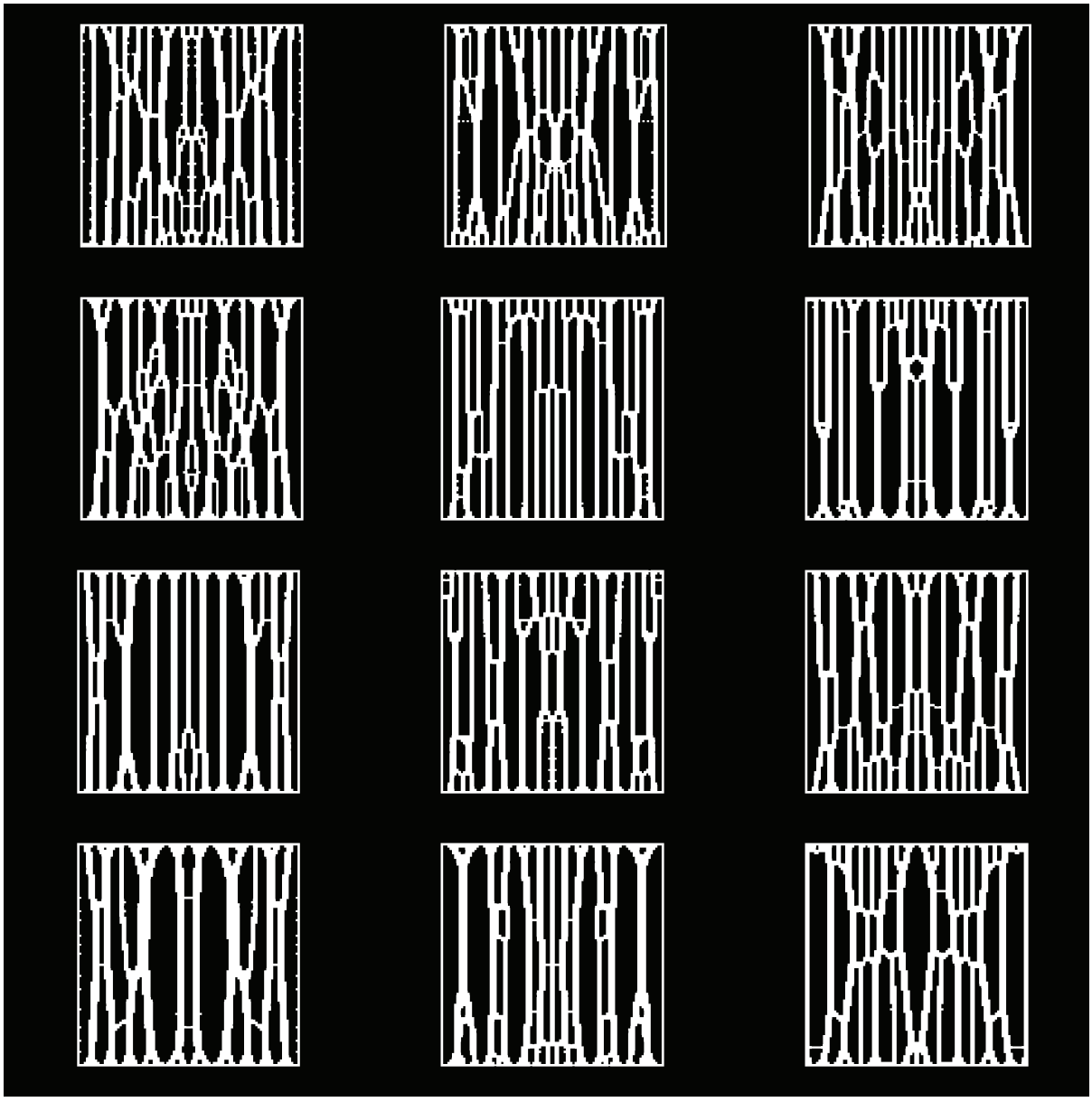

Figure C.3: Structures generated using C92P08 objective weights.

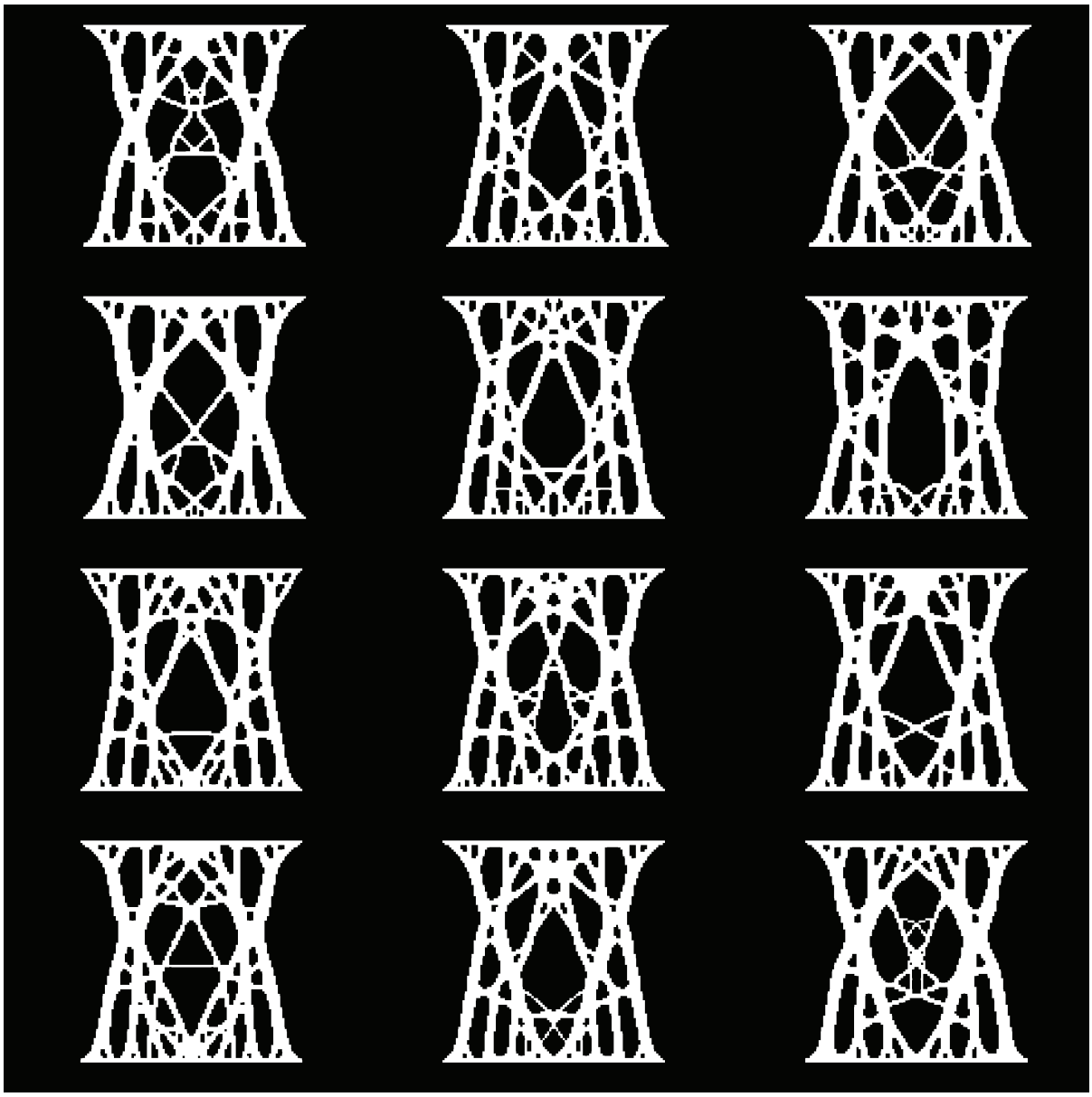

Figure C.4: Structures generated using C50S50 objective weights.

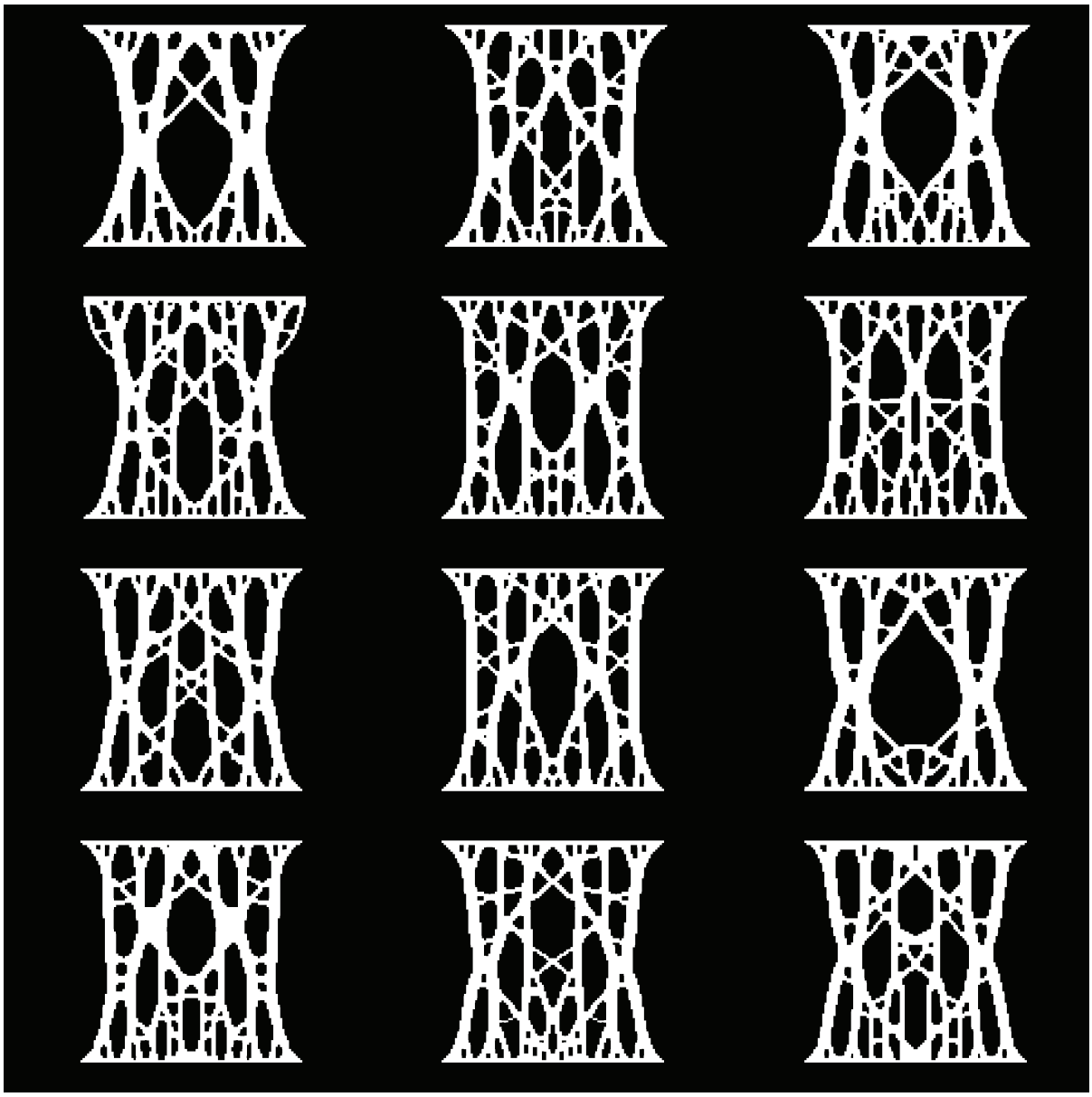

Figure C.5: Structures generated using C65S35 objective weights.

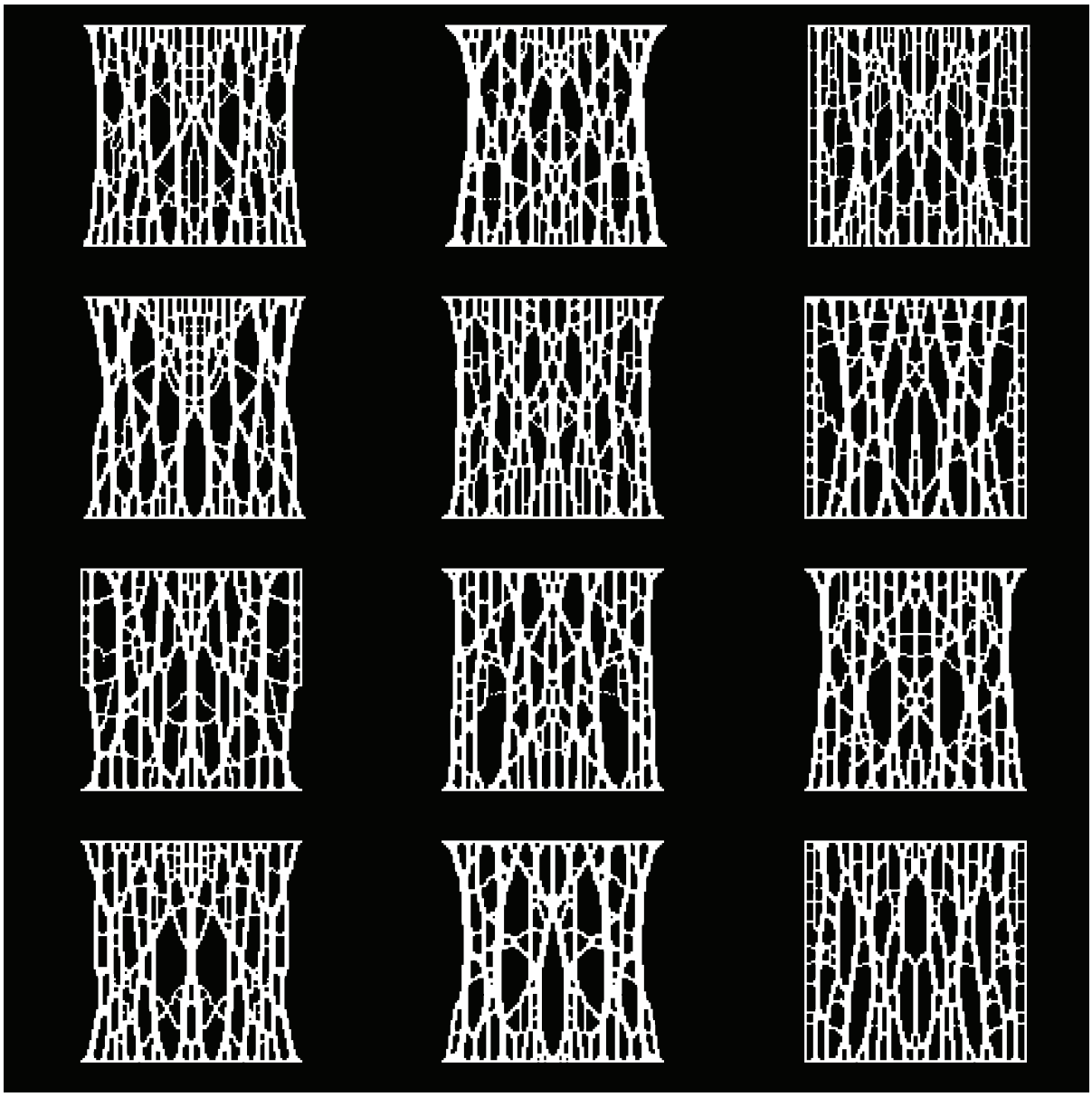

Figure C.6: Structures generated using C85P05S10 objective weights.

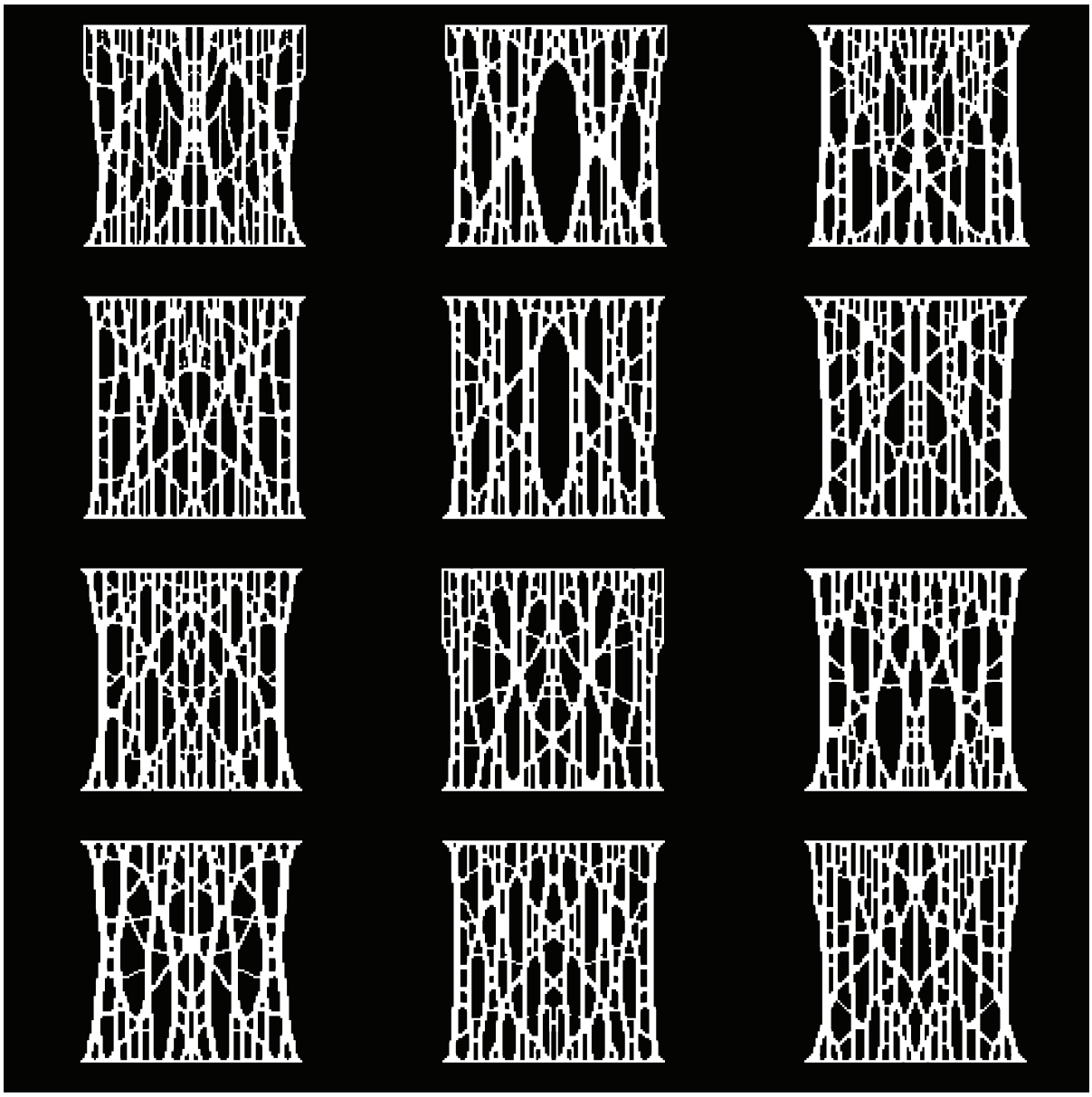

Figure C.7: Structures generated using C88P01S11 objective weights.

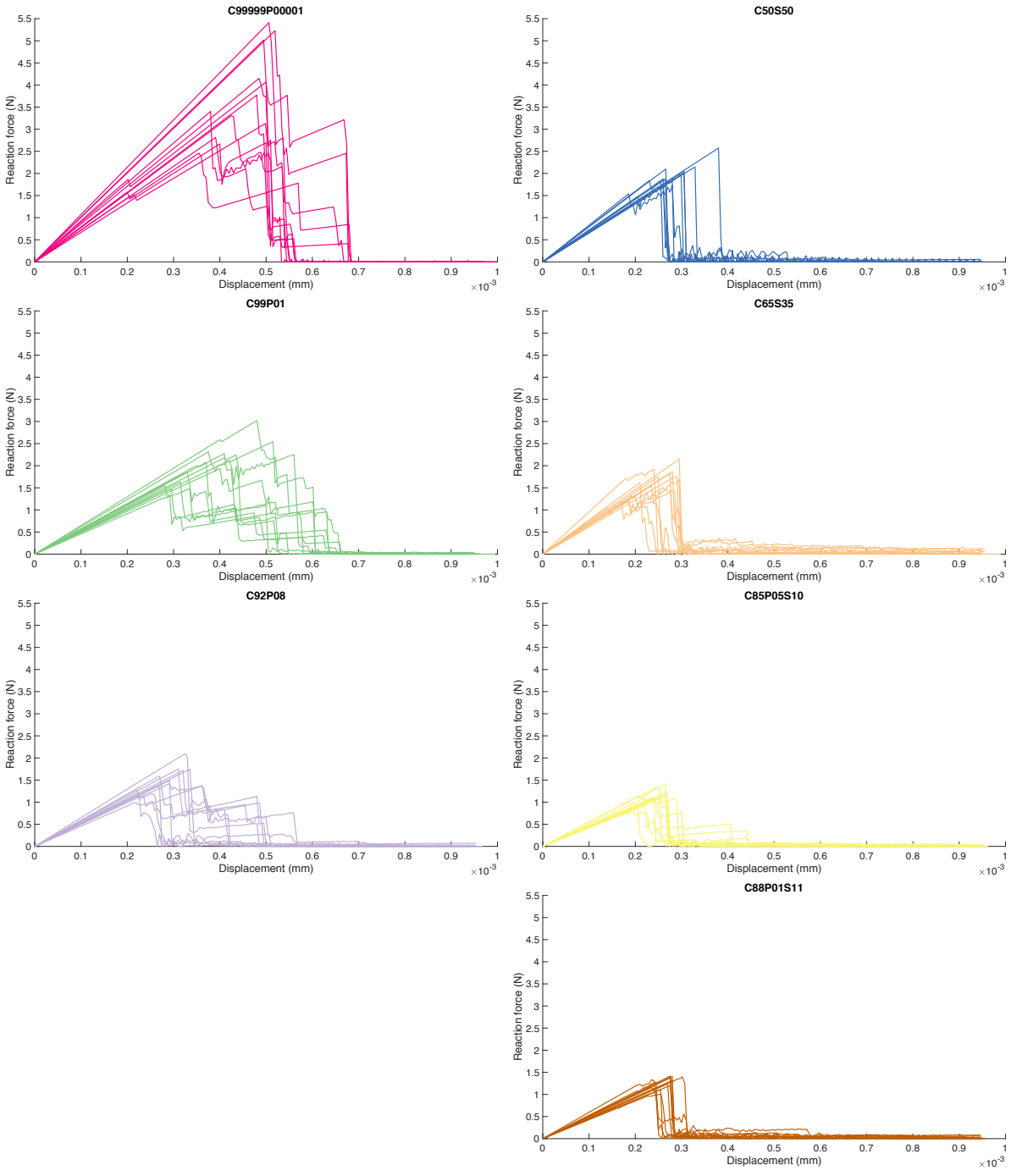

Figure C.8: Force-displacement curves for each structure in a parameter set.

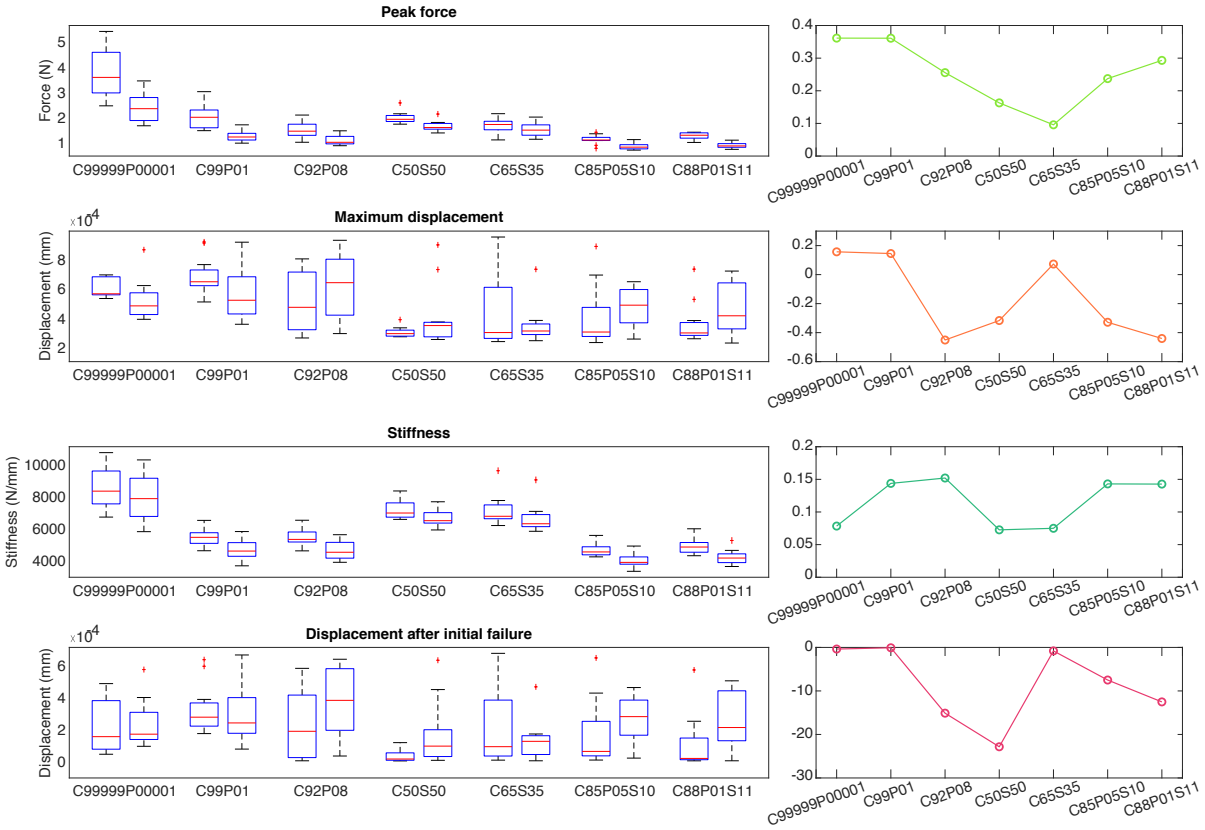

Figure C.9: Left column: boxplots indicating variation in peak force, maximum displacement, stiffness, and displacement between initial beam failure and system failure. Each pair of plots represents the same parameter set, with the left boxplot corresponding to the original model and the right boxplot to the perturbed model. Right column: percent difference between original and perturbed model, averaged over each model within the same parameter set, for each of the four metrics shown on the left.

Appendix D

Appendix for Chapter 4

This appendix contains supplementary information for Chapter 4. Figs. D.1 and D.2 demonstrate the integrated power in frequency bands [1.0, 1.8] mm^{-1} and [3.8, 7.4] mm^{-1}, respectively, as a function of the size of the analyzed prism. These figures illustrate that the highest power is achieved for prisms with small cross-section sizes and longer analysis dimensions; hence, we choose prisms with 1 mm cross-section widths and 5 mm analysis lengths.

Table D.1 contains the average ratio metric values for the baseline and eroded versions of each dataset, while Tables D.2 and D.3 contain the corresponding sensitivities and specificities for classifying baseline and eroded data. Table D.4 contains the average ratio metric for osteoporotic data, as well as classification sensitivities.

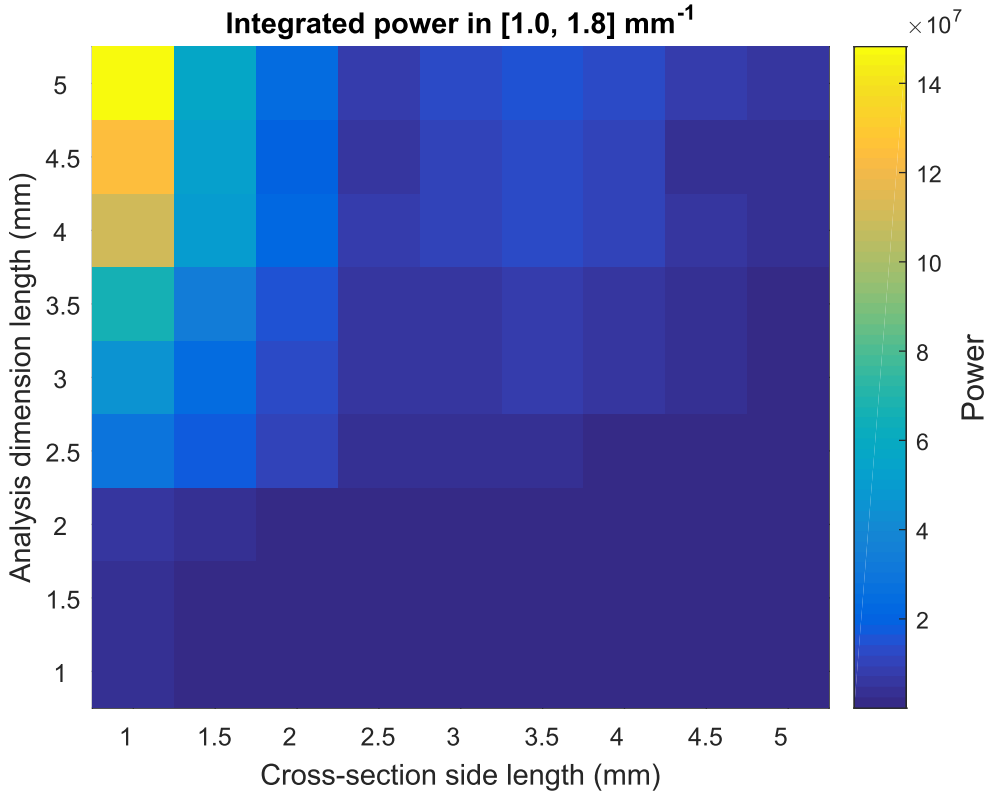

Figure D.1: Integrated power increases as analysis length increases and cross-section size decreases. The integrated power in frequency band $[1.0, 1.8]$ mm^{-1}, corresponding to the low-frequency (Tb.Sp) band used to determine the ratio metric, is calculated for prisms of varying analysis dimension length and cross-section side length. The cross-section is kept square. Each data point is obtained by averaging over 100 prisms of the same size from different locations in the baseline thresholded AE12L2 dataset. The highest integrated power occurs for a prism with 1 mm $\times$ 1 mm cross-sectional area and 5 mm analysis length. To calculate the ratio metric, we use prisms of this size, which also corresponds to approximately the smallest resolution and machine parameters that can be acquired with µTexture.

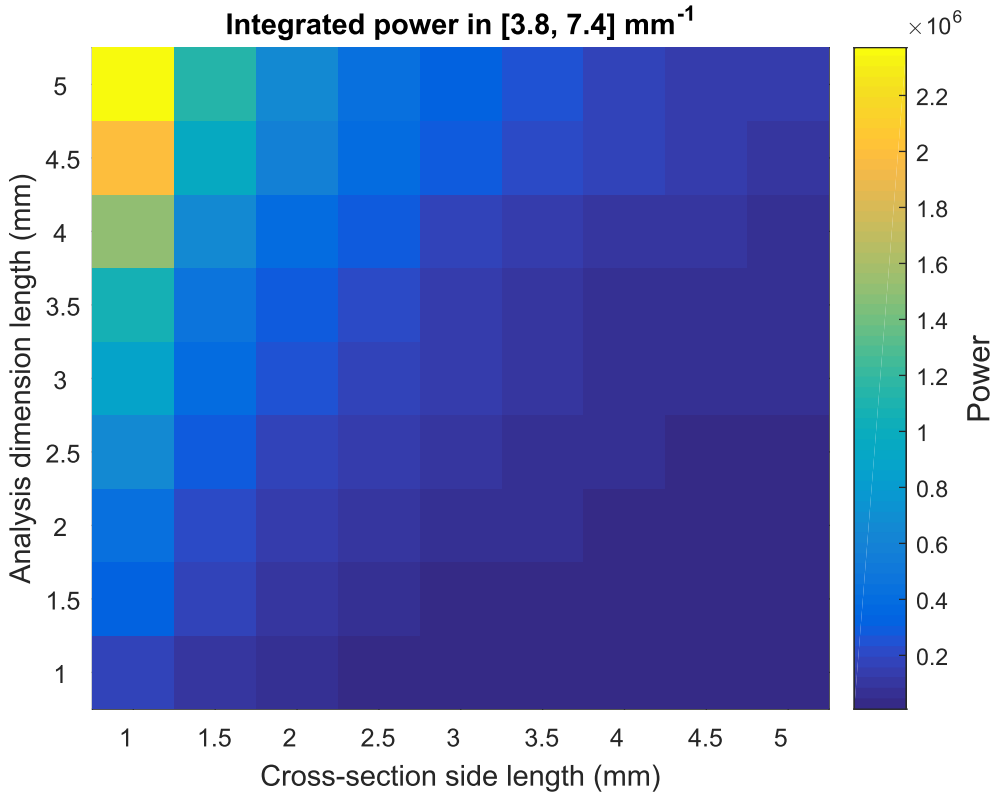

Figure D.2: Integrated power increases as analysis length increases and cross-section size decreases. The integrated power in frequency band $[3.8, 7.4]$ mm^{-1}, corresponding to the high-frequency (Tb.Th) band used to determine the ratio metric, is calculated for prisms of varying analysis dimension length and cross-section side length. The cross-section is kept square. Each data point is obtained by averaging over 100 prisms of the same size from different locations in the baseline thresholded AE12L2 dataset. The highest integrated power occurs for a prism with 1 mm $\times$ 1 mm cross-sectional area and 5 mm analysis length. To calculate the ratio metric, we use prisms of this size, which also corresponds to approximately the smallest resolution and machine parameters that can be acquired with µTexture.

Table D.1: Mean ratio metric of of baseline and eroded healthy bone samples.

Sample	Analysis direction	Baseline	Eroded (2-voxel)	Eroded (4-voxel)
AE12L2	Anterior-posterior	0.95 ± 0.08	0.74 ± 0.08	0.63 ± 0.09
AE12L2	Medial-lateral	0.92 ± 0.07	0.74 ± 0.08	0.61 ± 0.10
AE12L2	Superior-inferior	0.91 ± 0.09	0.77 ± 0.10	0.70 ± 0.11
F60L3	Anterior-posterior	0.95 ± 0.09	0.82 ± 0.10	0.71 ± 0.11
F60L3	Medial-lateral	0.90 ± 0.08	0.78 ± 0.09	0.67 ± 0.11
F60L3	Superior-inferior	0.72 ± 0.09	0.74 ± 0.11	0.60 ± 0.11
Both	Anterior-posterior	0.95 ± 0.08	0.77 ± 0.10	0.66 ± 0.10
Both	Medial-lateral	0.91 ± 0.08	0.75 ± 0.09	0.63 ± 0.10
Both	Superior-inferior	0.84 ± 0.13	0.76 ± 0.10	0.66 ± 0.12

Average ratio metric of baseline and eroded samples for each analysis direction and sample. Error denotes one standard deviation.

Table D.2: Classification accuracy of baseline and eroded (2-voxel radius) healthy bone samples.

Sample	Analysis direction	Sensitivity	Specificity
AE12L2	Anterior-posterior	0.924 ± 0.008	0.916 ± 0.003
AE12L2	Medial-lateral	0.890 ± 0.009	0.919 ± 0.004
AE12L2	Superior-inferior	0.761 ± 0.009	0.838 ± 0.007
F60L3	Anterior-posterior	0.762 ± 0.014	0.782 ± 0.012
F60L3	Medial-lateral	0.761 ± 0.011	0.793 ± 0.014
F60L3	Superior-inferior	0.433 ± 0.086	0.540 ± 0.087
Both	Anterior-posterior	0.841 ± 0.004	0.872 ± 0.004
Both	Medial-lateral	0.847 ± 0.004	0.873 ± 0.006
Both	Superior-inferior	0.549 ± 0.163	0.684 ± 0.101

Sensitivity (percentage of eroded samples correctly classified) and specificity (percentage of thresholded samples correctly classified) of classifiers trained on VOIs from indicated dataset(s) with specified analysis direction, averaged over 50 runs of 5-fold cross-validation. Error denotes one standard deviation.

Table D.3: Classification accuracy of baseline and eroded (4-voxel radius) healthy bone samples.

Sample	Analysis direction	Sensitivity	Specificity
AE12L2	Anterior-posterior	0.968 ± 0.003	0.954 ± 0.004
AE12L2	Medial-lateral	0.927 ± 0.006	0.964 ± 0.002
AE12L2	Superior-inferior	0.858 ± 0.004	0.922 ± 0.006
F60L3	Anterior-posterior	0.890 ± 0.009	0.857 ± 0.005
F60L3	Medial-lateral	0.888 ± 0.009	0.907 ± 0.007
F60L3	Superior-inferior	0.656 ± 0.015	0.826 ± 0.015
Both	Anterior-posterior	0.920 ± 0.003	0.918 ± 0.004
Both	Medial-lateral	0.920 ± 0.003	0.946 ± 0.003
Both	Superior-inferior	0.801 ± 0.006	0.718 ± 0.004

Sensitivity (percentage of eroded samples correctly classified) and specificity (percentage of thresholded samples correctly classified) of classifiers trained on VOIs from indicated dataset(s) with specified analysis direction, averaged over 50 runs of 5-fold cross-validation. Error denotes one standard deviation.

Table D.4: Classification accuracy of osteoporotic bone samples.

Sample	Analysis direction	Mean ratio metric	Sensitivity
AE15TH10	Anterior-posterior	0.74 ± 0.08	0.923
AE15TH10	Medial-lateral	0.72 ± 0.05	0.923
AE15TH10	Superior-inferior	0.75 ± 0.06	0.542 ± 0.027
AE15TH11	Anterior-posterior	0.79 ± 0.05	0.601 ± 0.009
AE15TH11	Medial-lateral	0.72 ± 0.07	0.800
AE15TH11	Superior-inferior	0.77 ± 0.09	0.327 ± 0.020

Average sensitivity for each set of osteoporotic VOIs classified using support vector machine classifier trained on baseline thresholded and 4-voxel eroded VOIs from AE12L2 and F60L3, as well as average ratio metric of osteoporotic samples. Sensitivities are averaged over 50 runs of 5-fold cross-validation. Error denotes one standard deviation.

Bibliography

[1] P. McDonnell, P. E. McHugh, and D. O'Mahoney. Vertebral osteoporosis and trabecular bone quality. *Ann. Biomed. Eng.* **35**, 170 (2007).

[2] I. Jäger and P. Fratzl. Mineralized collagen fibrils: A mechanical model with a staggered arrangement of mineral particles. *Biophys J* **79**, 1737 (2000).

[3] C. Hellmich, F.-J. Ulm, and L. Dormieux. Can the diverse elastic properties of trabecular and cortical bone be attributed to only a few tissue-independent phase properties and their interactions. *Biomech. Model. Mechanobiol.* **2**, 219 (2004).

[4] A. Fritsch, C. Hellmich, and L. Dormieux. Ductile sliding between mineral crystals followed by rupture of collagen crosslinks: Experimentally supported micromechanical explanation of bone strength. *J. Theor. Biol.* **260**, 230 (2009).

[5] J.-Y. Reginster and N. Burlet. Osteoporosis: A still increasing prevalence. *Bone* **38**, 4 (2006).

[6] R. O. Ritchie, R. O. Buehler, and P. Hansma. Plasticity and toughness in bone. *Phys. Today* **62**, 41 (2009).

[7] E. S. Siris, P. D. Miller, E. Barrett-Connor, K. G. Faulkner, L. E. Wehren, T. A. Abbot, M. L. Berger, A. C. Santora, and L. M. Sherwood. Identification and fracture outcomes of undiagnosed low bone mineral density in postmenopausal women: Results from the national osteoporosis risk assessment. *J. Am. Med. Assoc.* **286**, 2815 (2001).

[8] B. Abrahamsen, T. van Staa, R. Ariely, M. Olson, and C. Cooper. Excess mortality following hip fracture: a systematic epidemiological review. *Osteoporos. Int.* **20**, 1633 (2009).

[9] N. C. Wright, A. C. Looker, K. G. Saag, J. R. Curtis, E. S. Delzell, S. Randall, and B. Dawson-Hughes. The recent prevalence of osteoporosis and low bone mass in the united states based on bone mineral density at the femoral neck or lumbar spine. *J. Bone Miner. Res.* **29**, 2520 (2014).

[10] Office of the Surgeon General (US). Bone health and osteoporosis: A report of the Surgeon General. Technical report. (Rockville, MD, 2004).

[11] P. Sambrook and C. Cooper. Osteoporosis. *Lancet* **367**, 2010 (2006).

[12] O. Johnell and J. A. Kanis. An estimate of the worldwide prevalence and disability associated with osteoporotic fractures. *Osteoporos. Int* **17**, 1726 (2006).

[13] M. A. Laskey. Dual-energy X-ray absorptiometry and body composition. *Nutrition* **12**, 45 (1996).

[14] J. E. Adams. Quantitative computed tomography. *Eur. J. Radiol.* **71**, 415 (2009).

[15] S. A. Goldstein, R. Goulet, and D. McCubbrey. Measurement and significance of three-dimensional architecture to the mechanical integrity of trabecular bone. *Calcif Tissue Int* **53**, S127 (1993).

[16] R. W. Goulet, S. A. Goldstein, M. J. Ciarelli, J. L. Kuhn, M. B. Brown, and L. A. Feldkamp. The relationship between the structural and orthogonal compressive properties of trabecular bone. *J. Biomech.* **27**, 375 (1994).

[17] M. L. Brandi. Microarchitecture, the key to bone quality. *Rheumatology* **48**, iv3 (2009).

[18] A. J. Fields, S. K. Eswaran, M. G. Jekir, and T. M. Keaveny. Role of trabecular microarchitecture in whole-vertebral body biomechanical behavior. *J. Bone Miner. Res.* **24**, 1523 (2009).

[19] J. S. Thomsen, E. N. Ebbesen, and L. Mosekilde. Age-related differences between thinning of horizontal and vertical trabeculae in human lumbar bone as assessed by a new computerized method. *Bone* **31**, 136 (2002).

[20] R. Huiskes, R. Ruimerman, G. H. van Lenthe, and J. D. Janssen. Effects of mechanical forces on maintenance and adaptation of form in trabecular bone. *Nature* **405**, 704 (2000).

[21] R. Ruimerman, P. Hilbers, B. van Rietbergen, and R. Huiskes. A theoretical framework for strain-related trabecular bone maintenance and adaptation. *J. Biomech.* **38**, 931 (2005).

[22] J. Wolff, P. G. J. Maquet (translator), and R. Furlong (translator). *The Law of Bone Remodelling* (Springer-Verlag, Berlin, New York, 1986).

[23] J. E. Bertram and S. M. Swartz. The 'law of bone transformation': a case of crying Wolff? *Biol. Rev. Camb. Philos. Soc.* **66**, 245 (1991).

[24] M. E. J. Newman. *Networks: An Introduction* (Oxford University Press, 2010).

[25] D. Hu and D. Cai. Adaptation and optimization of biological transport networks. *Phys. Rev. Lett.* **111**, 138701 (2013).

[26] H.-J. Park and K. Friston. Structural and functional brain networks: From connections to cognition. *Science* **342**, 1238411 (2013).

[27] N. Pinter-Wollman, E. A. Hobson, J. E. Smith, A. J. Edelman, D. Shizuka, S. de Silva, J. S. Waters, S. D. Prager, T. Sasaki, G. Wittemyer, J. Fewell, and D. B. McDonald. The dynamics of animal social networks: analytical, conceptual, and theoretical advances. *Behav. Ecol.* **25**, 242 (2013).

[28] L. Papadopoulos, M. A. Porter, K. E. Daniels, and D. S. Bassett. Network analysis of particles and grains. *J. Complex Netw.* **6**, 485 (2017).

[29] F. J. Pérez-Reche, S. N. Taraskin, W. Otten, M. P. Viana, L. da F. Costa, and C. A. Gilligan. Prominent effect of soil network heterogeneity on microbial invasion. *Phys. Rev. Lett.* **109**, 98102 (2012).

[30] S. M. Tommasini, S. Wearne, P. R. Hof, and K. J. Jepsen. Percolation theory relates corticocancellous architecture to mechanical function in vertebrae of inbred mouse strains. *Bone* **42**, 743 (2008).

[31] S. Boutroy, M. L. Bouxsein, F. Munoz, and P. D. Delmas. *In vivo* assessment of trabecular bone michroarchitecture by high-resolution peripheral quantitative computed tomography. *J. Clin. Endocrinol. Metab.* **90**, 6508 (2005).

[32] D. S. Bassett, M. A. Porter, N. F. Wymbs, S. T. Grafton, J. M. Carlson, and P. J. Mucha. Robust detection of dynamic community structure in networks. *Chaos* **23**, 13142 (2013).

[33] M. Girvan and M. E. J. Newman. Community structure in social and biological networks. *Proc. Natl. Acad. Sci. U.S.A.* **99**, 7821 (2002).

[34] K. K. Nishiyama and E. Shane. Clinical imaging of bone microarchitecture with HR-pQCT. *Curr. Osteoporos. Rep.* **11**, 147 (2013).

[35] F. W. Wehrli, B. R. Gomberg, P. K. Saha, H. K. Song, S. N. Hwang, and P. J. Snyder. Digital topological analysis of in vivo magnetic resonance microimages of trabecular bone reveals structural implications of osteoporosis. *J. Bone Miner. Res.* **16**, 1520 (2001).

[36] R. G. Pautler and S. E. Fraser. The year(s) of the contrast agent – micro-MRI in the new millennium. *Curr. Opin. Immunol.* **15**, 385 (2003).

[37] D. W. Dempster, J. E. Compston, M. K. Drezner, F. H. Glorieux, J. A. Kanis, H. Malluche, P. J. Meunier, S. M. Ott, R. R. Recker, and A. M. Parfitt. Standardized nomenclature, symbols, and units for bone histomorphometry: A 2012 update of the report of the asbmr histomorphometry nomenclature committee. *J. Bone Miner. Res.* **28**, 2 (2013).

[38] C. A. M. Kulak and D. W. Dempster. Bone histomorphometry: a concise review for endocrinologists and clinicians. *Arq. Bras. Endocrinol. Metab.* **54**, 87 (2010).

[39] M. L. Bouxsein, S. K. Boyd, B. A. Christiansen, R. E. Guldberg, K. J. Jepsen, and R. Muller. Guidelines for assessment of bone microstructure of rodents using micro-computed tomography. *J. Bone Miner. Res.* **25**, 1468 (2010).

[40] G. Dong, Q. Dong, Y. Liu, B. Lou, J. Feng, K. Wang, X. Zhou, and H. Wu. High-resolution micro-CT scanning as an innovative tool for evaluating dental hard tissue development. *J. Appl. Clin. Med. Phys.* **15**, 335 (2014).

[41] G. Beller, M. Burkhart, D. Felsenberg, W. Gowin, H. Hege, B. Koller, S. Prohaska, P. Saparin, and J. Thomsen. Vertebral body data set ESA29-99-L3, 2005.

[42] CT-analyser, Bruker microCT (Kontich, Belgium), http://bruker-microct.com/products/ctan.htm.

[43] N. Otsu. A threshold selection method from gray-level histograms. *IEEE Trans. Syst. Man. Cybern.* **9**, 62 (1979).

[44] T. C. Lee and R. L. Kashyap. Building skeleton models via 3-D medial surface/axis thinning algorithms. *Comput. Vis. Graph. Image Process.* **56** (1994).

[45] M. Kerschnitzki, P. Kollmannsberger, M. Burghammer, G. N. Duda, R. Weinkamer, W. Wagermaier, and P. Fratzl. Architecture of osteocyte network correlates with bone material quality. *J. Bone Miner. Res.* **28**, 1837 (2013).

[46] M. Doube, M. M. Klosowski, I. Arganda-Carreras, F. P. Cordelières, R. P. Dougherty, J. S. Jackson, B. Schmid, and J. R. Hutchinson. BoneJ: Free and extensible bone image analysis in ImageJ. *Bone* **47**, 1076 (2010).

[47] J. Y. Rho, R. B. Ashman, and C. H. Turner. Young's modulus of trabecular and cortical bone material: ultrasonic and microtensile measurements. *J. Biomech.* **26**, 111 (1993).

[48] C. Jorgenson and T. Kundu. Measurement of material elastic constants of trabecular bone: a micromechanical analytic study using a 1 GHz acoustic microscope. *J. Orthop. Res.* **20**, 151 (2002).

[49] L. Pothuaud, B. V. Rietbergen, C. Charlot, E. Ozhinsky, and S. Majumdar. A new computational efficient approach for trabecular bone analysis using beam models generated with skeletonized graph technique. *Comput. Methods Biomech. Biomed. Eng.* **7**, 205 (2004).

[50] J. Homminga, B. R. Mccreadie, H. Weinans, and R. Huiskes. The dependence of the elastic properties or osteoporotic cancellous bone on volume fraction and fabric. *J. Biomech.* **36**, 1461 (2003).

[51] A. Nazarian, D. von Stechow, D. Zurakowski, R. Müller, and B. D. Snyder. Bone volume fraction explains the variation in strength and stiffness of cancellous bone affected by metastatic cancer and osteoporosis. *Calcif. Tissue Int.* **83**, 368 (2008).

[52] L. J. Gibson, M. F. Ashby, and B. A. Harley. *Cellular Materials in Nature and Medicine* (Cambridge University Press, 2010).

[53] C. J. Hernandez, G. S. Beaupré, T. S. Keller, and D. R. Carter. The influence of bone volume fraction and ash fraction on bone strength and modulus. *Bone* **29**, 74 (2001).

[54] M. M. Driscoll, B. G.-g. Chen, T. H. Beuman, S. Ulrich, S. R. Nagel, and V. Vitelli. The role of rigidity in controlling material failure. *Proc. Natl. Acad. Sci. U.S.A.* **113**, 10813 (2016).

[55] C. Nguyen, K. J. Schlesinger, T. W. James, K. M. James, R. L. Sah, K. Masuda, and J. M. Carlson. Novel magnetic resonance technique for characterizing mesoscale structure of trabecular bone. *R. Soc. Open Sci.* **5**, 180563 (2018).

[56] M. R. Allen, E. McNerny, J. M. Organ, and J. M. Wallace. True gold or pyrite: A review of reference point indentation for assessing bone mechanical properties in vivo. *J. Bone Miner. Res.* **30**, 1539 (2015).

[57] M. P. Bendsøe and O. Sigmund. *Topology Optimization* (Springer, 2003).

[58] D. Peetz. Multi-objective topology optimization for trabecular bone-like structure: Role of stability and surface area. Master's thesis, University of Illinois at Urbana-Champaign, 2016.

[59] E. Seeman and P. D. Delmas. Bone quality – the material and structural basis of bone strength and fragility. *N. Engl. J. Med.* **354**, 2250 (2006).

[60] C. Boyle and I. Y. Kim. Three-dimensional micro-level computational study of Wolff's law via trabecular bone remodeling in the human proximal femur using design space topology optimization. *J. Biomech.* **44**, 935 (2011).

[61] I. G. Jang and I. Y. Kim. Computational study of Wolff's law with trabecular architecture in the human proximal femur using topology optimization. *J. Biomech.* **41**, 2353 (2008).

[62] S. Fortunato and D. Hric. Community detection in networks: A user guide. *Phys. Rep.* **659**, 1 (2016).

[63] D. S. Bassett, E. T. Owens, M. A. Porter, M. L. Manning, and K. E. Daniels. Extraction of force-chain network architecture in granular materials using community detection. *Soft Matter* **11**, 2731 (2015).

[64] L. Papadopoulos, J. G. Puckett, K. E. Daniels, and D. S. Bassett. Evolution of network architecture in a granular material under compression. *Phys. Rev. E* **94**, 32908 (2016).

[65] E. Berthier, M. A. Porter, and K. E. Daniels. Forecasting failure locations in two-dimensional disordered lattices. arXiv:1812.08025 (2019).

[66] J. Y. Rho, L. Kuhn-Spearing, and P. Zioupos. Mechanical properties and the hierarchical structure of bone. *Med. Eng. Phys.* **20**, 92 (1998).

[67] P. Fratzl and R. Weinkamer. Nature's hierarchical materials. *Prog. Mater. Sci.* **52**, 1263 (2007).

[68] E. Donnelly. Methods for assessing bone quality: A review. *Clin. Orthop. Relat. Res.* **469**, 2128 (2011).

[69] P. K. Hansma, P. J. Turner, and G. E. Fantner. Bone diagnostic instrument. *Rev. Sci. Instrum.* **77**, 75105 (2006).

[70] P. Hansma *et al.* The bone diagnostic instrument II: Indentation distance increase. *Rev. Sci. Instrum.* **79**, 64303 (2008).

[71] M. A. Gallant, D. M. Brown, J. M. Organ, M. R. Allen, and D. B. Burr. Reference-point indentation correlates with bone toughness assessed using whole-bone traditional mechanical testing. *Bone* **53**, 301 (2013).

[72] M. G. Ghany, D. E. Kleiner, H. Alter, E. Doo, F. Khokar, K. Promrat, D. Herion, Y. Park, T. J. Liang, and J. H. Hoofnagle. Progression of fibrosis in chronic hepatitis C. *Gastroenterol.* **124**, 97 (2003).

[73] A. G. Nicholson, L. G. Fulford, T. V. Colby, R. M. du Bois, D. M. Hansell, and A. U. Wells. The relationship between individual histologic features and disease progression in idiopathic pulmonary fibrosis. *Am. J. Respir. Crit. Care Med.* **166**, 173 (2002).

[74] L. A. Adams, S. Sanderson, K. D. Lindor, and P. Angulo. The histological course of nonalcoholic fatty liver disease: a longitudinal study of 103 patients with sequential liver biopsies. *J. Hepatol.* **42**, 132 (2005).

[75] B. Busse, M. Hahn, M. Soltau, J. Zustin, K. Püschel, G. N. Duda, and M. Amling. Increased calcium content and inhomogeneity of mineralization render bone toughness in osteoporosis: Mineralization, morphology and biomechanics of human single trabeculae. *Bone* **45**, 1034 (2009).

[76] T. M. Keaveny and O. C. Yeh. Architecture and trabecular bone â toward an improved understanding of the biomechanical effects of age, sex and osteoporosis. *J. Musculoskel. Neuron Interact.* **2**, 205 (2002).

[77] A. Odgaard, J. Kabel, B. van Rietbergen, M. Dalstra, and R. Huiskes. Fabric and elastic principal directions of cancellous bone are closely related. *J. Biomech.* **30**, 487 (1997).

[78] D. Chase, T. James, and K. James. Selective sampling magnetic resonance-based method for assessing structural spatial frequencies, 2016. US Patent 9366738 B2.

[79] R. Bitar, G. Leung, R. Perng, S. Tadros, A. R. Moody, J. Sarrazin, C. McGregor, M. Christakis, S. Symons, A. Nelson, and T. P. Roberts. MR pulse sequences: What every radiologist wants to know but is afraid to ask. *Radiographics* **26**, 513 (2006).

[80] M. Zaitsev, J. Maclaren, and M. Herbst. Motion artifacts in MRI: A complex problem with many partial solutions. *J. Magn Reson Imaging* **42**, 887 (2015).

[81] J. S. Thomsen, M. V. Jensen, A. S. Niklassen, E. N. Ebbesen, and A. Brüel. Age-related changes in vertebral and iliac crest 3D bone microstructure differences and similarities. *Osteoporos. Int.* **26**, 219 (2015).

[82] T. D. Faber, D. C. Yoon, and S. C. White. Fourier analysis reveals increased trabecular spacing in sickle cell anemia. *J. Dent. Res.* **81**, 214 (2002).

[83] T. D. Faber, D. C. Yoon, S. K. Service, and S. C. White. Fourier and wavelet analyses of dental radiographs detect trabecular changes in osteoporosis. *Bone* **35**, 403 (2004).

[84] G. E. Fantner, T. Hassenkam, J. H. Kindt, J. C. Weaver, H. Birkedal, L. Pechenik, J. A. Cutroni, G. A. Cidade, G. D. Stucky, D. E. Morse, and P. K. Hansma. Sacrificial bonds and hidden length dissipate energy as mineralized fibrils separate during bone fracture. *Nat. Mater.* **4**, 612 (2005).

[85] J. Currey. Sacrificial bonds heal bone. *Nature* **414**, 699 (2001).

[86] H. D. Espinosa, J. E. Rim, F. Barthelat, and M. J. Buehler. Merger of structure and material in nacre and bone – perspectives on de novo biomimetic materials. *Prog. Mater. Sci.* **54**, 1059 (2009).

[87] Z. Yin, F. Hannard, and F. Barthelat. Impact-resistant nacre-like transparent materials. *Science* **364**, 1260 (2019).

[88] L. G. S. Jeub, M. Bazzi, I. S. Jutla, and P. J. Mucha. A generalized Louvain method for community detection implemented in MATLAB, `https://github.com/GenLouvain/GenLouvain`, 2011-2019.

[89] M. E. J. Newman and M. Girvan. Finding and evaluating community structure in networks. *Phys. Rev. E* **69**, 26113 (2004).

[90] T. Hildebrand and P. Rüegsegger. A new method for the model-independent assessment of thickness in three-dimensional images. *J. Microsc.* **185**, 67 (1997).

[91] J. Homminga, B. Van-Rietbergen, E. Lochmüller, H. Weinans, F. Eckstein, and R. Huiskes. The osteoporotic vertebral structure is well adapted to the loads of daily life, but not to infrequent "error" loads. *Bone* **34**, 510 (2004).